12-2021

# Stimuli-Responsive and Electrically Conductive Metal-Organic Frameworks

Amina Khatun
akhatun@g.clemson.edu

# STIMULI-RESPONSIVE AND ELECTRICALLY CONDUCTIVE METAL-ORGANIC FRAMEWORKS

---

A Dissertation
Presented to
the Graduate School of
Clemson University

---

In Partial Fulfillment
of the Requirements for the Degree
Doctor of Philosophy
Chemistry

---

by
Amina Khatun
December 2021

---

Accepted by:
Dr. Sourav Saha, Committee Chair
Dr. Julia L. Brumaghim
Dr. Stephen E. Creager
Dr. William T. Pennington

## ABSTRACT

Metal-organic frameworks (MOFs), a class of porous materials made of organic ligands linked by metal ions or cluster nodes, are well known for their highly ordered crystalline structure and chemical and structural tunability. Due to their porous nature, MOFs can encapsulate guest molecules inside the cavities. The tunable structures, compositions, porosity, and surface area make MOFs useful for various applications, such as gas storage and separation, chemical sensing, catalysis, optoelectronics, and drug delivery.

In chapter 2, I present a new luminescent metal-organic framework (LMOF) featuring energy transfer and stimuli ($Hg^{2+}$) responsive capabilities. The two fluorophoric ligands incorporated in the LMOF framework have complementary absorption and emission, which allows ligand-to-ligand energy transfer. Therefore, upon excitation, the donor transfers the excitation energy to the acceptor chromophore via Förster resonance energy transfer (FRET), and as a result, the MOF emission stemmed from the lower energy emitter (acceptor chromophore). In addition to this, our MOF displayed significant red-shift and quenching of its photoluminescence in the presence of $Hg^{2+}$ solution while only a modest fluorescence quenching but no spectral shifts in the presence of other transition metal ions. Moreover, the framework structure remained intact after exposure to $Hg^{2+}$ and other transition metal ions, and its original photoluminescence spectrum could be restored by simple washing, making it a promising reusable $Hg^{2+}$ sensor. These studies demonstrate the light-harvesting and toxic $Hg^{2+}$ sensing capabilities of a new luminescent MOF.

Chapter 3 focuses on the tuning of the optical and electrical bandgap of a MOF-74 analog. The MOF-74 was constructed from an electron-deficient naphthalene diimide-

based ligand containing two salicylic acid groups to coordinate with $Zn^{2+}$ metal ion. To tune the bandgap of this MOF-74, an electron-rich guest (tetrathiafulvalene; TTF) guests are encapsulated along the wall of the framework. This arrangement of the TTF in the framework increases the electron delocalization via π-π stacking, resulting in the reduction of the bandgap of the MOF by approximately 1 eV.

Studies presented in chapter 4 investigate the improvement of the electrical conductivity of an insulating MOF by introducing conductive polymers inside the MOF cavities. In this study, the MOF was loaded with the monomers (EDOT and Py) of the respective conductive polymers (PEDOT and PPy), and polymerization was carried out in the presence of an oxidant (iodine). The resulting MOF-polymer composites exhibit a significantly higher conductivity in comparison to the pristine insulating MOF.

# DEDICATION

I dedicate this dissertation to my dearest parents.

ACKNOWLEDGEMENT

I would like to express my sincere thanks to my supervisor Dr. Sourav Saha for his continuous support and guidance in helping me achieve my Ph.D.

I would also like to express my deepest gratitude to Dr. Ashok Yadav, Dr. Dillip K. Panda, and Dr. Krishnendu Maity for their intellectual input and help in my research. I am forever indebted to them for encouraging me not to lose hope throughout the past years of my graduate study. I like to extend my special thanks to Dr. Ashok Yadav again for providing me with his valuable feedback on my dissertation.

I would like to thank Dr. Julia Brumaghim, Dr. Stephen Creager, and Dr. William Pennington for serving as my Ph.D. committee members and for their valuable suggestions and feedback. I am extremely thankful to Dr. Colin McMillen for his contribution and help in solving crystal structures. Thanks to our collaborators Dr. Michael Walter, Dr. Nickolas Sayresmith, Dr. Wei Zhou, for their help.

I am also thankful to my present lab mates Shiyu Zhang, Monica, Paola, Weikang, and my former labmate Andrei Palukoshka.

I am extremely thankful to my friends Sagar Dasgupta, Dr. Khadijatul Kobra, Nushrat Humaira, Dr. Waziha Farha, and Dr. Niamat-e-Khuda Lamia for being there always for me in my good and bad times during my graduate study. I cannot even begin to thank my sisters Taslima Tumpa and Fahima Afroze Chhoya, my aunty Razia Islam, and my other family members Didar Sheikh, Suma, Neelima, Niloy, and Elephant Road's uncles and aunties for their unconditional love and support. It would have been very difficult to accomplish this Degree without their continuous support and encouragement.

TABLE OF CONTENTS

Page

Table of Contents (Continued)

## LIST OF TABLES



## LIST OF FIGURES

## LIST OF ABBREVIATIONS

| | |
|---|---|
| BDC | Benzenedicarboxylic acid |
| BET | Brunauer–Emmett–Teller |
| BPDC | Biphenyldicarboxylic acid |
| BPY | Bipyridyl |
| BTC | Benzenetricarboxylic acid |
| BTP | 4,4′,4″-(benzene-1,3,5-triyl)tris(pyrazol-1-ide) |
| CT | Charge transfer |
| DEF | Diethyl formamide |
| DET | Dexter energy transfer |
| DMF | Dimethyl formamide |
| DMSO | Dimethyl sulfoxide |
| DMNB | 2,3-dimethyl-2,3-dinitrobenzene |
| DNT | 2,4-dinitrotoluene |
| DPTTZ | Dipyridyl thiazolothiazole |
| DRS | Diffuse reflectance spectroscopy |
| DSC | Differential scanning calorimetry |
| EDOT | 3,4-ethylenedixoythiphene |
| EDX | Energy dispersive x-ray |
| ET | Energy transfer |
| EtOH | Ethanol |

| | |
|---|---|
| FRET | Förster resonance energy transfer |
| FTIR | Fourier-transform Infrared |
| HKUST | Hong Kong University of Science and Technology |
| HTTP | 2,3,6,7,10,11-hexaminotriphenylene |
| I-V | Current-Voltage |
| LLCT | Ligand-to-ligand charge transfer |
| LMCT | Ligand-to-metal charge transfer |
| LMOF | Luminescent metal–organic framework |
| MeCN | Acetonitrile |
| MeOH | Methanol |
| MIL | Materials of Institut Lavoisier |
| MLCT | Metal-to-ligand charge transfer |
| MMCT | Metal-to-metal charge transfer |
| MOF | Metal–organic framework |
| MTV | Multivariate |
| NDC | Naphthalene dicarboxylic acid |
| NDA | 1,4,5,8-Naphthalenetetracarboxylic dianhydride |
| NDI | Naphtalenediimide |
| NIR | Near Infrared |
| NMR | Nuclear magnetic resonance |
| NTB | 4,4′,4″-nitrilotrisbenzoic acid |

| | |
|---|---|
| Pdt | 2,3-pyrazinedithiolate |
| PEDOT | poly3,4-ethylenedioxythiophene |
| PL | Photoluminescence |
| PXRD | Powder x-ray diffraction |
| Py | Pyrrole |
| PPy | Polypyrrole |
| SBU | Secondary building unit |
| STEM | Scanning transmission electron microscopy |
| SXRD | Single crystal x-ray diffraction |
| TCNQ | 7,7,8,8-tetracyanoquinododimethane |
| TCPP | Tetrakis(4-carboxyphenyl)porphyrin |
| TCSPC | Time-corelated single photon counting |
| TEOA | Triethanolamine |
| TGA | Thermogravimetric analysis |
| TNP | 2,3,5-trinitrotoluene |
| TPT | 2,4,6-tri(4-pyridyl)-1,3,5-triazine |
| TTF | Tetrathiafulvalene |
| TTFTB | Tetrathiafulvalene tetrabenzoate |
| UiO | Universitetet i Oslo |
| UV | Ultraviolet |
| Vis | Visible |

# CHAPTER ONE

# INTRODUCTION

## 1.1. Metal-organic frameworks (MOFs)

Metal-organic frameworks (MOFs)[1,2]- are an emerging class of hybrid porous materials that blends the discrete properties of organic and inorganic materials, e.g., redox-tunability of organic ligands and the structural order of crystalline inorganic semiconductors. MOFs have been studied widely for their many different applications over the past decades. MOFs[1-6] are constructed via the coordination of polydentate organic ligands/linkers with metal ions that lead to the formation of one, two, and three-dimensional frameworks. The metal ion clusters that are connected by the organic ligands are called secondary building units (SBUs),[1] which, along with the ligand geometry, define the topology of the frameworks.

The seemingly unlimited choice of organic linkers along with a wide variety of metal ions makes it possible to construct an infinite number of MOFs. In addition, the incorporation of different types of linkers into the same frameworks results in multivariate MOFs, which include different functionalities in the framework.[1] This opportunity offers a high degree of tunability in the MOFs structure, such as porosity, surface area, chemical, and thermal stability, and properties. The organic ligands in the MOFs framework also allow for tuning of the pore's chemical nature by post-synthetic[7,8] incorporation of desired functional groups, which further modify the chemical property and the size and shape of the pores. These flexibilities to tune the MOF structure make them unique from traditional

porous materials such as zeolite and porous carbon.[1] Due to such uniqueness MOFs are considered potential candidates for a wide variety of applications, including- gas storage and separation,[6] chemical sensing,[9-14] catalysis,[15,16] optoelectronics,[17,18] bio-imaging,[19,20] and drug delivery.[20]

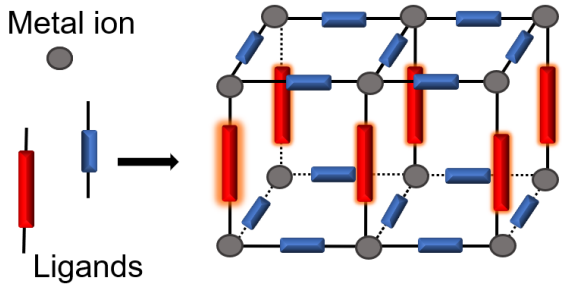


**Figure 1.1:** Illustration of a metal-organic framework (MOF).

## 1.2. Framework building units

### 1.2.1. Organic linkers

Organic ligands with functional groups such as carboxylic, pyridyl, hydroxy, etc., that can coordinate with the metal ions are widely used as linkers in the MOFs construction. Some of the examples are given in **Figure 1.2**.

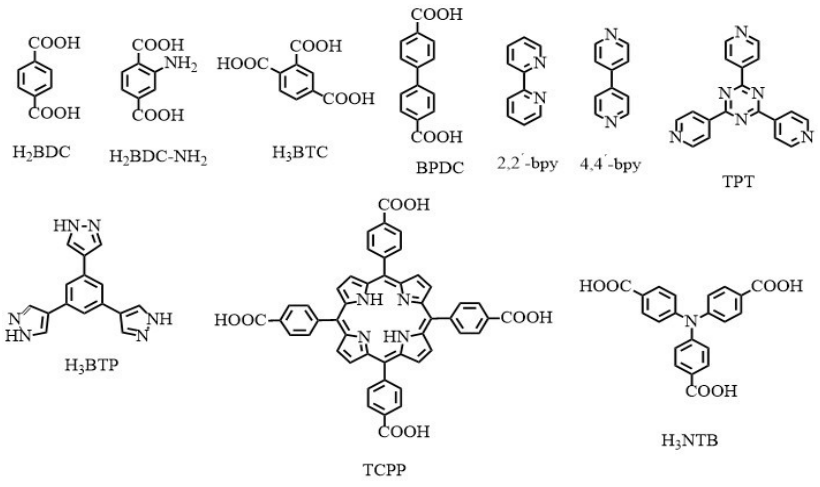


**Figure 1.2:** Selected examples of organic linkers.[1,4,6,14]

### 1.2.2. Secondary building units (SBUs)

Secondary building units (SBUs)[21,22] are integral MOFs that dictate the framework topology and robustness. Based on this principle, the MOF structure should be predictable, and the targeted topology with permanent porosity and the high surface area should be achievable by using the appropriate SBUs and organic linkers.

In contrast to traditional coordination polymers, where a single metal node connects the linkers, the vast majority of MOFs are composed of polyatomic metal clusters in the framework, which typically make them structurally more robust.[23] For example, in the case of MOF-5 that contains $Zn_4O(CO_2)_6$ inorganic SBU comprise twelve Zn-O bonds, whereas, in a typical tetrahedral coordination polymer, this number is only four (4 M-L bonds in $Zn(L)_2(ClO_4)_2$; L= N, N′-Bis(4-pyridyl)urea).[23] The stability of the polynuclear cluster of SBUs afford the structural robustness to the resulting MOFs[22,24]

## 1.3.Synthetic Approaches

In general, MOFs are synthesized by combining organic ligands and metal ions. Although the structure of the MOFs depends on the framework building units (metal clusters and linkers), several other factors such as temperature, pH, pressure, solvent, and reaction time play a significant role in the MOF synthesis.[25] Over the years, several approaches (discussed below) have been developed to synthesize targeted MOF structures.

### 1.3.1. Conventional synthesis (solvothermal)

The most widely used synthetic approach for MOFs is solvothermal synthesis. Under solvothermal conditions, the organic ligands and metal salts are mixed together in a vial or Teflon-lined autoclave and electrically heated at temperatures ranging from 80-260 °C for several hours to days to obtain MOFs. Generally, alkyl formamides, alcohols, pyridine, and water (hydrothermal) are used in this synthetic approach.[25,26] In some cases, a small amount of base, e.g., amines or acids such as nitric acid, is used in the MOF synthesis to facilitate or slow down the reaction, where appropriate.[26] However, the solvents alkylformamides (DMF, DEF) produce amines upon decomposition at a higher temperature, favor the deprotonation of organic ligands, and eliminate the necessity of using an additional base. An enormous number of MOFs have been synthesized using this conventional synthetic approach due to the ease of this technique and affordability to generate crystalline materials in most cases.[27-30]

### 1.3.2. Microwave-assisted synthesis

This synthetic technique utilizes microwaves and mobile electric charges (e.g., polar solvent molecules or ions) interactions to synthesize MOFs.[25,26,31] Microwave syntheses are considered analogous to conventional solvothermal synthesis. This technique is adapted to efficiently control the particle size and generate nano-sized MOF crystals at a significantly shorter period of time. [32-34]

### 1.3.3. Electrochemical synthesis

The BASF[36] researchers first reported the electrochemical synthesis of MOF. Using this technique, primarily Cu-based, Zn-based, and Al-based MOFs have been synthesized on an industrial scale.[25] In electrochemical synthesis, metal plates (Zn, Cu, etc.) are employed as an anode or cathode, and the organic ligands are dissolved in the solvent. This technique typically yields highly pure MOFs quickly due to the absence of counter anions such as chloride, nitrate, etc., since metal ions are used instead of metal salts in the MOF formation.[31] Several examples of electrochemically synthesized MOFs have been reported in the literature.[37-39]

### 1.3.4. Diffusion method

To obtain a larger and higher-quality crystal and avoid the formation of polycrystalline MOF, diffusion methods are used. In a solvent-liquid diffusion, three layers of solvent with different densities are used- i) precipitant solvent layer, ii) product solvent layer, iii) solvent that separates i, and ii. Slow diffusion of the precipitant solvent layer into the other layers results in crystal growth at the interface that usually takes a very long time (weeks).[31,35]

## 1.4. Luminescent metal-organic frameworks (LMOFs)

Luminescent metal-organic frameworks (LMOFs) are a growing sub-class of MOFs. LMOFs have attracted interest from scientists due to their ability to act as chemical sensors and potential light-harvesting materials.[14,40-48] As sensors, LMOFs offer easy detection through emission changes such as turn-on/turn-off emission, wavelength shift, intensity

change, new emission, etc. In addition, the structural diversity of LMOFs that can be attained by utilizing various organic ligands and metal ions, post-synthetic modifications made them advantageous over traditional luminescent materials.[13,14]

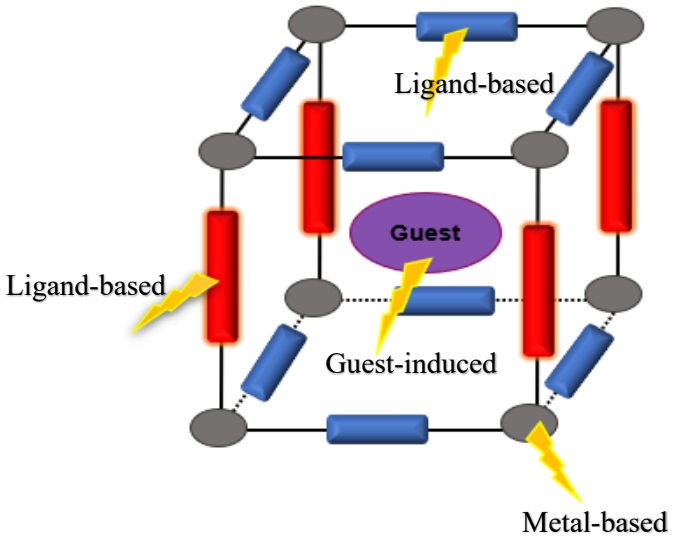


**Figure 1.4:** A schematic representation of the possible origin of luminescence in LMOF.

Luminescence in MOFs can originate from a variety of mechanisms (**Figure 1.4**) due to having diverse building blocks (organic linkers and metal ions) and having the ability to encapsulate guests in the porous frameworks. Therefore, the emission from LMOFs can be ligand-based, metal-centered, and can also arise from host-guest interactions of the immobilized guest molecules inside the pore in the framework.[13] Emission in LMOFs can occur via the spin allowed transition from singlet excited state ($S_1$) to singlet ground state ($S_0$) (fluorescence), or via non-radiative intersystem crossing

from singlet excited state ($S_1$) to triplet state ($T_1$) followed by spin forbidden transition from triplet ($T_1$) to singlet ground state ($S_0$) (Phosphorescence).[14]

### 1.4.1. Organic ligand-based emissions

Organic ligands with π electron-rich backbones are the main contributor of luminescence in most LMOFs. The emissions from these linkers mostly happen due to the $\pi \rightarrow \pi^*$ or $n \rightarrow \pi^*$ transition from the lowest-lying excited singlet state to the singlet ground state.[13] The framework fluorescence (intensity, lifetime, quantum yield) stemming from the linkers can be different from the free ligands in the solution. This difference arises from the immobilization of organic linkers in the MOFs that reduces the non-radiative decay of these linkers from the excited state and enhances the quantum yield due to the reduction of π-π interactions.[13] The linker-based emission could stem either purely from the ligand or as a result of ligand-to-ligand charge transfer (LLCT), ligand-to-metal charge transfer (LMCT), metal-to-ligand charge transfer (MLCT).[13,14] These energy transfer processes are discussed in section **1.4.4**.

### 1.4.2. Metal centered luminescence

The electronic configuration of metal ions has a significant influence on the luminescence of MOFs.[13] LMOFs that are constructed with transition metal ions mostly exhibit linker-based emission. The most commonly known transition metal-based LMOFs contains $d^{10}$ metal ions Zn(II) and Cd(II) in their frameworks.[13] A fully filled d-orbital ($d^{10}$) rules out effective quenching that can occur from paramagnetic transition metals ions.[14] LMOFs

containing lanthanide metal ions exhibit metal-centered emission. Although lanthanide emission is very weak due to forbidden f-f transitions (Laporte selection rule), the close proximity of lanthanide metal ions to the highly absorbing organic ligands in the LMOFs allows sensitization of metal ions via antenna effect and hence enhances the emission intensity of lanthanides in LMOFs.[13,14] Sensitization of lanthanide metal ions involves three steps- i) absorption of light by the organic linkers, ii) energy transfer to the lanthanide ions from the excited state linkers, and iii) emission from lanthanide ions.[13,14]

### 1.4.3. Guest-induced luminescence

Owing to their porous nature, MOFs can accommodate a variety of lumophores such as luminescent dye, lanthanide metal ions in the pores, which adds another dimension to tune the existing luminescent or fabricating the luminescent for a non-emissive MOF.[13, 14]

The guests can interact with the host MOF in several different ways,[49] such as Van der Waals interactions, π-π interactions, or H-bonding interactions, which may lead to the change of excitation energy state of the host MOF. The host-guest interactions may also lead to changes in emission intensity or emission wavelengths that can be utilized in various applications such as sensing and separations.[49]

### 1.4.4. Energy transfer interactions

The design of MOFs with energy/charge transfer interactions has been of great interest in the scientific community due to various possible applications ranging from sensing, photocatalysis, and optoelectronics.[18,43,50-53] MOFs offer a solid platform for designing the

directional energy transfer (ET) pathway required for a particular application of interest due to- i) it allows high chromophore ordering in the framework, which reduces the exciton quenching, ii) high degree of photon capture and energy migration to the reaction center, iii) structural detail and the nature of chromophore arrangement in the highly crystalline MOFs can be easily deciphered by SXRD; which further act as a vital tool model ET pathways.[45] There are several possible routes[13,14,45] for ET in the MOFs such as ligand-to-ligand charge transfer (LLCT), ligand-to-metal charge transfer (LMCT), metal-to-metal charge transfer MMCT, MLCT, and host-guest CT (**Figure 1.5**).

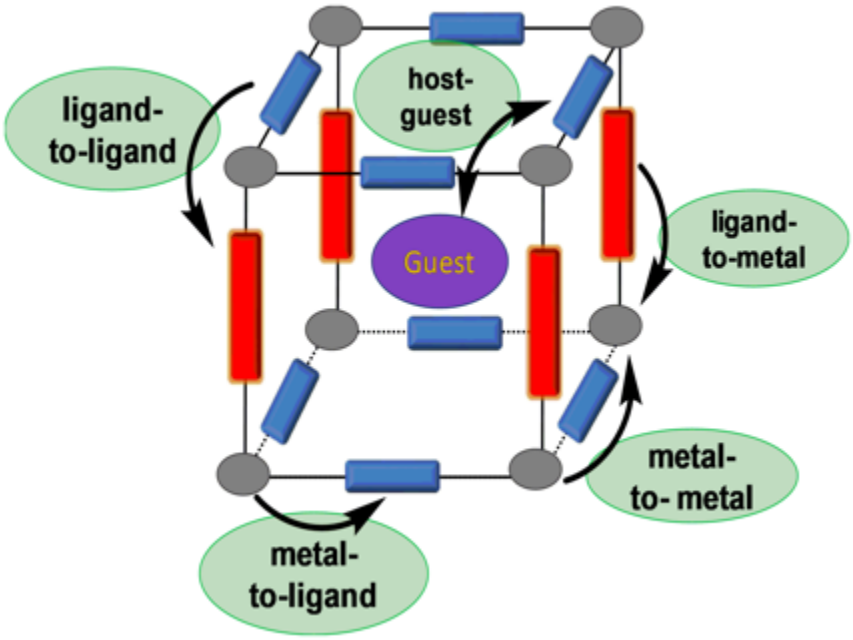


**Figure 1.5**: A schematic representation of possible energy transfer in LMOF

The ET processes in MOFs that occur between two different chromophores can further be described by two different mechanisms- Förster resonance energy transfer (FRET) and

Dexter energy transfer (DET). Förster resonance energy transfer (FRET) requires overlap of emission of the donor (D) and absorption of acceptor (A) chromophore, hence can occur in long-range (1-10nm).[12,14] In FRET, the energy transfer between chromophores happens due to the Coulombic interactions in a non-radiative fashion. On the other hand, Dexter energy transfer (DET) occurs in the short distance that requires orbital overlap of donor and acceptor chromophore for electron exchange and coupling.[12,14,45]

### 1.5.Electrically Conductive MOFs

Designing electrically conductive MOFs has been a prospective area of research in the MOF field in recent years due to their potential for electrocatalysis, chemiresisitive sensing, and energy storage applications.[54,55] Introducing redox-active linkers, metal ions in the framework, or redox-active/conductive guest encapsulation in the pores leading to intrinsically conducting and guest promoted conducting MOF, respectively. However, combining the porosity of MOFs and the electrically conductive nature is very challenging because the inherent porosity limits the charge transport pathways (through space).[54,56] To date, most MOFs are made with non-redox active linkers and metal ions; therefore, the number of electrically conductive MOFs are not as significant as some other fields such as gas storage and separation, sensing, etc.[54,56,57]

Of the huge number of MOFs, the majority are made by linking carboxylate linkers to the metal ions, which results in relatively ionic bonds in the SBUs causes large energy gaps and trapped valences.[55,56] Therefore, even when this type of SBUs connects active redox linkers, it hinders through bond charge transport, and as a consequence, the material

provides poor conductivity. However, judicious choice of linkers and metal ions, control over the interaction of SBU formation, and exploiting the porosity by incorporating redox-active guests can facilitate charge transport in the framework and lead to the material with considerable electrical conductivity.

### 1.5.1. Transport mechanisms

The charge transport in MOFs follow two general mechanisms-

i) hopping: charge transfer occurs between nonbonded and localized charge carriers[54]

ii) band transport: charge carriers are delocalized. Due to the strong intramolecular interactions between the sites, the delocalized charge carriers form a continuous energy band.[54]

### 1.5.2. Strategies towards conductive MOFs

For both intrinsic and guest-promoted conductive MOFs, two common approaches have been followed- through-bond and through-space.

### 1.5.3. Through-bond

The through-bond approach focuses on constructing MOFs with a favorable spatial and energetic overlap of the coordinated metal ions and ligand for promoting charge delocalization.[54,55,58-63] In this regard, sulfur and nitrogen-containing softer and more electropositive ligands where the coordination happens through sulfur and nitrogen have

been used.[58,64] The better metal-ligand orbital overlap leads to small bandgap energy and facilitates high charge mobility, resulting in high conductivity. Kitagawa and coworkers[65] reported first conductive MOF $Cu[Cu(pdt)_2]$ (pdt=2,3-pyrazinedithiolate) that exhibited $6x10^{-4}$ $Scm^{-1}$ conductivity (through-bond). In $Cu[Cu(pdt)_2]$, $Cu^{2+}$ ions are bridged pdt linker by two different sets of coordinating groups sulfur and nitrogen and forms a 3D network.[65] The presence of $Cu^{I}[Cu^{III}(pdt)_2]$ and $Cu^{II}[Cu^{II}(pdt)_2]$ states were considered to be responsible for high electrical conductivity.[65]

### 1.5.4. Through-space

The through-space charge transport occurs via the non-covalent interactions (π-π) between the organic linkers in the frameworks.[66-68] To exhibit considerable electrical conductivity, the stacking between these organic linkers must be the range of effective π-π stacking interaction (~3.5Å). Dincă and coworkers[66] reported a related study with a series of TTF-based MOFs $M_2$(TTFTB) with varying the connecting metal ions ($Mn^{2+}$, $Co^{2+}$, $Zn^{2+}$, $Cd^{2+}$). Among these four MOFs $Cd_2$(TTFTB) showed the highest conductivity $6.79 \times 10^{-4}$ $Scm^{-1}$ in comparison to others ($Mn_2$(TTFTB) $=1 \times 10^{-4}$ and $Co_2$(TTFTB)$= 5 \times 10^{-5}$ $Scm^{-1}$). The results were attributed to the decrease in S---S distance with increasing the size of the cations that results in a higher degree of π-π interaction in the case of $Cd_2$(TTFTB).

### 1.5.5. Guest-promoted electrical conductivity

The porous nature of MOFs that are considered to be a hindrance towards intrinsically conductive MOF construction can be utilized for conductivity enhancement. For instance,

accommodating redox-active guest molecules in the pores that can increase the charge carrier density and mobility will improve conductivity.[54,56] Many redox-active guests[54,56] such as iodine,[69,70] organic molecules,[71,72,] and conductive polymers[73,74] are the most used guests to enhance the conductivity. Since part of this thesis focuses on polymer guest-induced electrical conductivity improvement, specific examples of the same are discussed here.

Kitagawa and co-workers[73] reported the conductivity enhancement of MIL-101(Cr) upon polymerization of 3,4-ethylenedioxythiophene (EDOT) in the MOF pores. This investigation demonstrated that the conductivity in this particular case is highly dependent on the loading percentage of the monomer. The highest monomer loaded (57%) MIL-101(Cr) showed outstanding improvement on the electrical conductivity from $10^{-11}$ $Scm^{-1}$ (pristine) to $10^{-3}$ $Scm^{-1}$ (polymerized MOF). Ballav and co-workers[74] investigated the conductivity changes upon accommodating different polymers PEDOT and PPy in the cavity of UiO-66. The conductivity of UiO-66 increased drastically from $10^{-8}$ $Scm^{-1}$ to $10^{-2}$ $Scm^{-1}$ and $10^{-4}$ $Scm^{-1}$ for the polymerized composites UiO-66-PEDOT and UiO-66-PPy, respectively.[74] In both studies, the increased charge transport efficiency for the presence of conductive polymers was considered to be the reason for the enhancement of conductivity.

## 1.6.Applications of MOFs

### 1.6.1. Gas storage and separations

#### $H_2$ storage

$H_2$ has been considered as an alternative to fossil fuels for automobile energy supplies since it generates a cleaner byproduct ($H_2O$). In addition, $H_2$ has the highest energy per mass in comparison to any other fuel.[75] Current techniques to store $H_2$ under high pressure in cryogenic liquid $H_2$ tanks involve issues that include -large energy consumption for $H_2$ liquification and maintaining the tank at low temperature, leakage problem, and safety, low volumetric and gravimetric densities.[75-77] One of the major challenges is the low volumetric energy density at ambient operating conditions in the vehicle.[75,78] Therefore, it is necessary to develop methods for storing $H_2$ at or near ambient temperature.

MOFs have attracted considerable interest in this regard as a potential material to store $H_2$ due to their very high surface area, porosity, and tunability at the pores.[5,79-82] Although the interactions between $H_2$ and the MOFs are typically weak Van der Waals interactions, the presence of open metal sites in the frameworks available for direct binding to $H_2$ is crucial for high-density $H_2$ storage.[79] Yaghi and co-workers[80] first reported the $H_2$ storage capability (uptake capacity 10 wt%, at 77 K and 100 bars) of MOF-5. Since then, a large number of MOFs have been reported with their $H_2$ storage capacity. However, for most of the MOFs, the storage capacity was investigated at 77K and at pressure up to 100 bar because the Van der Waals interactions are very weak and decrease with the increase of temperature. These studies showed that the storage capacity is proportionally dependent on the surface area and pore volume of the MOFs.[76,79]

**$CO_2$ Separation**

With the increasing population and energy demand, the dependency on fossil fuels increases day by day. As a consequence, the emission of $CO_2$ is going higher and has already been a threat to global warming. Therefore, the development of materials for the efficient capture of $CO_2$ is urgent. The widely used technique[76,79] to remove $CO_2$ is based on the use of aqueous amine solution. However, this technique suffers from high regeneration temperature and lack of reversibility due to the strong binding of $CO_2$ with amines. Therefore, the development of reversible physiadsorbent such as MOFs for $CO_2$ capture is in demand.

Due to the large quadrupole moment and polarizability of $CO_2$[76,79], it interacts strongly than other gases such as $N_2$ and $CH_4$ with MOFs pore surfaces decorated with polar functional groups.[76,77] Capturing $CO_2$ selectively with the MOFs that lack polar functionalization or other chemical binding sites (such as the amine group) is tricky due to the comparable kinetic diameters of other gas molecules ($CO_2$ = 3.30, $CH_4$ = 3.76, and $N_2$ = 3.64 Å).[75] In these cases, interpenetrated frameworks showed considerable efficacy towards selective capture of $CO_2$ from the others by molecular sieving. For instance, MOF-508,[83] a double interpenetrated MOF, shows excellent selectivity for $CO_2$ removal at 303 K and 4.5 bar. It captured $CO_2$ from binary ($CO_2/CH_4$, $CO_2/N_2$) and ternary ($CO_2/CH_4/N_2$) gas mixture with the following adsorption capacities: 26.0, 5.5, 3.2 wt% for $CO_2$, $CH_4$, and $N_2$, respectively.[83] Incorporation of amine functionalities or other polar functional groups in the framework can also facilitate selective and efficient binding of $CO_2$, e.g., the $CO_2$ adsorption capacity of Zn(BTZ) is 35.6 wt%.[84]

### 1.6.2. Catalysis

MOFs have attracted substantial attention from the researcher due to the several unique features that MOFs can offer in the field of catalysis. Among them, the high density of active catalytic sites in high internal surface area has been considered as one of the crucial for high reaction rate.[85,86] Others include synthetic tunability, post-synthetic incorporation of active sites, shape-selective catalysis, swift transport of the reactant due to the presence of large pore are important factors in developing MOF-base catalysts.[85,86] Although significant numbers of MOFs have been reported that exhibit catalytic activity for different reactions, the poor stability of many MOFs at high temperatures often limits their industrial applications.[86] However, a wide number of MOFs show excellent catalytic activities for the reaction that occurs at moderate temperatures and do not require catalyst regeneration.[86]

**Hydrogenation of $CO_2$**

$CO_2$ contributes to global warming and needs to be urgently removed or converted to some useful chemicals such as methanol to mitigate its accumulation in the atmosphere. In this instance, Yaghi and co-workers[87] utilize a MOF-based catalyst consisting of Cu-nanoparticle (18 nm) encapsulated in the UiO-66 ($Zr6O_4(OH)_4(BDC)_6$). This catalyst showed 100% selectivity for the conversion of $CO_2$ to methanol at 175 °C, which is 8-fold higher than the widely used $Cu/ZnO/Al_2O_3$ catalyst at the respective temperature.[87] The strong interaction between Cu nanoparticles with the Zr oxide SBUs in the framework and the presence of Cu at its multiple oxidation states and the absence of nanoparticle accumulation are considered to be responsible for the higher selectivity for methanol

generation.[87] Lin and co-workers[88] reported that another Zr-based UiO-bpy MOF contained Cu/ZnOx nanoparticles (<1 nm) to convert $CO_2$ to methanol efficiently. The CuZn@Uio-bpy showed 100% selectivity for methanol at 200-250 °C, which is significantly higher than catalyst $Cu/ZnO/Al_2O_3$ (54.8%, at 250 °C).[88] This result was attributed to the prevention of nanoparticle agglomeration and phase separation due to strong interactions between the $Cu/ZnO_x$ and the bpy, and $Zr_6$ SBUs.

**Photocatalysis**

The incorporation of photoactive linkers/sites to MOF frameworks enables them to use in photocatalysis. Guo and co-workers,[89] reported evolution of $H_2$ using visible-light-driven photocatalysis with x%-MIL-125-$(SCH_3)_2$ MOF. This MOF obtained by linker replacement of $H_2BDC$ with $H_2BDC$-$(SCH_3)_2$ in the MIL-125 significantly reduces the resulting MOF's bandgap from 3.8 eV to 2.6 eV. For the photocatalytic generation of $H_2$, a cocatalyst (Pt) and electron donor triethanolamine (TEOA) were used in the catalytic system.[89] This hybrid material displayed high $H_2$ production as 3814.0 $\mu molg^{-1}h^{-1}$ upon irradiation at 425 nm, which is an order of magnitude higher than that of the leading-edge Pt/MOF photocatalyst derived from aminoterephthalate.[89]

### 1.6.3. Sensing applications of LMOFs

Detection of various analytes using LMOF sensor materials depends on the interaction of the analytes and the MOF. The pore's size, shape, and chemical environment must be appropriate to accommodate analytes of interest and interact with them. In order to act as an efficient sensor materials LMOFs must display measurable changes in the emission

specific to the analyte and reversible response (required in most cases). A wide number of LMOFs fulfill these requirements and offer easy detection of luminescent changes; therefore, the potential of LMOFs for sensing various ions, explosives, and toxic chemicals has been well investigated by researchers.[10,12-14,90] Among many of these applications, toxic metal ions ($Hg^{2+}$ and $Pb^{2+}$) and nitroaromatic explosives sensing are discussed in this dissertation**.**

**$Hg^{2+}$-sensing**

$Hg^{2+}$ is one of the toxic metal ions that can be present as a contaminant in the drinking water. The widespread $Hg^{2+}$ contamination comes from chemical industries and mines. Toxicity from $Hg^{2+}$, when present in the drinking water higher than the permissible limit of 2 ppb, can cause severe health problems ranging from kidney damage to death. Therefore, it is vital to remove $Hg^{2+}$ from the drinking water efficiently. In this regard, several LMOFs containing mercury-specific functional groups have been used for efficient detection, and in some cases, removal.

In a related study, Xu and coworkers[9] constructed a thiol laced-Zr MOF by connecting 2,5-dimercapto-1,4-benzenedicarboxylic acid ($H_2$DMBD) via $Zr^{4+}$ metal ion. Due to the soft acid-base interaction between $Hg^{2+}$ and sulfur, this MOF displayed excellent $Hg^{2+}$ uptake capacity in aqueous solution (concentration below 0.01 ppm = 10 ppb). Wen and coworkers[91] reported two MOFs built from the 2-$NH_2$bdc (2-amino-1,4-benzenedicarboxylic acid) and bibp (4,4′-bis(imidazol-1-ylmethyl)-biphenyl) (1) and tib (1,3,5-tris(1-imidazolyl)benzene) (2) organic linkers and $Zn^{2+}$ and $Cd^{2+}$ respectively. In

both MOFs the amino groups in the 2-$NH_2$bdc are not coordinated to the framework building metal ions; therefore, they were available for $Hg^{2+}$ binding. Both MOFs displayed excellent selectivity towards $Hg^{2+}$ over the other cations tested and detectability as low as $4.2 \times 10^{-8}$ M (~2 ppb) in an aqueous solution with the latter.

**$Pb^{2+}$ Sensing**

Liu and coworkers[92] investigated the cation sensing capabilities of a lanthanide-based MOF constructed from $Tb^{3+}$ and 3,5-dicarboxyphenol anion ligand that displayed "antenna sensitization"-based luminescent. This Tb-MOF exhibited very high selectivity towards $Pb^{2+}$ over several other cations investigated and is capable of detecting (detection limit $10^{-7}$ M) $Pb^{2+}$ from extremely low concentration solution in water. The selectivity towards $Pb^{2+}$ was attributed to the strong electrostatic interaction between $Pb^{2+}$ and the phenolic oxygen in the framework due to the electronic structure of $Pb^{2+}$. This interaction perturbed the efficiency of energy transfer from the linker to $Tb^{3+}$ and thereby quenched the emission intensity.

**Explosive sensing**

LMOFs have attracted substantial interest from researchers for their potential as sensor materials in explosive detection.[10,11,14] The reason behind this is LMOFs offer very fast and easy detectability (changes in luminescence), portability, and low cost in comparison to the present analytical techniques such as energy dispersive x-ray diffraction (EDXRD), plasma desorption mass spectrometry (PDMS), etc.[10,14] for explosive detection. In this instance, Li

and coworkers[93] reported the first LMOF $Zn_2(bpdc)_2(bpee)$ (bpdc=4,4'-biphenyldicarboxylate; bpee=1,2-bipyridylethene) that was investigated for nitroaromatic 2,4-Dinitrotoluene (DNT), 2,3-dimethyl-2,3-dinitrobutane (DMNB) sensing from the vapor phase.[93] This LMOF displayed very quick and high percentage quenching of emission intensities within 10 seconds in the presence of the DNT and DMNB. The microsize porous nature of the MOF and strong interaction between the framework and analytes that caused excited state electron transfer from the MOF to DNT and DMNB were considered to be the basis for the outstanding detection. [93]

Gosh and coworkers[94] reported detection of TNP (2,3,5-trinitro phenol) from the aqueous solution using a bio-MOF-1, $[Zn_8(ad)_4(BPDC)_6O{\cdot}2\ Me_2NH_2]$ (ad=adenine, BPDC=biphenyl dicarboxylic acid). The bio-MOF-1 showed outstanding selectivity for TNP (detection limit 2.9 ppb) over the other nitroaromatics due to H-bonding interactions between TNP and the amino group from the adenine moiety in the pores.

## 1.7.Overview of this dissertation

The second chapter presents a construction of a new luminescent MOFs, and it's Hg(II) sensing capability. This study also describes the utilization of two organic ligands with overlapping absorption-emission profiles to yield ligand-to-ligand energy transfer in the resulting MOF.

The third chapter describes the construction of a MOF-74 analog with an electron deficient ligand and lowering its bandgap by approximately 1 eV upon complimentary guest (electron-rich) encapsulation.

The fourth chapter presents the guest-promoted electrical conductivity improvement of an insulating MOF. In this study, the monomer EDOT (3,4-ethylenedioxythiophene) and Py (pyrrole) are the first loaded in the MOF cavity and in-situ polymerized. The resulting MOF-polymer composites obtained from this study exhibit significantly higher electrical conductivity than the pristine MOF.

## 1.7.References


1. Furukawa, H.; Cordova, K. E.; O'Keeffe, M.; Yaghi, O. M. The Chemistry and Applications of Metal-Organic Frameworks. *Science* **2013**, *341*, 1230444:1–12.
2. Yaghi, O. M.; Li, H. Hydrothermal Synthesis of a Metal-Organic Framework Containing Large Rectangular Channels. *J. Am. Chem. SOC.* **1995,** *117,* 10401–10402.
3. Kitagawa, S.; Kitaura, R.; Noro, S.-I. Functional Porous Coordination Polymers. *Angew. Chem. Int. Ed*. **2004**, *43*, 2334 –2375.
4. Farha, O. K.; Hupp, J. T. Rational Design, Synthesis, Purification, and Activation of Metal-Organic Framework Materials. *Acc. Chem. Res.* **2010,** *43,* 1166–1175.
5. Furukawa, H.; Ko, N.; Go, Y. B.; Aratani, N.; Choi, S. B.; Choi, E.; Yazaydin, Ö.; Snurr, R. Q.; O′Keeffe, M.; Kim, J.; Yaghi, O. M. Ultrahigh Porosity in Metal-Organic Frameworks. *Science* **2010**, *329*, 424–428.
6. Eddaoudi, M.; Kim, J.; Rosi, Nathaniel.; Vodak, D.; Wachter, J.; O'Keeffe, M.; Yaghi, O. M. Systematic Design of Pore Size and Functionality in Isoreticular MOFs and Their Application in Methane Storage. *Science* **2002,** *295,* 469–472.
7. Song, Y.-F.; Cronin, L. Postsynthetic Covalent Modification of Metal–Organic Framework (MOF) Materials. *Angew. Chem. Int. Ed.* **2008,** *47,* 4635 – 4637.
8. Kandiah, M.; Usseglio, S.; Svelle, S.; Olsbye, U.; Lillerudb, K. P.; Tilset, M. Post-synthetic modification of the metal–organic framework compound UiO-66. *J. Mater. Chem.* **2010,** *20,* 9848–9851.

9. Yee, K.-K.; Reimer, N.; Liu, J.; Cheng, S.-Y.; Yiu, S.-M.; Weber, J.; Stock, N.; Xu, Z. Effective Mercury Sorption by Thiol-Laced Metal−Organic Frameworks: in Strong Acid and the Vapor Phase. *J. Am. Chem. Soc.* **2013,** *135,* 7795–7798.
10. Zhao, D.; Cui, Yuanjing, Yang, Y.; Qian, G. Sensing-functional luminescent metal–organic Frameworks. *CrystEngComm,* **2016**, *18,* 3746–3759.
11. Xu, H.; Cao, C.-S.; Kanga, X.-M.; Zhao, B. Lanthanide-based metal–organic frameworks as luminescent probes. *Dalton Trans.,* **2016,** *45,* 18003–18017.
12. Cui, Y.; Yue, Y.; Qian, G.; Chen, B. Luminescent Functional Metal-Organic Frameworks. *Chem. Rev*. **2012,** *112,* 1126–1162.
13. Allendorf, M. D.; Bauer, C. A.; Bhakta, R. K.; Houk, R. J. T. Luminescent metal–organic frameworks. *Chem. Soc. Rev.,* **2009**, *38,* 1330–1352.
14. Lustig, W. P.; Mukherjee, S.; Rudd, N. D.; Desai, A. V.; Li, J.; Ghosh, S. K. Metal–organic frameworks: functional luminescent and photonic materials for sensing applications. *Chem. Soc. Rev.,* **2017,** *46,* 3242–3285.
15. Fateeva, A.; Chater, P. A.; Ireland, C. P.; Tahir, A. A.; Khimyak, Y. Z.; Wiper, P. V.; Darwent, J. R.; Rosseinsky, M. J. A Water-Stable Porphyrin-Based Metal–Organic Framework Active for Visible-Light Photocatalysis. *Angew. Chem. Int. Ed*. **2012,** *51,* 7440–7444.
16. Liu, J.; Chen, L.; Cui, H.; Zhang, J.; Zhang, L.; Su, C.-Y. Applications of metal–organic frameworks in heterogeneous supramolecular catalysis. *Chem. Soc. Rev.* **2014,** *43,* 6011–6061.

17. Stavila, V.; Talin, A.; Allendorf, M. D. MOF-based electronic and optoelectronic devices. *Chem. Soc. Rev.* **2014,** *43,* 5994–6010.

18. Dolgopolova, E. A.; Shustova, N. B. Metal-Organic Frameworks Photophysics: Optoelectronic Devices, Photoswitches, Sensor, and Photocatalysts. *MRS Bull.* **2016,** *41,* 890–896.

19. Yang, Y.; Zhao, Q.; Feng, w.; Li, F. Luminescent Chemodosimeters for Bioimaging. *Chem. Rev.* **2013,** *113,* 192−270.

20. Rocca, J. D.; Liu, D.; Lin, W. Nanoscale Metal-Organic Frameworks for Biomedical Imaging and Drug Delivery. *Acc. Chem. Res.* **2011,** *44,* 957–968.

21. Eddaoudi, M.; Moler, D. B.; Li, H.; Reineke, T. M.; O'Keeffe, M.; Yaghi, O. M. Modular Chemistry: Secondary Building Units as a Basis for the Design of Highly Porous and Robust Metal-Organic Carboxylate Frameworks. *Acc. Chem. Res*. **2001,** *34*, 319–330.

22. Kitagawa, S.; Kitaura, R.; Noro, S-i. Functional Porous Coordination Polymers. *Angew. Chem. Int. Ed*. **2004**, *43*, 2334 –2375.

23. Tranchemontagne, D. J.; Mendoza-Corte's, J. L.; O'Keeffe, M.; Yaghi, O. M. Secondary building units, nets and bonding in the chemistry of metal-organic frameworks. *Chem. Soc. Rev*., **2009**, *38*, 1257–1283.

24. Kalmutzki, M. J.; Hanikel, N.; Yaghi, O. M. Secondary building units as the turning point in the development of the reticular chemistry of MOFs. *Sci. Adv.* **2018**, *4*, 9180:1–16.

25. Férey, F. Hybrid porous solids: past, present, future. *Chem. Soc. Rev*., **2008**, *37*, 191–214.

26. Sun, Y.; Zhou, H-C. Recent progress in the synthesis of metal-organic frameworks. *Sci. Technol. Adv. Mater.* **2015**, *16*, 054202:1–11.

27. Li, H.; Eddaoudi, M.; O'Keeffe, M. O.; Yaghi, O. M. Design and synthesis of an exceptionally stable and highly porous metal-organic framework. *Nature*, **1999**, *402*, 276–279.

28. Furukawa, H.; G′andara, F.; Zhang, Y-B.; Jiang, J.; Queen, W. L.; Hudson, M. R.; Yaghi, O. M. Water Adsorption in Porous Metal−Organic Frameworks and Related Materials. *J. Am. Chem. Soc.* **2014**, *136*, 4369−4381.

29. Lee, C. Y.; Farha, O. M.; Hong, B. J.; Sarjeant, A. A.; Nguyen, S. T.; Hupp, J. T. Light-Harvesting Metal-Organic Frameworks (MOFs): Efficient Strut-to-Strut Energy Transfer in Bodipy and Porphyrin-Based MOFs. *J. Am. Chem. Soc*. **2011**, *133*, 15858–15861.

30. Feng, D.; Gu, Z-Y.; Li, J-R.; Jiang, H-L.; Wei, Z.; Zhou, H-C. Zirconium-Metalloporphyrin PCN-222: Mesoporous Metal-Organic Frameworks with Ultrahigh Stability as Biomimetic Catalysts. *Angew. Chem. Int. Ed*. **2012**, *51*, 10307 –10310.

31. Gangu, K. K.; Maddila, S.; Saratchandra Babu Mukkamala, S. B.; Jonnalagadda, S. B. A review on contemporary Metal-Organic Framework materials. *Inorganica Chimica Acta* **2016**, *446*, 61–74.

32. Hwang, Y. K.; Chang, J-S.; Park, S-E.; Kim, D. S.; Kwon, Y-U.; Jhung, S. H.; Hwang, J-S.; Park, M. S. Microwave Fabrication of MFI Zeolite Crystals with a Fibrous Morphology and Their Applications. *Angew. Chem. Int. Ed.* **2005**, *44*, 556 –560.
33. Jhung, S.; Lee, J-H.; Forster, P. M.; Férey, G.; Cheetham, A. K.; Chang, J-S. Microwave Synthesis of Hybrid Inorganic–Organic Porous Materials: Phase-Selective and Rapid Crystallization. *Chem. Eur. J.* **2006**, *12*, 7899 – 7905.
34. Horcajada, P.; Chalati, T.; Serre, C.; Gillet, B.; Sebrie, C.; Baati, T.; Eubank, J. F.; Heurtaux, D.; Clayette, P.; Kreuz, C.; Chang, J-S.; Hwang, Y. K.; Marsaud, V.; Bories, P-N.; Cynober, L.; Gil, S.; Férey, G.; Couvreur, P.; Gref, R. Porous metal–organic-framework nanoscale carriers as a potential platform for drug delivery and imaging. *NATURE MATERIALS* **2010**, *9*, 172–178.
35. Safaei, M.; Foroughi, M. M.; Ebrahimpoor, N.; Jahani, S.; Omidi, A.; Khatami, M. A review on metal-organic frameworks: Synthesis and applications. *Trends in Analytical Chemistry* **2019**, *118*, 401–425.
36. Mueller, U.; Puetter, H.; Hesse, M.; Wessel, H. METHOD FOR ELECTROCHEMICAL PRODUCTION OF A CRYSTALINE POROUS METAL ORGANIC SKELETON MATERIAL. 2005 Patent WO 2005/049892.
37. Campagnol, N.; Assche, T. V.; Boudewijns,T.; Denayer, J.; Binnemans, K.; Vos, D. D.; Fransaer, J. High pressure, high temperature electrochemical synthesis of metal–organic frameworks: films of MIL100 (Fe) and HKUST-1 in different morphologies. *J. Mater. Chem. A*, **2013**, *1*, 5827–5830.

38. Li, M.; Dincă, M. Selective formation of biphasic thin films of metal–organic frameworks by potential-controlled cathodic electrodeposition. *Chem. Sci*., **2014**, *5*, 107–111.

39. Stassen, I.; Styles, M.; Assche, T. V.; Campagnol, N.; Fransaer, J.; Denayer, J.; Tan, J-C.; Falcaro, P.; Vos, D. D.; Ameloot, R. Electrochemical Film Deposition of the Zirconium Metal−Organic Framework UiO-66 and Application in a Miniaturized Sorbent Trap. *Chem. Mater*. **2015**, *27*, 1801−1807.

40. Williams, D. E.; Rietman, J. A.; Maier, J. M.; Tan, R.; Greytak, A. B.; Smith, M. D.; Krause, J. A.; Shustova, N. B. Energy Transfer on Demand: Photoswitch-Directed Behavior of Metal−Porphyrin Frameworks. *J. Am. Chem. Soc.* **2014**, *136,* 11886−11889.

41. Lee, C. Y.; Farha, O. K.; Hong, B. J.; Sarjeant, A. A.; Nguyen, S. T.; Hupp, J. T. Light-Harvesting Metal-Organic Frameworks (MOFs): Efficient Strut-to-Strut Energy Transfer in Bodipy and Porphyrin-Based MOFs. *J. Am. Chem. Soc.* **2011,** *133,* 15858–15861.

42. So, M. C.; Weiderrecht, G. P.; Mondloch, J. E.; Hupp, J. T.; Farha, O. K. Metal–organic framework materials for light-harvesting and energy transfer. *Chem. Commun.* **2015,** *51,* 3501–3510.

43. Son, H.-J.; Jin, S.; Patwardhan, S.; Wezenberg, S. J.; Jeong, N. C.; So, M.; Wilmer, C. E.; Sarjeant, A. A.; Schatz, G. C.; Snurr, R. Q.; Farha, O. K.; Wiederrecht, G. P.; Hupp, J. T. Light-Harvesting and Ultrafast Energy Migration in Porphyrin-Based Metal-Organic Frameworks. *J. Am. Chem. Soc.* **2013,** *135,* 862–869.

44. Dolgopolova, E. A.; Williams, D. E.; Greytak, A. B.; Rice, A. M.; Smith, M. D.; Krause, J. A.; Shustova, N. B. A Bio-inspired Approach for Chromophore Communication: Ligand-to-Ligand and Host-to-Guest Energy Transfer in Hybrid Crystalline Scaffolds. *Angew. Chem. Int. Ed*. **2015,** *54,* 13639–13643.

45. Williams, D. E.; Shustova, N. B. Metal-Organic Frameworks as a Versatile Tool to Study and Model Energy Transfer Processes. *Chem. Eur. J.* **2015,** *21,* 15474–15479.

46. Dolgopolova, E. A.; Rice, A. M.; Martin, C. R.; Shustova, N.B. Photochemistry and photophysics of MOFs: steps towards MOF-based sensing enhancements. *Chem. Soc. Rev.* **2018,** *47,* 4710–4728.

47. Zhang, Q.; Zhang, C.; Cao, L.; Wang, Z.; An, B.; Lin, Z.; Huang, R.; Zhang, Z.; Wang, C.; Lin, W. Förster Energy Transport in Metal–Organic Frameworks is beyond Step-by-Step Hopping. *J. Am. Chem. Soc.* **2016,** *138,* 5308–5315.

48. Li, B.; Zhang, Y.; Ma, D.; Shi, Z.; Ma, S. Mercury Nano-Trap for Effective and Efficient Removal of Mercury(II) from Aqueous Solution. *Nat. Commun.* **2014,** *5,* 5537.

49. Lin, R.-B.; Liu, S.-Y.; Ye, J.-W.; Li, X.-Y.; Zhang, J.-P. Photoluminescent Metal–Organic Frameworks for Gas Sensing. *Adv. Sci.* **2016**, *3*, 1500434:1–20.

50. So, M. C.; Wiederrecht, G. P.; Mondloch, J. E.; Hupp, J. T.; Farha, O. M. Metal–organic framework materials for light-harvesting and energy transfer. *Chem. Commun.,* **2015**, *51*, 3501–3510.

51. Manna, B.; Singh, S.; Karmakar, A.; Desai, A. V.; Ghosh, S. K. Selective Anion Exchange and Tunable Luminescent Behaviors of Metal−Organic Framework Based Supramolecular Isomers. *Inorg. Chem*. **2015**, *54*, 110−116.

52. Kreno, L. E.; Leong, K.; Farha, O. M.; Allendorf, M.; Duyne, R. P. V.; Hupp, J. T. Metal-Organic Framework Materials as Chemical Sensors. *Chem. Rev.* **2012**, *112*, 1105–1125.

53. Zhang, T.; Lin, W. Metal–organic frameworks for artificial photosynthesis and photocatalysis. *Chem. Soc. Rev*., **2014**, *43*, 5982–5993.

54. Xie, L. S.; Skorupskii, G.; Dincă, M. Electrically Conductive Metal−Organic Frameworks. *Chem. Rev*. **2020**, *120*, 8536−8580.

55. Sun, L.; Campbell, M. G.; Dincă, M. Electrically Conductive Porous Metal–Organic Frameworks. *Angew. Chem. Int. Ed*. **2016**, *55*, 3566 – 3579.

56. Nidamanuri, N.; Maity, K.; Saha, S. Electrically Conductive Metal-Organic Frameworks: Elaboration and Applications of Meta-Organic Frameworks; World Scientific, 2018; pp 655-686.

57. D'Alessandro, D. M.; Kanga, J. R. R.; Caddy, J. S. Towards Conducting Metal-Organic Frameworks. *Aust. J. Chem.* **2011**, *64*, 718–722.

58. Sun, L.; Miyakai, T.; Seki, S.; Dincă, M. $Mn_2$(2,5-Disulfhydrylbenzene-1,4-Dicarboxylate): A Microporous Metal−Organic Framework with Infinite (−Mn−S−)∞ Chains and High Intrinsic Charge Mobility. *J. Am. Chem. Soc*. **2013**, *135*, 8185−8188.

59. Xie, L. S.; Sun, L.; Wan, R.; Park, S. S.; DeGayner, J. A.; Hendon, C. H.; Dincă, M. Tunable Mixed-Valence Doping toward Record Electrical Conductivity in a Three-Dimensional Metal−Organic Framework. *J. Am. Chem. Soc*. **2018**, *140*, 7411−7414.

60. Day, R. W.; Bediako, D. K.; Rezaee, M.; Parent, L. R.; Skorupskii, G.; Arguilla, M. Q.; Hendon, C. H.; Stassen, I.; Gianneschi, N.; Kim, P.; et al. Single Crystals of Electrically Conductive 2D MOFs: Structural and Electrical Transport Properties. *ACS Cent. Sci*. **2019**, *5,* 1959−1964.

61. Dou, J. H.; Sun, L.; Ge, Y.; Li, W.; Hendon, C. H.; Li, J.; Gul, S.; Yano, J.; Stach, E. A.; Dincă, M. Signature of Metallic Behavior in the Metal-Organic Frameworks $M_3$(Hexaiminobenzene)$_2$ (M = Ni, Cu). *J. Am. Chem. Soc*. **2017**, *139*, 13608−13611.

62. Sun, L.; Hendon, C. H.; Park, S. S.; Tulchinsky, Y.; Wan, R.; Wang, F.; Walsh, A.; Dincă, M. Is Iron Unique in Promoting Electrical Conductivity in MOFs? *Chem. Sci*. **2017**, *8*, 4450−4457.

63. Dong, R.; Han, P.; Arora, H.; Ballabio, M.; Karakus, M.; Zhang, Z.; Shekhar, C.; Adler, P.; Petkov, P. S.; Erbe, A.; Mannsfeld, S. C. B.; Felser, C.; Heine, T.; Bonn, M.; Feng, X.; Cánovas, E. High Mobility Band-like Charge Transport in a Semiconducting Two-Dimensional Metal−Organic Framework. *Nat. Mater.* **2018**, *17*, 1027−1032.

64. Sun, L.; Hendon, C. H.; Minier, M. A.; Walsh, A.; Dincă, M. Million-Fold Electrical Conductivity Enhancement in Fe2(DEBDC) versus Mn2(DEBDC) (E = S, O). *J. Am. Chem. Soc*. **2015**, *137*, 6164−6167.

65. Takaishi, S.; Hosoda, M.; Kajiwara, T.; Miyasaka, H.; Yamashita, M.; Nakanishi, Y.; Kitagawa, Y.; Yamaguchi, K.; Kobayashi, A.; Kitagawa, H. Electroconductive Porous Coordination Polymer Cu[Cu(pdt)$_2$] Composed of Donor and Acceptor Building Units. *Inorg. Chem.* **2009**, *48*, 9048–9050.

66. Park, S. S.; Hontz, E. R.; Sun, L.; Hendon, C. H.; Walsh, A.; Voorhis, T. V.; Dincă, M. Cation-Dependent Intrinsic Electrical Conductivity in Isostructural Tetrathiafulvalene-Based Microporous Metal−Organic Frameworks. *J. Am. Chem. Soc*. **2015**, *137*, 1774−1777.

67. Kuang, X.; Chen, S.; Meng, L.; Chen, J.; Wu, X.; Zhang, G.; Zhong, G.; Hu, T.; Li, Y.; Lu, C.-Z. Supramolecular Aggregation of a Redox-Active Copper-Naphthalenediimide Network with Intrinsic Electron Conduction. *Chem. Commun*. **2019**, *55*, 1643−1646.

68. Xie, L. S.; Alexandrov, E. V.; Skorupskii, G.; Proserpio, D. M.; Dincă, M. Diverse π−π Stacking Motifs Modulate Electrical Conductivity in Tetrathiafulvalene-Based Metal−Organic Frameworks. *Chem. Sci*. **2019**, *10*, 8558−8565.

69. Zeng, M.-H.; Yin, Z.; Tan, Y.-X.; Zhang, W.-X.; He, Y.-P.; Kurmoo, M. Nanoporous Cobalt(II) MOF Exhibiting Four Magnetic Ground States and Changes in Gas Sorption upon Post-Synthetic Modification. *J. Am. Chem. Soc*. **2014**, *136*, 4680−4688.

70. Zeng, M.-H.; Wang, Q.-X.; Tan, Y.-X.; Hu, S.; Zhao, H.-X.; Long, L.-S.; Kurmoo, M. Rigid Pillars and Double Walls in a Porous Metal-Organic Framework: Single-Crystal to Single-Crystal, Controlled Uptake and Release of Iodine and Electrical Conductivity. *J. Am. Chem. Soc*. **2010**, *132*, 2561−2563.

71. Talin, A. A.; Centrone, A.; Ford, A. C.; Foster, M. E.; Stavila, V.; Haney, P.; Kinney, R. A.; Szalai, V.; Gabaly, F. E.; Yoon, H. P.; Léonard, F.; Allendorf, M. D. Tunable Electrical Conductivity in Metal-Organic Framework Thin-Film Devices. *Science* **2014**, *343*, 66–69.

72. Guo, Z.; Panda, D. K.; Maity, K.; Lindsey, D.; Parker, T. G.; Albrecht-Schmitt, T. E.; Barreda-Esparza, J. L.; Xiong, P.; Zhou, W.; Saha, S. Modulating electrical conductivity of metal–organic framework films with intercalated guest π-systems. *J. Mater. Chem. C* **2016,** *4,* 894–899.

73. Ouay, B. L.; Boudot, M.; Kitao, T.; Yanagida, T.; Kitagawa, S.; Uemura, T. Nanostructuration of PEDOT in Porous Coordination Polymers for Tunable Porosity and Conductivity. *J. Am. Chem. Soc.* **2016**, *138*, 10088−10091.

74. Jadhav, A.; Gupta, K.; Ninawe, P.; Ballav, N. Imparting Multifunctionality by Utilizing Biporosity in a Zirconium-Based Metal–Organic Framework. *Angew. Chem*. **2020**, *132*, 2235 –2239.

75. Li, H.; Li, L.; Lin, R-B.; Zhou, W.; Zhang, Z.; Xiang, S.; Chen, B. Porous metal-organic frameworks for gas storage and Separation: Status and challenges. *EnergyChem* **2019**, *1*, 100006:1–39.

76. Li, H.; Wang, K.; Sun, Y.; Lollar, C. T.; Li, J.; Zhou, H-C. Recent advances in gas storage and separation using metal–organic frameworks. *Materials Today*, **2018**, *21*, 108–121.

77. Li, X.; Yang, X.; Xue, H.; Pang, H.; Xu, Q. Metal–organic frameworks as a platform for clean energy applications. *EnergyChem,* **2022**, *2*, 100027:1–29.

78. Li, B.; Wen, H.-M.; Yu, Y.; Cui, Y.; Zhou, W.; Chen, B.; Qian, G. Nanospace within metal-organic frameworks for gas storage and separation. *Materials Today Nano* **2018,** *2*, 21–49.

79. Schoedel1, A.; Ji1, Z.; Yaghi, O. M. The role of metal–organic frameworks in a carbon-neutral energy cycle. *NATURE ENERGY* **2016**, *1*, 16043:1–13.

80. Kaye, S. S.; Dailly, A.; Yaghi, O. M.; Long, J. R. Impact of preparation and handling on the hydrogen storage properties of $Zn_4O$(1,4-benzenedicarboxylate)$_3$ (MOF-5). *J. Am. Chem. Soc.* **2007**, *129*, 14176–14177.

81. Farha, O. K.; Wilmer, C. E.; Eryazici, I.; Hauser, B. G.; Par- illa, P. A.; O'Neill, K.; Sarjeant, A. A.; Nguyen, S. T.; Snurr, R. Q.; Hupp, J. T. Designing higher surface area metal–organic frame- works: are triple bonds better than phenyls? *J. Am. Chem. Soc.* **2012**, *134*, 9860–9863.

82. Sumida, K.; Brown, C. M.; Herm, Z. R.; Chavan, S.; Bordiga, S.; Long, J. R. Hydrogen storage properties and neutron scattering studies of $Mg_2$(dobdc)—a metal–organic framework with open $Mg^{2+}$ adsorption sites. *Chem. Commun.* **2011**, *47*, 1157–1159.

83. Bastin, L.; Ba´rcia, P. S.; Hurtado, E. J.; Silva, J. A. C.; Rodrigues, A. E.; Chen, B. A Microporous Metal-Organic Framework for Separation of $CO_2/N_2$ and $CO_2/CH_4$ by Fixed-Bed Adsorption. *J. Phys. Chem. C* **2008**, *112*, 1575-1581.

84. Cui, P.; Ma, Y-G.; Li, H-H.; Zhao, B.; Li, J-R.; Cheng, P.; Balbuena, P. B.; Zhou, H-C. Multipoint interactions enhanced $CO_2$ uptake: a zeolite-like zinc–tetrazole framework with 24-nuclear zinc cages. *J. Am. Chem. Soc.* **2012**, *134*, 18892–18895.

85. Bavykina, A.; Kolobov, N.; Khan, I. S.; Bau, J. A.; Ramirez, A.; Gascon, J. Metal−Organic Frameworks in Heterogeneous Catalysis: Recent Progress, New Trends, and Future Perspectives. *Chem. Rev.* **2020**, *120*, 8468−8535.

86. Yang, D.; Gates, B. C. Catalysis by Metal-Organic Frameworks: Perspective and Suggestions for Future Research. *ACS Catal*. **2019**, *9*, 1779−1798.

87. Rungtaweevoranit, B.; Baek, J.; Araujo, J. R.; Archanjo, B. S.; Choi, K. M.; Yaghi, O. M.; Somorjai, G. A. Copper Nanocrystals Encapsulated in Zr-based Metal−Organic Frameworks for Highly Selective $CO_2$ Hydrogenation to Methanol. *Nano Lett*. **2016**, *16*, 7645−7649.

88. An, B.; Zhang, J.; Cheng, K.; Ji, P.; Wang, C.; Lin, W. Confinement of Ultrasmall Cu/ZnOx Nanoparticles in Metal−Organic Frameworks for Selective Methanol Synthesis from Catalytic Hydrogenation of $CO_2$. *J. Am. Chem. Soc.* **2017**, *139*, 3834−3840.

89. Han, S.-Y.; Pan, D.-L.; Chen, H.; Bu, X.-B.; Gao, Y.-X.; Gao, H.; Tian, Y.; Li, G.-S.; Wang, G.; Cao, S.-L.; Guo, G-C. A Methylthio-Functionalized-MOF

Photocatalyst with High Performance for Visible-Light-Driven $H_2$ Evolution. *Angew. Chem., Int. Ed*. **2018**, *57*, 9864−9869.

90. Samanta, P.; Let, S.; Mandal, W.; Dutta, S.; Ghosh, S. K. Luminescent metal–organic frameworks (LMOFs) as potential probes for the recognition of cationic water pollutants. *Inorg. Chem. Front*., **2020**, *7*, 1801–1821.
91. Wen, L.; Zheng, X.; Lv, K.; Wang, C.; Xu, X. Two Amino-Decorated Metal−Organic Frameworks for Highly Selective and Quantitatively Sensing of $Hg^{II}$ and $Cr^{VI}$ in Aqueous Solution. *Inorg. Chem*. **2015**, *54*, 7133−7135.
92. Ji, G.; Liu, J.; Gao, X.; Sun, W.; Wang, J.; Zhao, S.; Liu, Z. A luminescent lanthanide MOF for selectively and ultra-high sensitively detecting $Pb^{2+}$ ions in aqueous solution. *J. Mater. Chem. A*, **2017**, *5*, 10200–10205.
93. Lan, A.; Li, K.; Wu, H.; Olson, D. H.; Emge, T. J.; Ki, W.; Hong, M.; Li, J. A Luminescent Microporous Metal–Organic Framework for the Fast and Reversible Detection of High Explosives. *Angew. Chem. Int. Ed*. **2009**, *48*, 2334 –2338.
94. Joarder, B.; Desai, A. V.; Samanta, P.; Mukherjee, S.; Ghosh, S. K. Selective and Sensitive Aqueous-Phase Detection of 2,4,6-Trinitrophenol (TNP) by an Amine-Functionalized Metal Organic Framework. *Chem. Eur. J.* **2015**, *21*, 965 – 969.

# CHAPTER TWO

# A DUAL FUNCTIONAL BICHROMOPHORIC LUMINESCENT METAL-ORGANIC FRAMEWORK (LMOF): INTER-LIGAND ENERGY TRANSFER AND $Hg^{2+}$ SENSING

(Permission for Copyright: Reprinted (adapted) with permission from *Inorg. Chem*. **2019**, *58*, 12707−12715. Copyright (2019) American Chemical Society.)

## 2.1.Introduction

Photoinduced cascade electron transfer and energy transfer through preorganized chromophores and donor−acceptor arrays are key steps of light-harvesting mechanisms of photosynthetic plants and bacteria.[1] These well-orchestrated intricate events are not only the primary source of food and energy supplies that propel life on earth but also offer scientists clues for how to design artificial light-harvesting materials that can power and advance human civilization in a sustainable way. The first and foremost criterion for efficient electron/energy transfer events is precise organization of chromophore, donor, and acceptor units with complementary energy levels so that the photons and/or electrons released by the former can be received by the latter.[2] Among various supramolecular and polymeric materials developed to date,[3−6] metal−organic frameworks (MOFs)[7]—a class of crystalline porous coordination networks composed of metal cluster nodes and organic linkers—present one of the most effective ways to organize these components in a highly ordered periodic fashion that can foster efficient energy and electron transfer processes when the requisite criteria are satisfied. Furthermore, tunable reticular structures, porosity,

and chemical and physical properties make MOFs one the most versatile materials that can not only capture and concentrate certain analytes selectively but also exhibit stimuli-responsive behaviors upon specific host−guest interactions.[8] As a result, although much of MOF research in early days largely focused on their size- and shape-selective guest encapsulation, separation, storage, sequestration, and delivery applications,[9−15] the introduction of redox- and photoactive ligands,[15−17] metal ions,[18] and guest molecules[19−21] endowed them with fascinating optical, electronic, and chemical properties,[22,23] unlocking their potential for photocatalysis,[24,25] sensing,[8,26−40] electrical[41−52] and ionic conductivities,[53−61] and light-to-electrical energy conversion.[62−70]

Photoluminescence (PL) is one of the most appealing and useful properties of MOFs. While some frameworks display photoluminescence despite not containing intrinsically emissive components due to ligand rigidification,[8,27] the most effective and tunable luminescent MOFs usually feature luminescent aromatic ligands and lanthanide ions that emit light upon direct or indirect sensitization involving ligand-toligand or ligand-to-metal energy transfer events.[71] Although ligand-to-ligand energy transfer events are most commonly found in porphyrin-based MOFs,[72−78] porphyrins are rather weak fluorophores and very prone to photobleaching. Therefore, there remains a need for porphyrin-free luminescent MOFs that can support energy transfer and display stimuli-responsive emission changes. Diversifying the composition, properties, and functions of light-harvesting MOFs, herein, we report synthesis, PL behavior, and energy transfer and $Hg^{2+}$ sensing capabilities of a new pillared-paddle wheel framework $Zn_2(NDC)_2(DPTTZ)$ featuring 2,6-naphthalele dicarboxylate (NDC) struts and N,N′-di(4 pyridyl)thiazolo-[5,4-

d]thiazole (DPTTZ) pillars (**Figure 2.1**), which are excellent chromophores and fluorophores with complementary absorption and emission characteristics suitable for Förster resonance energy transfer (FRET).[79,80] Although the redox and light-harvesting properties of electron-deficient and luminescent TTZ compounds are well documented in molecular environments, [81,82] they have been rarely incorporated in MOFs[83–85,] and their PL and redox properties have yet to be explored inside crystalline frameworks. The lowest-energy absorption peak of DPTTZ overlaps quite well with the emission peak of NDC, which enables ligand-to ligand FRET and allows the MOF to display exclusively DPTTZ-centric blue emission (~410 nm) irrespective of the excitation wavelength. Control MOFs devoid of either NDC or DPTTZ ligand do not display such energy transfer capability. Furthermore, the PL spectrum of the DPTTZ-based MOF undergoes significant bathochromic shift and quenching in the presence of $Hg^{2+}$ but not with other transition metal ions, making it a promising sensor for this toxic heavy metal ion.

## 2.2.Results and discussions

Despite having strong emissions in dilute solutions, many organic fluorophores often exhibit diminished fluorescence at higher concentrations, as well as in the solid-state, because of self-quenching. On the other hand, in crystalline MOFs, fluorescent ligands can be positioned periodically at certain distances such that their photoluminescence is preserved and even augmented. Taking advantage of this unique structural feature of MOFs, we synthesized a pillared paddle-wheel architecture $Zn_2(NDC)_2(DPTTZ)\cdot(DMF)_2$ (**Figure 2.1a**) using NDC struts as energy donors and DPTTZ pillars as energy acceptors

via a simple solvothermal reaction (vide supra). SXRD analysis revealed that the resulting rod-shaped pale-yellow crystals possessed triclinic unit cells with $P\bar{1}$ space group. The $Zn_2(COO)_4$ paddle wheel nodes formed by NDC struts are located in the ab-planes while the axially coordinated DPTTZ pillars are aligned along the c-axis. The diagonal distances between $Zn_2$ nodes in a given plane are 19.04 and 17.86 Å, and the distance between the $Zn_2$ nodes bridged by DPTTZ pillars is 16.92 Å, that is, the fluorescent ligands are enough separated to avoid self-quenching.[8,70] Furthermore, the large separation and orientation of electron-rich NDC struts and electron-deficient DPTTZ pillars prevent π-donor/acceptor charge-transfer interactions, which could quench their photoluminescence. Interestingly, under the same solvothermal conditions, the reaction of $Zn(NO_3)_2 \cdot 6H_2O$, 1,4-BDC, and DPTTZ yielded $Zn_2(1,4\text{-BDC})_2(DPTTZ)_2 \cdot (DMF)$ framework with orthorhombic unit cell and Iba2 space group (**Figure 2.1b**) instead of a typical cubic pillared-paddle wheel architecture. This framework is analogous to a previously reported[84,85] $[Zn(1,3\text{-BDC})(DPTTZ)]_n$ and featured a different type of $Zn_2$ nodes made of two distorted octahedral Zn-centers, each connected to one chelating and two bridging carboxylate groups in the equatorial plane and two axial DPTTZ ligands. The closest distance between two parallel π-stacked DPTTZ ligands was around 3.6−4 Å, that is, within the range of π−π-interaction. The experimental PXRD patterns of both DPTTZ-based MOFs (**Figure 2.1c** and **d**) were consistent with the corresponding simulated patterns, confirming that they were indeed phase-pure materials and maintained their structural integrity and crystallinity upon activation.

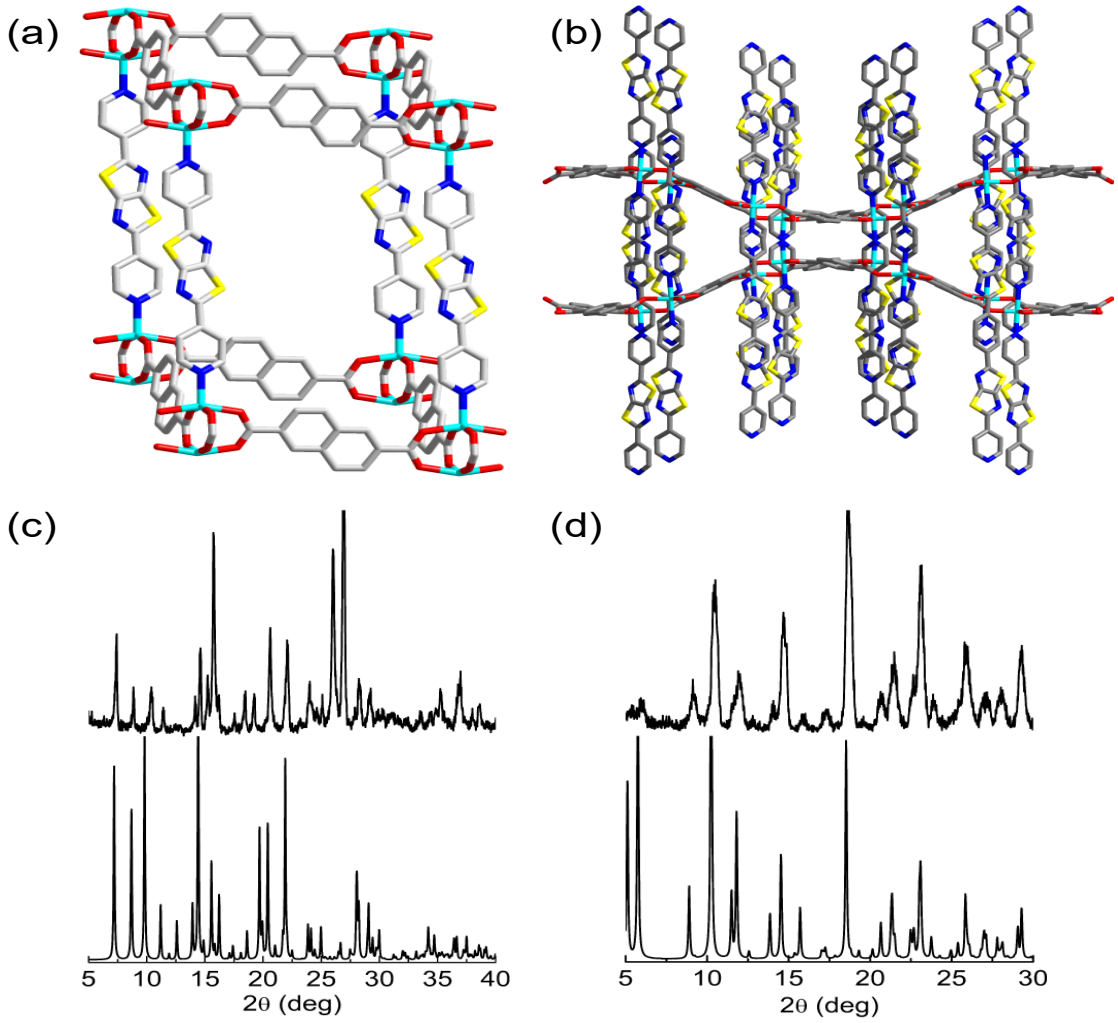


**Figure 2.1:** Single crystal structures of (**a**) $Zn_2(NDC)_2(DPTTZ)$ and (**b**) $Zn_2(1,4\text{-}BDC)_2(DPTTZ)_2$ (cyan: Zn, blue: N, red: O, yellow: S, and grey: C). H atoms and disordered DMF molecules are omitted for clarity. The PXRD profiles of (**c**) $Zn_2(NDC)_2(DPTTZ)$ and (**d**) $Zn_2(1,4\text{-}BDC)_2(DPTTZ)_2$ (bottom simulated, top experimental).

The thermogravimetric and differential scanning calorimetric analyses of $Zn_2(NDC)_2(DPTTZ)$ showed (**Figure 2.2**) that it lost only 5% of initial weight at 125−175 °C possibly due to the loss of residual DMF and remained stable up to 300 °C (30% weight loss). The TGA-DSC profiles of $Zn_2(1,4\text{-}BDC)_2(DPTTZ)_2$ framework showed gradual weight loss (10%) between 130−230 °C and a significant drop above 330 °C, indicating it also has reasonable thermal stability up to that temperature.

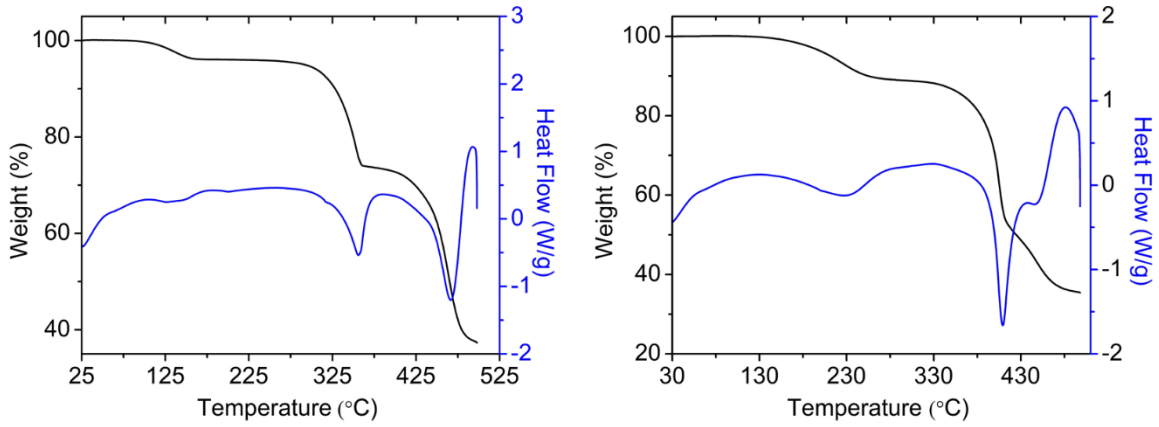


**Figure 2.2:** The TGA (black) and DSC (blue) profiles of $Zn_2(NDC)_2(DPTTZ)$ (left) and $Zn_2(1,4\text{-}BDC)_2(DPTTZ)_2$ (right).

Both frameworks displayed type-I $CO_2$- sorption isotherms (**Figure 2.3**), from which their Brunauer−Emmett−Teller (BET) surface areas and pore volumes were estimated. The surface area and pore volume of $Zn_2(NDC)_2(DPTTZ)$ are 106.8 $m^2/g$ and $6.6 \times 10^{-2}$ $cm^3/g$, respectively, and those for $Zn_2(1,4\text{-}BDC)_2(DPTTZ)_2$ are 113.4 $m^2/g$ and

$7.8 \times 10^{-2}$ $cm^3/g$, respectively. Thus, both materials displayed comparable porosity despite having significant structural differences.

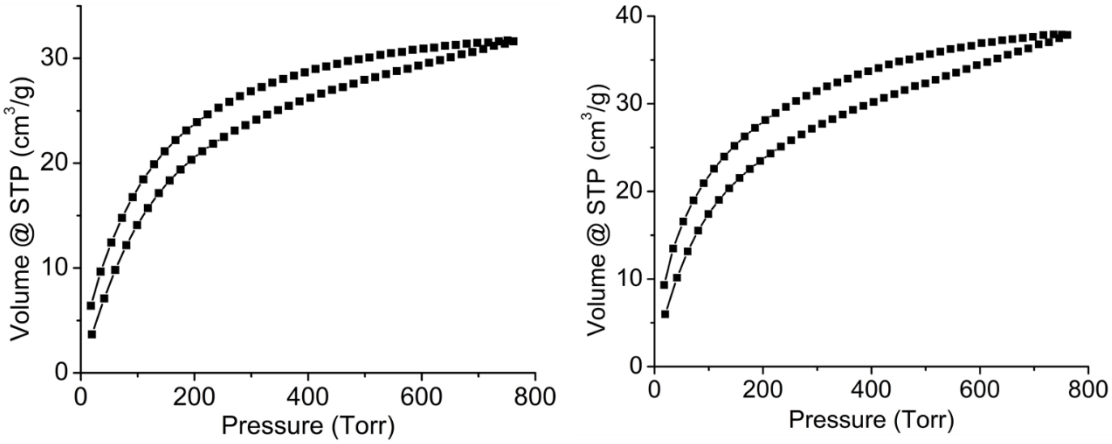


**Figure 2.3:** $CO_2$-sorption isotherms of $Zn_2(NDC)_2(DPTTZ)$ (left) and $Zn_2(1,4\text{-}BDC)_2(DPTTZ)_2$ (right).

The excitation and emission spectra (**Figure 2.4a**) of NDC and DPTTZ ligands revealed excellent overlap between the emission peak of the former and the excitation (absorption) peak of the latter, which bodes well for ligand-to-ligand FRET. Upon excitation of NDC at 330 or 350 nm, it displayed an emission spectrum featuring two sharp peaks 360 and 375 nm and a prominent shoulder at ~400 nm, which overlapped quite well with the intense lowest energy excitation peak of DPTTZ at 390 nm responsible for $S_0 \rightarrow S_1$ transition. Upon its excitation at 390 nm, DPTTZ exhibits a strong emission peak at 410 nm. As a result, irrespective of the excitation wavelengths, a 1:1 NDC/ DPTTZ solution

mixture displayed (**Figure 2.4b**) only DPTTZ centric emission (410 nm) and none from NDC at a shorter wavelength, indicating that NDC struts acted as antenna chromophores.

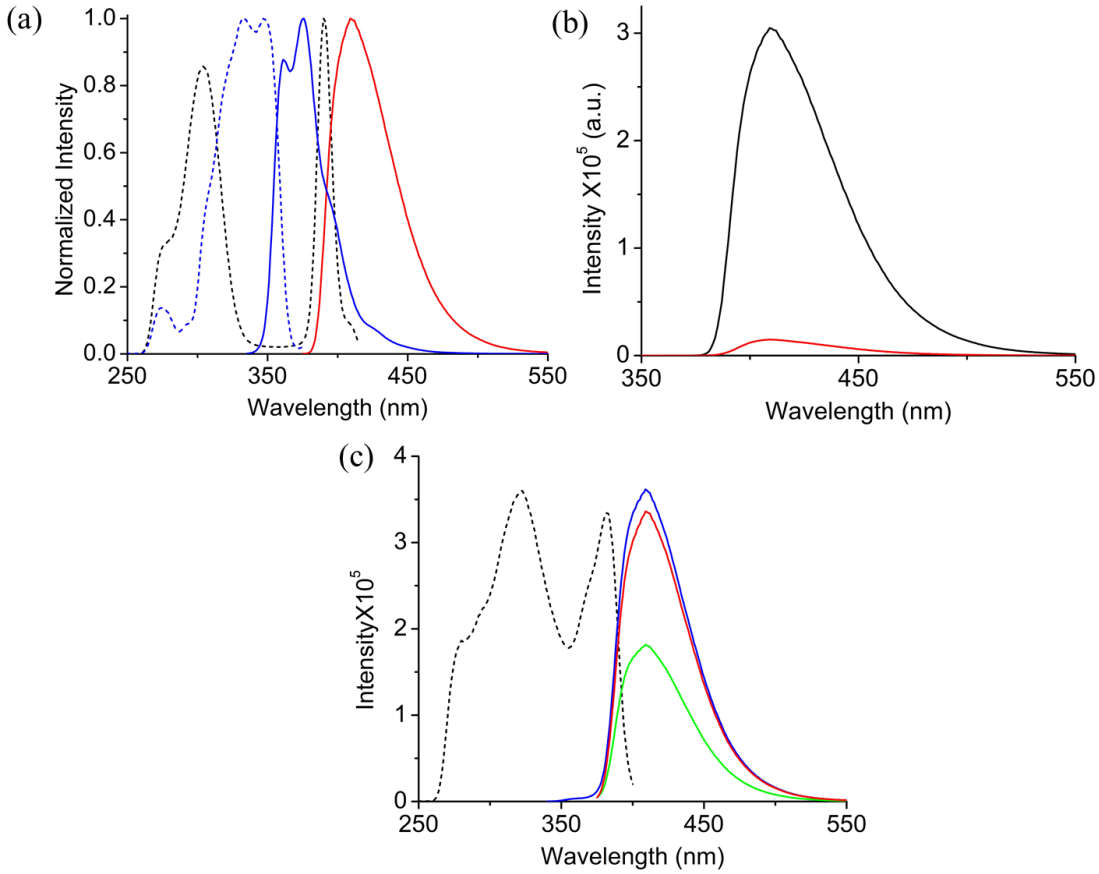


**Figure 2.4:** (a) Excitation (dashed lines) and emission (solid lines) spectra of free NDC (blue) and DPTTZ (red) ligands showing the requisite spectral overlap for FRET. (b) The PL spectra of 1:1 NDC/DPTTZ solution in DMF upon excitation at 350 (red) and 390 nm (black). (c) Excitation (dashed black line) and emission spectra of $Zn_2(NDC)_2(DPTTZ)$ showing exclusively DPTTZ-centric emission regardless of excitation wavelengths ($\lambda_{Ex}$ = 320 (blue), 350 (green), and 380 nm (red)).

Encouraged by complementary absorption and emission characteristics of NDC and DPTTZ units, we turned our attention to the PL properties of bichromophoric and control MOFs. Steady-state fluorescence studies of a $Zn_2(NDC)_2(DPTTZ)$ suspension in DMF revealed that (**Figure 2.4c**) irrespective of the excitation wavelengths, it only displayed the characteristic emission of DPTTZ at 410 nm and none from NDC struts, suggesting that the latter acted as antenna chromophores. As a result, exclusively DPTTZ-centric MOF emission (410 nm) was observed through both direct (380 nm) and indirect (320 nm) excitation. In contrast, 1,4-BDC and DPTTZ did not share overlapping emission with absorption spectra, which eliminated the possibility of ligand-to-ligand energy transfer in the control MOF (**Figure 2.5a**). Therefore, $Zn_2(1,4\text{-}BDC)_2(DPTTZ)_2$ required direct excitation of DPTTZ ligands to display photoluminescence, which appeared at a slightly longer wavelength (435 nm) compared to that of $Zn_2(NDC)_2(DPTTZ)$ possibly because of π−π-interaction between the closely spaced (<3.6−4 Å apart) parallel DPTTZ ligands (**Figure 2.5b**). Likewise, another control MOF $Zn_2(NDC)_2(BPY)$ devoid of energy accepting DPTTZ pillars only displayed a characteristic NDC emission peak at ∼380 nm. The drop-cast MOF films displayed slightly longer wavelength emissions compared to respective suspensions (**Figure 2.6**).

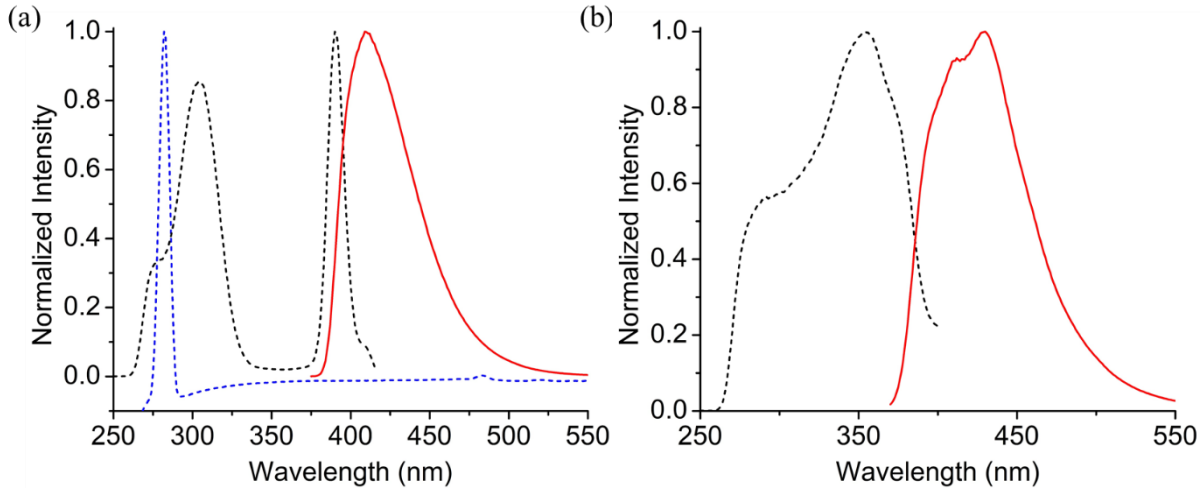


**Figure 2.5:** (a) Excitation (dashed lines) and emission (solid lines) spectra of free BDC (blue) and DPTTZ (red) ligands showing the lack of spectral overlap required for FRET. (b) The excitation (dashed black line) and emission (solid red line) spectra of $Zn_2$(1,4-BDC)$_2$(DPTTZ)$_2$.

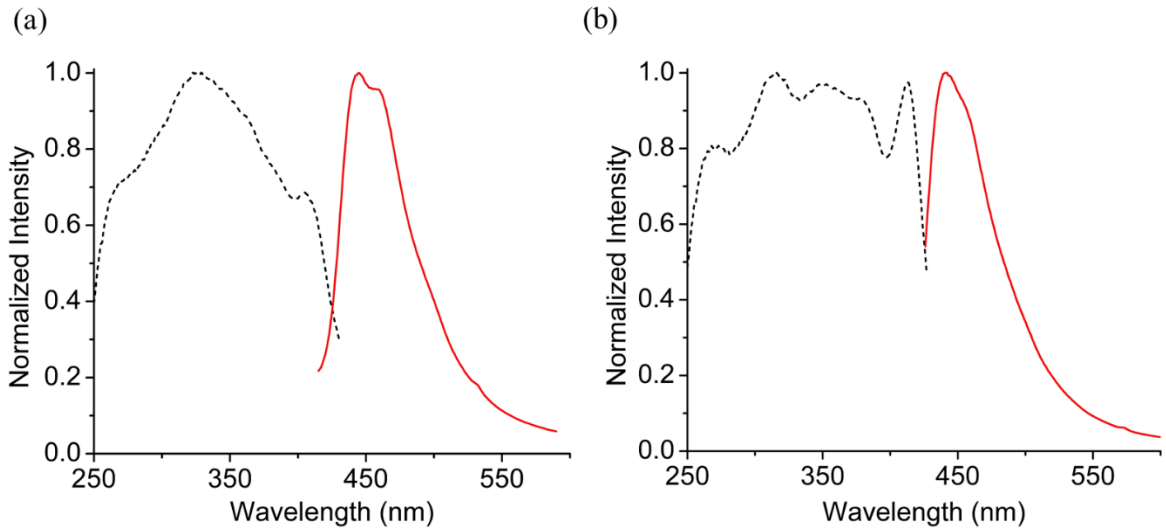


**Figure 2.6:** Excitation (dotted black) and emission (solid red) spectra of drop-cast films of (a) $Zn_2$(NDC)$_2$(DPTTZ). and (b) $Zn_2$(1,4-BDC)$_2$(DPTTZ)$_2$.

The fluorescence quantum yields (ΦF) were obtained from steady-state fluorescence measurements. The TCSPC data (**Figure 2.7**) were fit into double and triple exponential decays to obtain fluorescence lifetimes (τF) and radiative decay rates (kF) (**Table 2.1**).

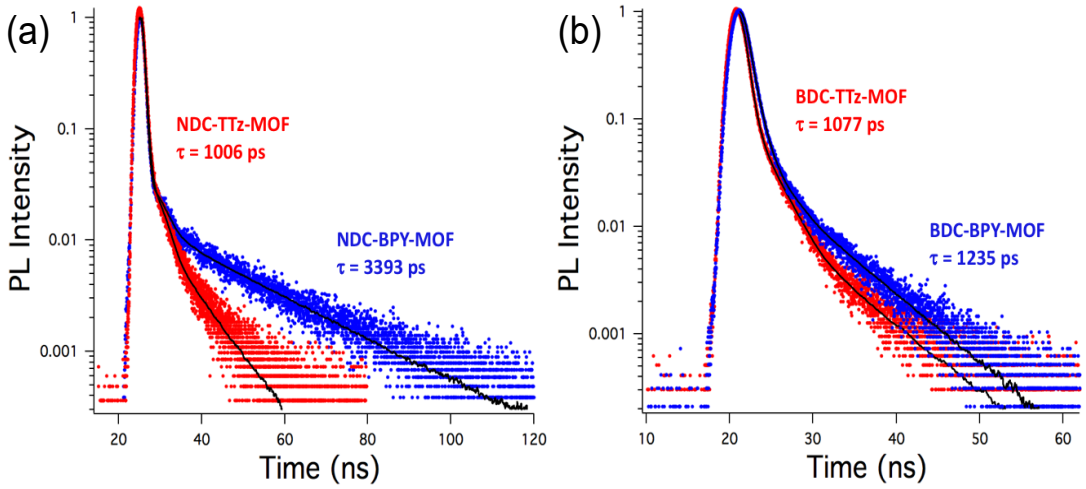


**Figure 2.7:** Comparisons between PL decay profiles of (a) $Zn_2(NDC)_2(DPTTZ)$ (red) and $Zn_2(NDC)_2(BPY)$ (blue) and (b) $Zn_2(1,4\text{-}BDC)_2(DPTTZ)_2$ and $Zn_2(1,4\text{-}BDC)_2(BPY)$ suspensions in chlorobenzene.

In general, the fluorescence lifetimes of MOFs measured in chlorobenzene suspensions were longer than in drop cast films, which could be attributed to exciton−exciton interactions leading to fluorescence quenching in the films. However, thin-film measurements allowed for direct and more accurate comparisons between these MOFs and free fluorescent ligands. The fluorescence lifetime of DPTTZ (τF = 461 ps)

became significantly longer when it was incorporated into MOFs: 953 ps in $Zn_2$(1,4-BDC)$_2$(DPTTZ)$_2$ and 620 ps in $Zn_2$(NDC)$_2$(DPTTZ). The longer fluorescence lifetimes of the MOF-bound preorganized DPTTZ ligands can be attributed to diminished π–π-interaction between them, which could quench the emission of aromatic fluorophores. The differences between fluorescence lifetimes of dilute DPTTZ solution and DPTTZ-based MOF suspensions were less pronounced than in films (**Table 2.1**), as they all experienced longer lifetimes (∼1 ns). Nevertheless, the fluorescence lifetimes of $Zn_2$(NDC)$_2$(DPTTZ) containing complementary energy donor and acceptor ligands was shorter than that of $Zn_2$(1,4-BDC)$_2$(DPTTZ)$_2$ both in suspensions and thin films, suggesting that singlet exciton delocalization was perhaps more effective in the former and singlet energy transfer was less efficient in the latter due to poor emission of BDC and the lack of overlap between BDC and DPTTZ emission and absorption spectra, respectively. The fluorescence quantum yields and radiative rates of DPTTZ increased slightly when it was incorporated into MOFs, which could be attributed to its rigidification and coordination with Lewis acidic Zn(II) centers. The alkylation of pyridyl groups of DPTTZ is also known to enhance its fluorescence.[80]

**Table 2.1:** The fluorescence lifetimes ($\tau_F$), quantum yields ($\Phi_F$), radiative rates ($k_F$) of control and DPTTZ-based MOFs.

| | **$\tau_F$ (ps) suspension** | **$\tau_F$ (ps) drop-cast film** | **$\Phi_F$ suspension** | **$k_F$ ($s^{-1}$) suspension** |
|---|---|---|---|---|
| DPTTZ | 1044 | 461 | 0.22 (380 nm ex.) | $2.11 \times 10^8$ |
| $Zn_2(BDC)_2(DPTTZ)_2$ | 1077 | 953 | 0.27 (407 nm ex.) | $2.50 \times 10^8$ |
| $Zn_2(NDC)_2(DPTTZ)$ | 1006 | 620 | 0.38 (381 nm ex.) | $3.78 \times 10^8$ |
| $Zn_2(NDC)_2(BPY)$ | 3393 | 1368 | — | — |
| $Zn_2(BDC)_2(BPY)_2$ | 1235 | 470 | — | — |

NDC has a fairly long fluorescence lifetime and rich photophysics in the long-UV region,[89,] whereas BPY has very limited excitation and emission dynamics. Therefore, the photophysics of control MOF $Zn_2(NDC)_2(BPY)$ was dominated by NDC struts and showed extended fluorescent lifetimes: 1368 ps in drop-cast films and 3393 ps in suspension (**Figure 2.7a**). In comparison, the PL decay profile (**Figure 2.7a**) of $Zn_2(NDC)_2(DPTTZ)$ framework featuring complimentary energy donor and acceptor units revealed significantly shorter fluorescence lifetimes both in thin-films (620 ps) and suspension (1006 ps), which were more comparable to that of DPTTZ than NDC. The excitation spectrum of this

bichromophoric MOF indicated that NDC and DPTTZ ligands could be sensitized independently; however, its steady-state emission stemmed exclusively from the latter (**Figure 2.4c**) regardless of the excitation wavelength. Furthermore, the relative intensities of the DPTTZ-centric PL of the MOF upon indirect (NDC at 320 nm) and direct (DPTTZ at 380 nm) excitations were comparable. Together, these results indicated that $^{1}$*NDC to DPTTZ singlet energy transfer within this bichromophoric MOF. On the other hand, the PL lifetimes and decay profiles (**Figure 2.7b**) of $Zn_2(1,4\text{-BDC})_2(DPTTZ)_2$ were comparable to that of $Zn_2(1,4\ BDC)_2(BPY)$, indicating that there was no ligand-to-ligand energy transfer in either case, and the photophysics of the former was again dominated by DPTTZ ligands.

Finally, we investigated the PL changes of $Zn_2(NDC)_2(DPTTZ)$ MOF in response to $Hg^{2+}$, a toxic heavy metal ion.[90–92] In the presence of a dilute $Hg(OTf)_2$ solution with concentration as low as 75 μM or 15 ppm, the emission peak of $Zn_2(NDC)_2(DPTTZ)$ suspension (0.1 mg/mL in DMF) (**Figure 2.8**) started to shift to a longer wavelength (450 nm), and its intensity also diminished. These changes could be attributed to the heavy atom effect and possible coordination of $Hg^{2+}$ with the sulfur atoms of DPTTZ ligands. This hypothesis was supported by the fact that in the presence of $Hg^{2+}$, free DPTTZ ligand also displayed similar PL quenching and bathochromic shift, whereas free NDC ligand exhibited only fluorescence quenching but no shift (**Figure 2.9**). Furthermore, despite $Hg^{2+}$-induced red-shift and partial quenching of $Zn_2(NDC)_2(DPTTZ)$ MOF fluorescence, the longest wavelength excitation peak (390 nm) associated with DPTTZ excitation

remained unchanged, verifying that the new emission peak stemmed from DPTTZ–$Hg^{2+}$ interactions.

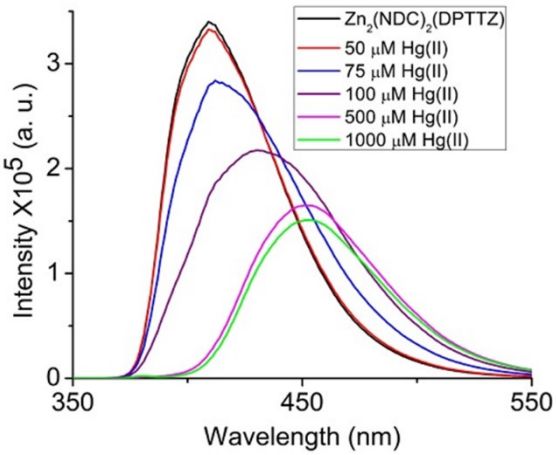


**Figure 2.8:** The PL response of $Zn_2(NDC)_2(DPTTZ)$ suspension (0.1 mg/mL in DMF) to increasing concentration of $Hg(OTf)_2$ (10–1000 μM).

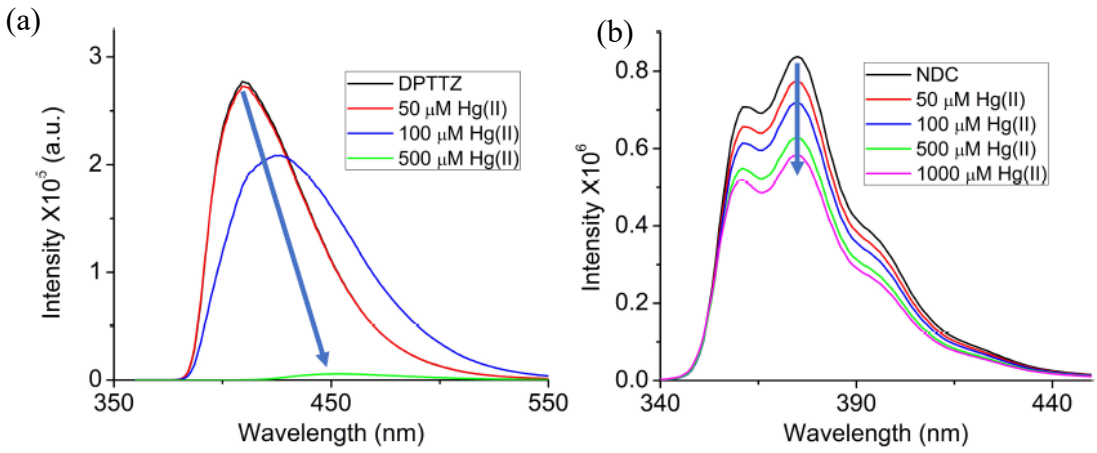


**Figure 2.9:** Fluorescence red-shift and quenching of free DPTTZ (left) and NDC (right) solutions in DMF with increasing concentrations of $Hg^{2+}$.

While both $Zn_2(NDC)_2(DPTTZ)$ MOF and free DPTTZ ligand displayed similar $Hg^{2+}$-induced PL changes, under the same conditions (9.98 $x10^{-5}$ M DPTTZ concentration), the PL quenching of the former was more significant (**Figure 2.10**), demonstrating that the DPTTZ-based MOF was more sensitive to $Hg^{2+}$ than the free ligand. Upon washing the $Hg^{2+}$ treated $Zn_2(NDC)_2(DPTTZ)$ MOF with a copious amount of DMF, the new 450 nm emission peak disappeared, and the original 410 nm peak reemerged (**Figure 2.11**), demonstrating that the interaction of the MOF with $Hg^{2+}$ and the corresponding PL changes were easily reversible. The $Hg^{2+}$- induced red-shift of $Zn_2(NDC)_2(DPTTZ)$ MOF photoluminescence was also visible in the naked eye from the fluorescence microscope images of corresponding drop-cast films. The pristine MOF crystals displayed blue emission, whereas the $Hg^{2+}$-treated MOF appeared teal under the same irradiation (**Figure 2.11**, inset).

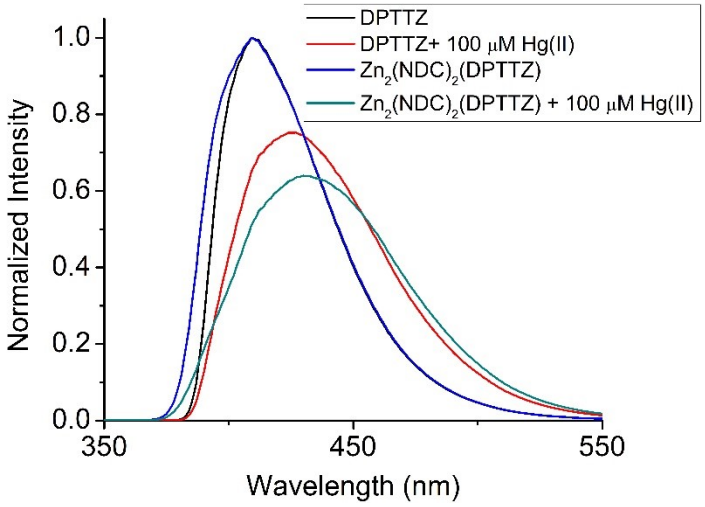


**Figure 2.10:** The PL response of $Zn_2(NDC)_2(DPTTZ)$ MOF and free DPTTZ ligand to 100 μM $Hg^{2+}$.

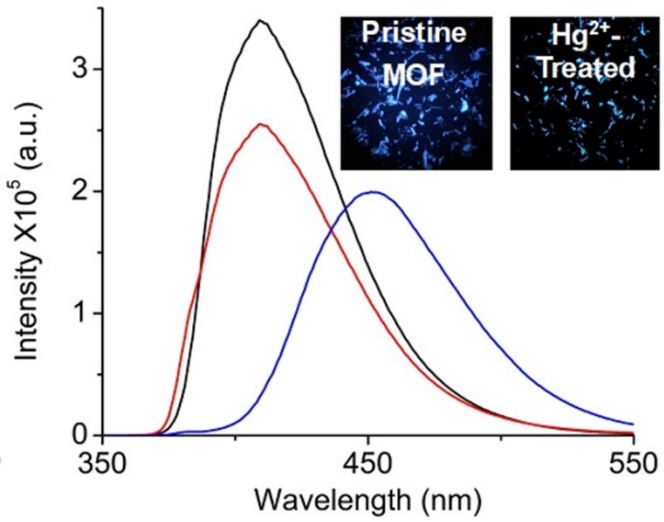


**Figure 2.11:** The PL spectra of pristine (black) and $Hg^{2+}$-treated $Zn_2(NDC)_2(DPTTZ)$ before (blue) and after (red) washing with DMF showing its reversible $Hg^{2+}$ sensing capability. Inset: The fluorescence microscope images of pristine (left) and $Hg^{2+}$-treated (right) $Zn_2(NDC)_2(DPTTZ)$.

Unlike $Hg^{2+}$, however, other transition metal ions, such as $Mn^{2+}$, $Fe^{2+}$, $Co^{2+}$, $Ni^{2+}$, $Cu^{2+}$, and $Cd^{2+}$, did not cause any red-shift of $Zn_2(NDC)_2(DPTTZ)$ photoluminescence, and only $Fe^{2+}$ and $Cu^{2+}$ engendered significant fluorescence quenching (**Figure 2.12a**). The free DPTTZ ligand also displayed a similar PL response to these metal ions (**Figure 2.13**), confirming that this ligand was indeed responsible for the cation-induced PL changes in the MOF. Thus, the $Hg^{2+}$-induced PL response of the MOF was unique, which bodes well for its sensing application. When exposed to a mixture of different metal ions, including $Hg^{2+}$, the MOF still displayed the characteristic $Hg^{2+}$-specific PL signal (**Figure 2.12a**); that is, it was able to detect $Hg^{2+}$ in the presence of other metal ions.

Furthermore, the PXRD profiles of $Zn_2(NDC)_2(DPTTZ)$ after being exposed to $Hg^{2+}$ and other metal ions remained unchanged (**Figure 2.12b**), confirming that the framework retained its structural integrity under these conditions. The strong similarities between the $Hg^{2+}$-induced PL changes of $Zn_2(NDC)_2(DPTTZ)$ MOF and free DPTTZ ligand, coupled with the reversibility of PL changes upon washing the MOF with pure solvents not only confirmed that the $Hg^{2+}$/DPTTZ interaction was responsible for the PL changes but also ruled out a remote possibility of such changes being caused by metal ion exchange in $Zn_2(COO)_4$ paddle wheel nodes, which is a very slow process and unlikely to occur during the course of fairly quick (minutes) fluorescence titration experiment s.[93]

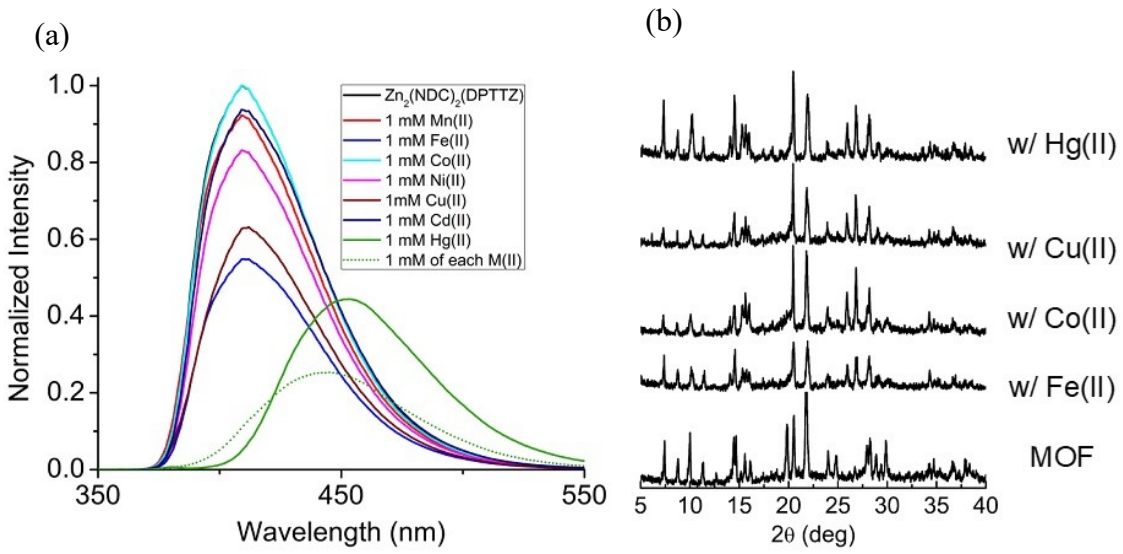


**Figure 2.12:** (a) The PL changes of $Zn_2(NDC)_2(DPTTZ)$ in response to different transition metal ions individually (1 mM, color-coded solid lines) and as a mixture containing $Hg^{2+}$ (1 mM each, dotted green line). (b) The PXRD profiles of $Zn_2(NDC)_2(DPTTZ)$ before and after being exposed to different metal ion solutions (1 mM in DMF) showing the stability of the framework.

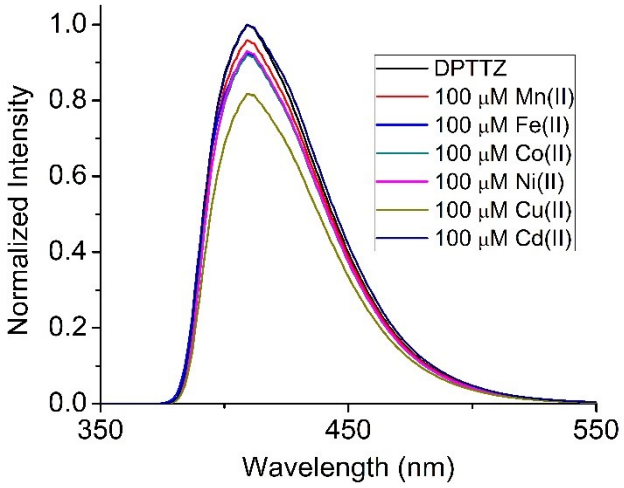


**Figure 2.13:** The PL response of free DPTTZ ligand to different metal ions.

The PL changes of $Zn_2(NDC)_2(DPTTZ)$ MOF occurred at as low as 15 ppm of $Hg^{2+}$ concentration; however, the amount of $Hg^{2+}$ adsorbed by the MOF has not been determined by batch experiments. Nevertheless, the distinct and reversible $Hg^{2+}$-induced PL response rendered $Zn_2(NDC)_2(DPTTZ)$ MOF a promising $Hg^{2+}$ sensor (in the tested organic solvent), although quantification of adsorbed $Hg^{2+}$ remains to be done to fulfill all the necessary criteria of practical luminescent sensors.[40] It is worth noting that, although several MOFs are known to display $Hg^{2+}$-induced fluorescence intensity changes,[32,33] unlike $Zn_2(NDC)_2(DPTTZ)$, they rarely exhibit totally new emission peaks in the presence of $Hg^{2+}$. Therefore, the $Hg^{2+}$- specific fluorescent changes of $Zn_2(NDC)_2(DPTTZ)$, which were distinct from that caused by other transition metal ions, made it more specific to $Hg^{2+}$ and less susceptible to interference from other cations. Furthermore, because of the distinct excitation wavelengths of NDC and DPTTZ ligands and the ligand-to-ligand energy transfer event, $Zn_2(NDC)_2(DPTTZ)$ can be sensitized at a wide wavelength region

(275−400 nm) to access its blue photoluminescence and $Hg^{2+}$ sensing capability, a scope that monochromophoric MOFs lack.

## 2.3.Experimental

### 2.3.1. General materials and methods

Starting materials, including NDC, 1,4-benzenedicarboxylic acid (1,4-BDC), 4,4′-bipyridine (BPY), dithiooxamide, 4-pyridinecarboxaldehyde, $Zn(NO_3)_2 \cdot 6H_2O$, $Hg(OTf)_2$, $Mn(NO_3)_2$, $Fe(ClO_4)_2$, $Co(NO_3)_2$, $Ni(NO_3)_2$, $Cu(NO_3)_2$, $Cd(NO_3)_2$, and solvents (DMF, MeCN, EtOH, $CHCl_3$, chlorobenzene, etc.) were purchased from Sigma Aldrich, Acros Organic, TCI America, and VWR and used as-obtained.

**$^1$H NMR**

The $^1$H NMR spectra were recorded on a Bruker 500 MHz NMR spectrometer.

**Single-crystal X-ray diffraction (SXRD)**

SXRD analyses of MOF crystals were performed on a Bruker D8 Venture dual-source diffractometer with Cu and Mo radiation sources and CMOS detector, and structures were solved and refined using Bruker SHELXTL software package.

**Powder X-ray diffraction (PXRD)**

PXRD analyses were done with a Rigaku Ultima IV X-ray diffractometer equipped with Cu Kα radiation source (λ = 1.5406 Å) and a CCD area detector.

**BET measurement**

The porosity of MOFs was determined from $CO_2$ sorption isotherms recorded on a Quantachrome Autosorb iQ Gas Sorption Analyzer.

**TGA-DSC**

The thermal stability of MOFs was determined from thermogravimetric analysis (TGA) and differential scanning calorimetry (DSC) measured with a TA Instruments SDT Q600.

**UV-vis and steady-state fluorescence spectroscopy**

The UV−vis absorption spectra of ligands and MOFs were recorded on a Shimadzu UV-2600 spectrophotometer equipped with an integrated sphere (200−1400 nm) and steady-state excitation and emission spectra with a Shimadzu RF-6000 equipped with a xenon lamp.

**TCSPC measurements**

Time-correlated single photon counting (TCSPC) measurements were conducted on a Jobin Yvon-Spex Fluorolog equipped with a 389 nm laser diode. The TCSPC fluorescence decay data were fit to double, and triple exponential decays using Igor Pro 6.3 software and in-house developed fitting/graphing scripts.

### 2.3.2. Synthesis and Characterization

**DPTTZ ligand**

DPTTZ ligand was synthesized following a reported protocol.[86] Briefly, a solution mixture of dithiooxamide (200 mg, 1.66 mmol) and 4-pyridinecarboxaldehyde (0.4 mL, 4.4 mmol) in anhydrous DMF (10 mL) was heated under reflux for 2.5 h. Upon cooling of the reaction mixture to room temperature, a yellow crystalline product precipitated out, which was collected by filtration, washed with $H_2O$ and MeOH, and dried under air (311 mg, 63% yield). The 1H NMR spectrum of the product was in good agreement with that of DPTTZ reported in the literature.[86]

**$Zn_2(NDC)_2(DPTTZ)\cdot(DMF)_2$ MOF**

$Zn_2(NDC)_2(DPTTZ)$ MOF was synthesized under standard solvothermal reaction conditions used for pillared paddle wheel architectures.[87,88] First, DPTTZ (6.0 mg, 0.02 mmol) was dissolved in hot DMF (5 mL) and added to a freshly prepared solution of $Zn(NO_3)_2\cdot 6H_2O$ (11.90 mg, 0.04 mmol) and NDC (8.73 mg, 0.04 mmol) in DMF (1.5 mL) in a screw-capped vial. Then the resulting reaction mixture was placed inside an oven and heated at a constant 80 °C for 2 days to obtain pale yellow colored rod-shaped crystals suitable for single-crystal X-ray diffraction (SXRD) analysis. These crystals were washed with fresh DMF and MeOH and dried under a vacuum to obtain the bulk material (7.9 mg, 44% yield).

The SXRD analysis (Appendix A) of as-synthesized crystals revealed a triclinic unit cell and yielded a total of 49321 reflections to a maximum θ of 26.39° (0.80 Å resolution), of which 4257 were independent (average redundancy 11.586, completeness = 99.5%, Rint = 5.87%, Rsig =2.55%) and 3889 (91.36%) were greater than $2\sigma(F^2)$. The final cell constants of a = 8.0961(13) Å, b = 10.5093(15) Å, c = 12.981(2) Å, α = 75.761(5)°, β = 77.486(6)°, γ = 88.858(5)°, and volume = 1044.5(3) $Å^3$ were based on the refinement of the XYZ-centroids of reflections above 20 σ(I). The calculated minimum and maximum transmission coefficients were 0.7910 and 0.9360. The structure was solved and refined using space group $P\bar{1}$, 1with Z = 1 for the formula unit $C_{44}H_{34}N_6O_{10}S_2Zn_2$. The final anisotropic full-matrix least-squares refinement on F2 with 335 variables converged at R1 = 3.50% for the observed data and wR2 = 8.62% for all data. The goodness-of-fit was 1.093. The largest peak in the final difference electron density synthesis was 0.671 e−/$Å^3$, and the largest hole was −0.913 e−/$Å^3$ with an RMS deviation of 0.082 e−/$Å^3$. On the basis of the final model, the calculated density was 1.592 g/$cm^{3,}$ and F(000) was 512e−.

**$Zn_2$(1,4-BDC)$_2$(DPTTZ)$_2$·(DMF) MOF**

A solvothermal reaction of $Zn(NO_3)_2·6H_2O$ (11.90 mg, 0.04 mmol), DPTTZ (6.0 mg, 0.02 mmol), and BDC (6.73 mg, 0.04 mmol) in DMF (6.5 mL) under the same conditions (80 °C, 2 d) yielded needle-shaped pale yellow crystals (6.6 mg, 62% yield) suitable for SXRD analysis.

The SXRD analysis (Appendix B) revealed an orthorhombic unit cell and yielded a total of 23443 reflections to a maximum θ of 22.00° (0.95 Å resolution), of which 6124

were independent (average redundancy 3.828, completeness = 99.5%, Rint = 8.34%, Rsig = 7.07%) and 4833 (78.92%) were greater than $2\sigma(F^2)$. The final cell constants of a = 34.566(2) Å, b = 17.1421(8) Å, c = 17.1901(10) Å, and volume = 10185.7(10) $Å^3$ were based on the refinement of the XYZ-centroids of reflections above 20 σ(I). The calculated minimum and maximum transmission coefficients were 0.8214 and 1.0000. The structure was solved and refined using space group Iba2, with Z = 8 for the formula unit $C_{47}H_{31}N_9O_9S_4Zn_2$.[84,85] The final anisotropic full-matrix least-squares refinement on $F^2$ with 641 variables converged at R1 = 4.40% for the observed data and wR2 = 8.87% for all data. The goodness-of-fit was 1.017. The largest peak in the final difference electron density synthesis was 0.921 e−/$Å^3$, and the largest hole was −0.357 e−/$Å^3$ with an RMS deviation of 0.071e−/Å3. On the basis of the final model, the calculated density was 1.467 g/$cm^3$, and F(000) was 4576 e−.

**Steady-State and Time-Resolved Fluorescence Studies**

For steady-state fluorescence analysis, DMF and chlorobenzene solutions of NDC and DPTTZ ligands and suspensions of $Zn_2(NDC)_2(DPTTZ)$, $Zn_2(BDC)_2(DPTTZ)_2$, and $Zn_2(NDC)_2(BPY)$ MOFs were used.

For time-correlated single-photon counting (TCSPC) measurements, drop-cast films of NDC, BDC, and DPTTZ ligands and MOFs were prepared on Fisherbrand Plain Microscope Slides from corresponding chlorobenzene solutions or suspensions (2 mg/mL, 0.25 mL). The films were allowed to dry in open air for 0.5 h before the measurements.

**Fluorescence Sensing Studies**

For fluorescence titration studies, stock solutions of $Hg(OTf)_2$, $Mn(NO_3)_2$, $Fe(ClO_4)_2$, $Co(NO_3)_2$, $Ni(NO_3)_2$, $Cu(NO_3)_2$, and $Cd(NO_3)_2$ in DMF (6 mM) were added to MOF suspensions (0.1 mg/mL, 2 mL) and spectra were recorded at increasing salt concentrations (10−1000 μM).

## 2.4.Conclusions

In summary, we have constructed a new luminescent pillared paddle-wheel framework $Zn_2(NDC)_2(DPTTZ)$, featuring NDC struts as antenna chromophores and DPTTZ pillars as energy acceptors and light emitters. The overlapping emission and absorption spectra of these two ligands enabled efficient inter-ligand energy transfer leading to exclusively DPTTZ-centric long-wavelength emission regardless of the excitation wavelength. Time-resolved fluorescence measurements revealed a much shorter excited state lifetime of $Zn_2(NDC)_2(DPTTZ)$ than a control MOF $Zn_2(NDC)_2(BPY)$ devoid of the energy acceptor, which was consistent with the faster fluorescence decay of DPTTZ than NDC. Furthermore, $Zn_2(NDC)_2(DPTTZ)$ was able to selectively sense $Hg^{2+}$, a toxic heavy metal ion, at μM concentrations. In the presence of $Hg^{2+}$, the characteristic DPTTZ-centric emission peak of this MOF underwent significant red-shift, while other transition metal ions merely caused modest PL quenching but no shift. The PXRD profile of the $Hg^{2+}$-treated framework remained unchanged and the original PL characteristic could be recovered by DMF washing, demonstrating that it could, in principle, serve as a reusable $Hg^{2+}$ sensor. Although the limited hydrolytic stability of $Zn_2$ pillared paddle-wheel MOFs

could hinder real-life application of $Zn_2(NDC)_2(DPTTZ)$ as a $Hg^{2+}$ sensor, this promising proof-of-concept demonstration inspired us to construct a Zr(IV)-based framework featuring dibenzoate-terminated TTZ ligands, which is expected to be water-stable at a wide pH range[32] and could qualify as a practical $Hg^{2+}$ sensor. Thus, this work presents a new luminescent MOF with ligand-centric emission, efficient ligand-to-ligand energy transfer, and selective $Hg^{2+}$ sensing capabilities, which will likely trigger an upsurge of TTZ-based MOFs for various applications.

## 2.5.References


1. Barber, J.; Andersson, B. Revealing the blueprint of photosynthesis. *Nature* **1994**, *370*, 31−34.
2. Valeur, B.; Berberan-Santos, M. Excitation Energy Transfer. In Molecular Fluorescence: Principles and Applications, 2nd ed.; Wiley-VCH: Weinheim, 2012; pp 213−261.
3. Webber, S. E. Photon-harvesting polymers. *Chem. Rev*. **1990**, *90*, 1469−1482.
4. Aratani, N.; Kim, D.; Osuka, A. Discrete Cyclic Porphyrin Arrays as Artificial Light Harvesting Antenna. *Acc. Chem. Res*. **2009**, *42*, 1922−1934.
5. Li, X.; Sinks, L. E.; Rybtchinski, B.; Wasielewski, M. R. Ultrafast Aggregate-to-Aggregate Energy Transfer within Self-assembled Light-Harvesting Columns of Zinc PhthalocyanineTetrakis-(Perylenediimide). *J. Am. Chem. Soc*. **2004**, *126*, 10810−10811.
6. Patwardhan, S.; Sengupta, S.; Siebbeles, L. D. A.; Wurthner, F.; Grozema, F. C. Efficient Charge Transport in Semisynthetic Zinc Chlorin Dye Assemblies. *J. Am. Chem. Soc*. **2012**, *134*, 16147−16150.
7. Furukawa, H.; Cordova, K. E.; O'Keeffe, M.; Yaghi, O. M. The Chemistry and Applications of Metal-Organic Frameworks. *Science* **2013**, *341*, 1230444.
8. Kreno, L. E.; Leong, K.; Farha, O. K.; Allendorf, M.; Van Duyne, R. P.; Hupp, J. T. Metal−Organic Framework Materials as Chemical Sensors. *Chem. Rev*. **2012**, *112*, 1105−1125.

9. Li, B.; Chrzanowski, M.; Zhang, Y.; Ma, S. Applications of Metal- Organic Frameworks Featuring Multi-Functional Sites. *Coord. Chem. Rev.* **2016**, *307*, 106−129.
10. He, Y.; Zhou, W.; Qian, G.; Chen, B. Methane storage in metal−organic frameworks. *Chem. Soc. Rev*. **2014**, *43*, 5657−5678.
11. Sumida, K.; Rogow, D. L.; Mason, J. A.; McDonald, T. M.; Bloch, E. D.; Herm, Z. R.; Bae, T.-H.; Long, J. R. Carbon Dioxide Capture in Metal−Organic Frameworks. *Chem. Rev*. **2012**, *112,* 724−781.
12. Li, J.-R.; Sculley, J.; Zhou, H.-C. Metal−Organic Frameworks for Separations. *Chem. Rev*. **2012**, *112*, 869−932.
13. Getman, R. B.; Bae, Y.-S.; Wilmer, C. E.; Snurr, R. Q. Review and Analysis of Molecular Simulations of Methane, Hydrogen, and Acetylene Storage in Metal−Organic Frameworks. *Chem. Rev*. **2012**, *112*, 703−723.
14. Huxford, R. C; Della Rocca, J.; Lin, W. Metal−organic frameworks as potential drug carriers. *Curr. Opin. Chem. Biol*. **2010**, *14*, 262−268.
15. Chen, T.-H.; Popov, I.; Kaveevivitchai, W.; Miljanic, O. S. Metal-Organic Frameworks: Rise of the Ligands. *Chem. Mater.* **2014**, *26*, 4322−4325.
16. Almeida Paz, F. A.; Klinowski, J.; Vilela, S. M. F.; Tomé, J. P. C.; Cavaleiro, J. A. S.; Rocha, J. Ligand design for functional metal−organic frameworks. *Chem. Soc. Rev.* **2012**, *41*, 1088−1110.
17. Lu, W.; Wei, Z.; Gu, Z.-Y.; Liu, T.-F.; Park, J.; Park, J.; Tian, J.; Zhang, M.; Zhang, Q.; Gentle, T., III; Bosch, M.; Zhou, H.-C. Tuning structure and function of

metal−organic frameworks via linker design. *Chem. Soc. Rev*. **2014**, *43*, 5561−5593.

18. Gandara, F.; Uribe-Romo, F. J.; Britt, D. K.; Furukawa, H.; Lei, L.; Cheng, R.; Duan, X.; O'Keeffe, M.; Yaghi, O. M. Porous, Conductive Metal-Triazolates and Their Structural Elucidation by the Charge-Flipping Method. *Chem. - Eur. J.* **2012**, *18*, 10595−10601.
19. Ullman, A. M.; Brown, J. W.; Foster, M. E.; Léonard, F.; Leong, K.; Stavila, V.; Allendorf, M. D. Transforming MOFs for Energy Applications Using Guest@MOF Concept. *Inorg. Chem*. **2016**, *55*, 7233−7249.
20. Allendorf, M.; Medishetty, R.; Fischer, R. A. Guest Molecule as a Design Element for Metal-Organic Frameworks. *MRS Bull*. **2016**, *41*, 865−869.
21. Allendorf, M. A.; Foster, M. E.; Léonard, F.; Stavila, V.; Feng, P. L.; Doty, F. P.; Leong, K.; Ma, E. Y.; Johnston, S. R.; Talin, A. A. Guest-Induced Emergent Properties in Metal-Organic Frameworks. *J. Phys. Chem. Lett*. **2015**, *6*, 1182−1195.
22. D'Alessandro, D. M. Exploiting redox activity in metal−organic frameworks: concepts, trends and perspectives. *Chem. Commun*. **2016**, *52*, 8957−8971.
23. Dolgopolova, E. A.; Shustova, N. B. Metal-Organic Frameworks Photophysics: Optoelectronic Devices, Photoswitches, Sensor, and Phtocatalysts. *MRS Bull*. 2016, *41*, 890−896.
24. Zhang, T.; Lin, W. Metal−organic frameworks for artificial photosynthesis and photocatalysis. *Chem. Soc. Rev*. **2014**, *43*, 5982−5993.

25. Fateeva, A.; Chater, P. A.; Ireland, C. P.; Tahir, A. A.; Khimyak, Y. Z.; Wiper, P. V.; Darwent, J. R.; Rosseinsky, M. J. A Water-Stable Porphyrin-Based Metal−Organic Framework Active for Visible-Light Photocatalysis. *Angew. Chem., Int. Ed.* **2012**, *51*, 7440−7444.

26. Stassen, I.; Burtch, N.; Talin, A.; Falcaro, P.; Allendorf, M.; Ameloot, R. An updated roadmap for the integration of metal−organic frameworks with electronic devices and chemical sensors. *Chem. Soc. Rev*. **2017**, *46*, 3185−3241.

27. Hu, Z.; Deibert, B. J.; Li, J. Luminescent metal-organic frameworks for chemical sensing and explosive detection. *Chem. Soc. Rev*. **2014**, *43*, 5815−5840.

28. Nagarkar, S. S.; Joarder, B.; Chaudhari, A. K.; Mukherjee, S.; Ghosh, S. K. Highly Selective Detection of Nitro Explosives by a Luminescent Metal-Organic Framework. *Angew. Chem., Int. Ed*. **2013**, *52*, 2881−2885.

29. Hu, Z.; Lustig, W. P.; Zhang, J.; Zheng, C.; Wang, H.; Teat, S. J.; Gong, Q.; Rudd, N. D.; Li, J. Effective Detection of Mycotoxins by a Highly Luminescent Metal Organic Framework. *J. Am. Chem. Soc.* **2015**, *137*, 16209−16215.

30. Shustova, N. B.; Cozzolino, A. F.; Reineke, S.; Baldo, M.; Dinca, M. Selective Turn-On Ammonia Sensing Enabled by High-Temperature Fluorescence in Metal Organic Frameworks with Open Metal Site. *J. Am. Chem. Soc*. **2013**, *135*, 13326−13329.

31. Shahat, A.; Hassan, H. M.; Azzazy, H. M. Optical Metal-Organic Framework Sensor for Selective Discrimination of Some Toxic Metal Ions in Water. *Anal. Chim. Acta* **2013**, *793*, 90−98.

32. Yee, K.-K.; Reimer, N.; Liu, J.; Cheng, S.-Y.; Yiu, S.-M.; Weber, J.; Stock, N.; Xu, Z. Effective Mercury Sorption by Thiol-Laced Metal-Organic Frameworks: in Strong Acid and the Vapor Phase. *J. Am. Chem. Soc*. **2013**, *135*, 7795−7798.

33. Liu, B.; Huang, Y.; Zhu, X.; Hao, Y.; Ding, Y.; Wei, W.; Wang, Q.; Qu, P.; Xu, M. Smart Lanthanide Coordination Polymer Fluorescence Probe for Mercury(II) Determination. *Anal. Chim. Acta* **2016**, *912*, 139−145.

34. Wu, L.-L.; Wang, Z.; Zhao, S.-N.; Meng, X.; Song, X.-Z.; Feng, J.; Song, S.-Y.; Zhang, H.-J. A Metal-Organic Framework/DNA Hybrid System as a Novel Fluorescent Biosensor for Mercury(II) Ion Detection. *Chem. - Eur. J*. **2016**, *22*, 477−480.

35. Li, L.; Chen, Q.; Niu, Z.; Zhou, X.; Yang, T.; Huang, W. Lanthanide MOFs Assembled from Fluorene-Based Ligand: Selective Sensing of Pb2+ and Fe3+ Ions. *J. Mater. Chem. C* **2016**, *4*, 1900−1905.

36. Wang, H. M.; Yang, Y. Y.; Zeng, C. H.; Chu, T. S.; Zhu, Y. M.; Ng, S. W. A Highly Luminescent Terbium-Organic Framework for Reversible Detection of Mercury Ions in Aqueous Solution. Photochem. *Photobiol. Sci*. **2013**, *12*, 1700−1706.

37. Zhu, Y.-M.; Zeng, C.-H.; Chu, T.-S.; Wang, H.-M.; Yang, Y.-Y.; Tong, Y.-X.; Su, C.-Y.; Wong, W.-T. A Novel Highly Luminescent LnMOF Film: A Convenient Sensor for $Hg^{2+}$ Detecting. *J. Mater. Chem. A* **2013**, *1*, 11312−11319.

38. Xu, H.; Gao, J.; Qian, X.; Wang, J.; He, H.; Cui, Y.; Yang, Y.; Wang, Z.; Qian, G. Metal-Organic Framework Nanosheets for Fast-Response and Highly Sensitive Luminescent Sensing of $Fe^{3+}$. *J. Mater. Chem. A* **2016**, *4*, 10900−10905.

39. Li, Q.; Wang, C.; Tan, H.; Tang, G.; Gao, J.; Chen, C.-H. A turn on fluorescent sensor based on lanthanide coordination polymer nanoparticles for the detection of mercury(II) in biological fluids. *RSC Adv*. **2016**, *6*, 17811−17817.

40. Diamantis, S. A.; Margariti, A.; Pournara, A. D.; Papaefstathiou, G. S.; Manos, M. J.; Lazarides, T. Luminescent metal−organic frameworks as chemical sensors: common pitfalls and proposed best practices. *Inorg. Chem. Front*. **2018**, *5*, 1493−1511.

41. Sun, L.; Campbell, M. G.; Dincă, M. Electrically Conductive Porous Metal−Organic Frameworks. *Angew. Chem., Int. Ed*. **2016**, *55*, 3566−3579.

42. Stavila, V.; Talin, A. A.; Allendorf, M. D. MOF-based electronic and optoelectronic devices. *Chem. Soc. Rev*. **2014**, *43*, 5994−6010.

43. Givaja, G.; Amo-Ochoa, P.; Gomez Garcia, J. G.; Zamora, F. Electrical conductive coordination polymers. *Chem. Soc. Rev*. **2012**, *41*, 115−147.

44. Allendorf, M. D.; Schwartzberg, A.; Stavila, V.; Talin, A. A. A roadmap to implementing metal−organic frameworks in electronic devices: challenges and critical directions. *Chem. - Eur. J*. **2011**, *17*, 11372−11388.

45. Park, S. S.; Hontz, E. R.; Sun, L.; Hendon, C. H.; Walsh, A.; Van Voorhis, T.; Dincă, M. Cation-Dependent Intrinsic Electrical Conductivity in Isostructural Tetrathiafulvalene-Based Microporous Metal−Organic Frameworks. *J. Am. Chem. Soc.* **2015**, *137*, 1774−1777.

46. Sun, L.; Hendon, C. H.; Minier, M. A.; Walsh, A.; Dincă, M. Million-Fold Electrical Conductivity Enhancement in $Fe_2$(DEBDC) versus $Mn_2$(DEBDC) (E = S, O). *J. Am. Chem. Soc*. **2015**, *137*, 6164−6167.

47. Sheberla, D.; Sun, L.; Blood-Forsythe, M. A.; Er, S.; Wade, C. R.; Brozek, C. K.; Aspuru-Guzik, A.; Dincă, M. High Electrical Conductivity in $Ni_3$(2,3,6,7,10,11 hexaiminotriphenylene)$_2$, a Semiconducting Metal-Organic Graphene Analogue. *J. Am. Chem. Soc*. 20**14**, *136*, 8859−8862.

48. Zeng, M.-H.; Wang, Q.-X.; Tan, Y.-X.; Hu, S.; Zhao, H.-X.; Long, L.-S.; Kurmoo, M. Rigid Pillars and Double Walls in a Porous Metal-Organic Framework: Single Crystal to Single-Crystal, Controlled Uptake and Release of Iodine and Electrical Conductivity. *J. Am. Chem. Soc*. **2010**, *132*, 2561−2563.

49. Talin, A. A.; Centrone, A.; Ford, A. C.; Foster, M. E.; Stavila, V.; Haney, P.; Kinney, R. A.; Szalai, V.; El Gabaly, F.; Yoon, H. P.; Léonard, F.; Allendorf, M. D. Tunable Electrical Conductivity in Metal-Organic Framework Thin-Film Devices. *Science* **2014**, *343*, 66−69.

50. Fernandez, C. A.; Martin, P. C.; Schaef, T.; Bowden, M. E.; Thallapally, P. K.; Dang, L.; Xu, W.; Chen, X.; McGrail, B. P. An Electrically Switchable Metal Organic Framework. *Sci. Rep*. **2015**, *4*, 6114.

51. Guo, Z.; Panda, D. K.; Maity, K.; Lindsey, D.; Parker, T. G.; Albrecht-Schmitt, T. E.; Barreda-Esparza, J. L.; Xiong, P.; Zhou, W.; Saha, S. Modulating electrical conductivity of metal−organic framework films with intercalated guest π-systems. *J. Mater. Chem. C* **2016**, *4*, 894−899.

52. Guo, Z.; Panda, D. K.; Gordillo, M. A.; Khatun, A.; Wu, H.; Zhou, W.; Saha, S. Lowering Band Gap of an Electroactive Metal−Organic Framework via Complementary Guest Intercalation. *ACS Appl. Mater. Interfaces* **2017**, *9*, 32413−32417.

53. Ramaswamy, P.; Wong, N. E.; Shimizu, G. K. H. MOFs as Proton Conductors – Challenges and Opportunities. *Chem. Soc. Rev*. **2014**, *43*, 5913−5932.

54. Horike, S.; Umeyama, D.; Kitagawa, S. Ion Conductivity and Transport by Porous Coordination Polymers and Metal-Organic Frameworks. *Acc. Chem. Res*. **2013**, *46*, 2376−2384.

55. Yoon, M.; Suh, K.; Natarajan, S.; Kim, K. Proton Conduction in Metal-Organic Frameworks and Related Modularly Built Porous Solids. *Angew. Chem., Int. Ed.* **2013**, *52*, 2688−2700.

56. Jeong, N. C.; Samanta, B.; Lee, C. Y.; Farha, O. K.; Hupp, J. T. Coordination-Chemistry Control of Proton Conductivity in the Ionic Metal−Organic Framework Material HKUST-1. *J. Am. Chem. Soc*. **2012**, *134*, 51−54.

57. Ameloot, R.; Aubrey, M.; Wiers, B. M.; Gómora-Figueroa, A. P.; Patel, S. N.; Balsara, N. P.; Long, J. R. Ionic Conductivity in the Metal-Organic Framework UiO-66 by Dehydration and Insertion of Lithium tert-Butoxide. *Chem. - Eur. J.* **2013**, *19*, 5533−5536.

58. Cepeda, J.; Pérez-Yáñez, S.; Beobide, G.; Castillo, O.; Goikolea, E.; Aguesse, F.; Garrido, L.; Luque, A.; Wright, P. A. Scandium/Alkaline Metal-Organic

Frameworks: Adsorptive Properties and Ionic Conductivity. *Chem. Mater*. **2016**, *28*, 2519−2528.

59. Fujie, K.; Ikeda, R.; Otsubo, K.; Yamada, T.; Kitagawa, H. Lithium Ion Diffusion in a Metal-Organic Framework Mediated by an Ionic Liquid. *Chem. Mater*. **2015**, *27*, 7355−7361.
60. Park, S. S.; Tulchinsky, Y.; Dincă, M. Single-Ion $Li^+$, $Na^+$, and $Mg^{2+}$ Solid Electrolytes Supported by a Mesoporous Anionic Cu−Azolate Metal−Organic Framework. *J. Am. Chem. Soc*. **2017**, *139*, 13260−13263.
61. Panda, D. K.; Maity, K.; Palukoshka, A.; Ibrahim, F.; Saha, S. $Li^+$ Ion-Conducting Sulfonate-Based Neutral Metal−Organic Framework. *ACS Sustainable Chem. Eng*. **2019**, *7*, 4619−4624.
62. Miner, E. M.; Park, S. S.; Dincă, M. High $Li^+$ and $Mg^{2+}$ Conductivity in a Cu-Azolate Metal−Organic Framework. *J. Am. Chem. Soc*. **2019**, *141*, 4422−4427.
63. Lopez, H. A.; Dhakshinamoorthy, A.; Ferrer, B.; Atienzar, P.; Alvaro, M.; Garcia, H. Photochemical Response of Commercial MOFs: $Al_2(BDC)_3$ and Its Use as Active Material in Photovoltaic Devices. *J. Phys. Chem. C* **2011**, *115*, 22200−22206.
64. Lee, D. Y.; Kim, E.-K.; Shin, C. Y.; Shinde, D. V.; Lee, W.; Shrestha, N. K.; Lee, J. K.; Han, S.-H. Layer-by-Layer Deposition and Photovoltaic Property of Ru-based Metal−Organic Frameworks. *RSC Adv*. **2014**, *4*, 12037−12042.
65. Liu, J.; Zhou, W.; Liu, J.; Howard, I.; Kilibarda, G.; Schlabach, S.; Coupry, D.; Addicoat, M.; Yoneda, S.; Tsutsui, Y.; Sakurai, T.; Seki, S.; Wang, Z.; Lindemann,

P.; Redel, E.; Heine, T.; Wöll, C. Photoinduced Charge-Carrier Generation in Epitaxial MOF Thin Films: High Efficiency as a Result of an Indirect Electronic Band Gap? *Angew. Chem., Int. Ed*. **2015**, *54*, 7441−7445.

66. Liu, J.; Zhou, W.; Liu, J.; Fujimori, Y.; Higashino, T.; Imahori, H.; Jiang, X.; Zhao, J.; Sakurai, T.; Hattori, Y.; Matsuda, W.; Seki, S.; Garlapati, S. K.; Dasgupta, S.; Redel, E.; Sun, L.; Wöll, C. A New Class of Epitaxial Porphyrin Metal−Organic Framework Thin-Films with Extremely High Photocarrier Generation Efficiency: Promising Materials for All Solid-State Solar Cells. *J. Mater. Chem. A* **2016**, *4*, 12739−12747.
67. Maza, W. A.; Haring, A. J.; Ahrenholtz, S. R.; Epley, C. C.; Lin, S. Y.; Morris, A. J. Ruthenium(II)-Polypyridyl Zirconium(IV) Metal−Organic Frameworks As a New Class of Sensitized Solar Cells. *Chem. Sci.* **2016**, *7*, 719−727.
68. Goswami, S.; Ma, L.; Martinson, A. B. F.; Wasielewski, M. R.; Farha, O. K.; Hupp, J. T. Toward Metal−Organic Framework-Based Solar Cells: Enhancing Directional Exciton Transport by Collapsing Three-Dimensional Film Structures. *ACS Appl. Mater. Interfaces* **2016**, *8*, 30863−30870.
69. Spoerke, E. D.; Small, L. J.; Foster, M. E.; Wheeler, J.; Ullman, A. M.; Stavila, V.; Rodriguez, M.; Allendorf, M. D. MOF-Sensitized Solar Cells Enabled by a Pillared Porphyrin. *J. Phys. Chem. C* **2017**, *121*, 4816−4824.
70. Gordillo, M. A.; Panda, D. K.; Saha, S. Efficient MOFSensitized Solar Cells Featuring Solvothermally Grown [100]-Oriented Pillared Porphyrin Framework-11 Films on ZnO/FTO Surfaces. *ACS Appl. Mater. Interfaces* **2019**, *11*, 3196−3206.

71. Cui, Y.; Yue, Y.; Qian, G.; Chen, B. Luminescent functional metal−organic frameworks. *Chem. Rev*. **2012**, *112*, 1126−1162.

72. Lee, C. Y.; Farha, O. K.; Hong, B. J.; Sarjeant, A. A.; Nguyen, S. T.; Hupp, J. T. Light-Harvesting Metal-Organic Frameworks (MOFs): Efficient Strut-to-Strut Energy Transfer in Bodipy and Porphyrin-Based MOFs. *J. Am. Chem. Soc*. **2011**, *133*, 15858−15861.

73. Son, H.-J.; Jin, S.; Patwardhan, S.; Wezenberg, S. J.; Jeong, N. C.; So, M.; Wilmer, C. E.; Sarjeant, A. A.; Schatz, G. C.; Snurr, R. Q.; Farha, O. K.; Wiederrecht, G. P.; Hupp, J. T. Light-Harvesting and Ultrafast Energy Migration in Porphyrin-Based Metal-Organic Frameworks. *J. Am. Chem. Soc.* **2013**, *135,* 862−869.

74. Dolgopolova, E. A.; Rice, A. M.; Martin, C. R.; Shustova, N. B. Photochemistry and photophysics of MOFs: steps towards MOFbased sensing enhancements. *Chem. Soc. Rev*. **2018**, *47*, 4710−4728.

75. So, M. C.; Wiederrecht, G. P.; Mondloch, J. E.; Hupp, J. T.; Farha, O. K. Metal-organic framework materials for light-harvesting and energy transfer. *Chem. Commun*. **2015**, *51*, 3501−3510.

76. Williams, D. E.; Shustova, N. B. Metal-Organic Frameworks as a Versatile Tool to Study and Model Energy Transfer Processes. *Chem.-Eur. J*. **2015**, *21*, 15474−15479.

77. Williams, D. E.; Rietman, J. A.; Maier, J. M.; Tan, R.; Greytak, A. B.; Smith, M. D.; Krause, J. A.; Shustova, N. B. Energy Transfer on Demand: Photoswitch-

Directed Behavior of Metal-Porphyrin Frameworks. *J. Am. Chem. Soc*. **2014**, *136*, 11886−11889.

78. Dolgopolova, E. A.; Williams, D. E.; Greytak, A. B.; Rice, A. M.; Smith, M. D.; Krause, J. A.; Shustova, N. B. A Bio-inspired Approach for Chromophore Communication: Ligand-to-Ligand and Host-to-Guest Energy Transfer in Hybrid Crystalline Scaffolds. *Angew. Chem., Int. Ed*. **2015**, *54*, 13639−13643.
79. Zhang, Q.; Zhang, C.; Cao, L.; Wang, Z.; An, B.; Lin, Z.; Huang, R.; Zhang, Z.; Wang, C.; Lin, W. Förster Energy Transport in Metal−Organic Frameworks is beyond Step-by-Step Hopping. *J. Am. Chem. Soc*. **2016**, *138*, 5308−5315.
80. Maza, W. A.; Padilla, R.; Morris, A. J. Concentration Dependent Dimensionality of Resonance Energy Transfer in a Postsynthetically Doped Morphologically Homologous Analogue ofUiO-67 MOF with Ruthenium (II) Polypyridyl Complex. *J. Am. Chem. Soc*. **2015**, *137*, 8161−8168.
81. Woodward, A. N.; Kolesar, J. M.; Hall, S. R.; Saleh, N.-A.; Jones, D. S.; Walter, M. G. ThiazolothiazoleFluorophores Exhibiting Strong Fluorescence andViologen-Like Reversible Electrochromism. *J. Am. Chem. Soc*. **2017**, *139*, 8467−8473.
82. Roy, I.; Bobbala, S.; Zhou, J.; Nguyen, M. T.; Nalluri, S. K. M.; Wu, Y.; Ferris, D. P.; Scott, E. A.; Wasielewski, M. R.; Stoddart, J. F. ExTzBox: A Glowing Cyclophane for Live-Cell Imaging. *J. Am. Chem. Soc.* **2018**, *140*, 7206−7212.
83. Rizzuto, F. J.; Faust, T. B.; Chan, B.; Hua, C.; D'Alessandro, D. M.; Kepert, C. J. Experimental and Computational Studies of a Multi-Electron Donor-Acceptor

Ligand Containing the Thiazolo[5,4-d]thiazole Core and its Incorporation into a Metal−Organic Framework. *Chem. - Eur. J*. **2014**, *20*, 17597−17605.

84. Millan, S.; Makhloufi, G.; Janiak, C. Incorporating the Thiazolo[5,4-d]thiazole Unit into a Corrdination Polymer with Interdigitated Structure. *Crystals* **2018**, *8*, 30.

85. Zhai, Z.-W.; Yang, S.-H.; Cao, M.; Li, L.-K.; Du, C.-X.; Zang, S.-Q. Rational Design of Three Two-Fold Interpenetrated Metal- Organic Frameworks: Luminescent Zn/Cd-Metal-Organic Frameworks for Detection of 2,4,6-Trinitrophenol and Nitrofurazone in the Aqueous Phase. *Cryst. Growth Des*. **2018**, *18*, 7173−7182.

86. Hisamatsu, S.; Masu, H.; Azumaya, I.; Takahashi, M.; Kishikawa, K.; Kohmoto, S. U-Shaped Aromatic Ureadicarboxylic Acids as Versatile Building Blocks: Construction of Ladder and Zigzag Networks and Channels. *Cryst. Growth Des*. **2011**, *11*, 5387−5395.

87. Ma, B.-Q.; Mulfort, K. L.; Hupp, J. T. Microporous pillared paddle-wheel based on mixed-ligand coordination of zinc ions. *Inorg. Chem*. **2005**, *44*, 4912−4914.

88. Chun, H.; Dybtsev, D. N.; Kim, H.; Kim, K. Synthesis, X-ray Crystal Structures, and Gas Sorption Properties of Pillared Square Grid Nets Based on Paddle-Wheel Motifs: Implications for Hydrogen Storage in Porous Materials. *Chem. - Eur. J.* **2005**, *11*, 3521−3529.

89. Berlman, I. B.; Weinreb, A. On the fluorescence spectrum and decay time of naphthalene. *Mol. Phys*. **1962**, *5*, 313−319.

90. Sun, Q.; Aguila, B.; Perman, J.; Earl, L.; Abney, C.; Cheng, Y.; Wei, H.; Nguyen, N.; Wojtas, L.; Ma, S. Post-synthetically Modified Covalent Organic Frameworks for Efficient and Effective Mercury Removal. *J. Am. Chem. Soc*. **2017**, *139*, 2786−2793.

91. Aguila, B.; Sun, Q.; Perman, J. A.; Earl, L. D.; Abney, C. W.; Elzein, R.; Schlaf, R.; Ma, S. Efficient Mercury Capture Using Functionalized Porous Organic Polymer. *Adv. Mater*. **2017**, *29*, 1700665.

92. Li, B.; Zhang, Y.; Ma, D.; Shi, Z.; Ma, S. Mercury Nano-Trap for Effective and Efficient Removal of Mercury(II) from Aqueous Solution. *Nat. Commun*. **2014**, *5*, 5537.

93. Lalonde, M.; Bury, W.; Karagiaridi, O.; Brown, Z.; Hupp, J. T.; Farha, O. M. Transmetalation: routes to metal exchange within metal−organic frameworks. *J. Mater. Chem. A* **2013***, 1*, 5453−5468.

# CHAPTER THREE

# GUEST-PROMOTED BANDGAP TUNING OF AN ELECTROACTIVE METAL-ORGANIC FRAMEWORK



## 3.1.Introduction

Narrow bandgap semiconductors with tunable electrical conductivity have been widely used in electronic devices worldwide. The electronics industries are currently ruled by crystalline inorganic semiconductors and conjugated organic polymer. Metal-organic frameworks (MOFs), owing to the excellent tunability in their structural and electronic properties, can be a potential narrow-band semiconductor if the requirements are fulfilled. MOFs[1] possess highly ordered extended structures containing metal ions and organic ligands and can be predesigned for the long-range charge movement. However, the metal cluster nodes that connect the organic linkers to the extended framework in the MOF limit the charge transport (through-bond and through-space) within the framework. The reason behind this poor transport and charge carrier density is due to the nature of most metal clusters (metal-carboxylate bond) and large spatial separation between the linkers.[2,3] Therefore, MOFs exhibiting narrow bandgap are not very common.[3-8] However, MOFs constructed from redox-active organic ligands and mixed-valence metal ions showing high charge mobility, carrier density, and conductivity have been reported.[6, 9-12]

Although a reasonable choice of metal ions and organic linkers can lead to higher intrinsic conductivity, a slight (sub-Å) increase in the inter-ligand distance can cause drastic changes in the conductivity.[11] Therefore, post-synthetic tuning of electronic property by redox-active guest incorporation in the porous MOF has drawn greater interest from researchers. In this regard, Saha and co-workers[13] reported conductivity enhancement of an electroactive MOF by complementary guest π-systems, which facilitated the long-range charge transport in the framework.

This chapter describes the utilization of the guest-promoted, as mentioned earlier, electronic property tuning strategy to reduce the bandgap of an electroactive MOF-74 analog. The MOF-74 was constructed from NDI-based ligand DSNDI and zinc metal ions. This study used an electron-deficient NDI-based ligand since NDI units can form donor/acceptor charge transfer (CT) complexes with other electron-rich π-systems and facilitate charge delocalization.[14-17]

### 3.2.Results and discussions

For this study, the DSNDI ligand was synthesized from the NDA (naphthalene dianhydride) and 4-aminosalicylic acid under reflux conditions.[18] The MOF-74 was then made from the DSNDI ligand and $Zn^{2+}$ via a solvothermal reaction (**Figure 3.1**).

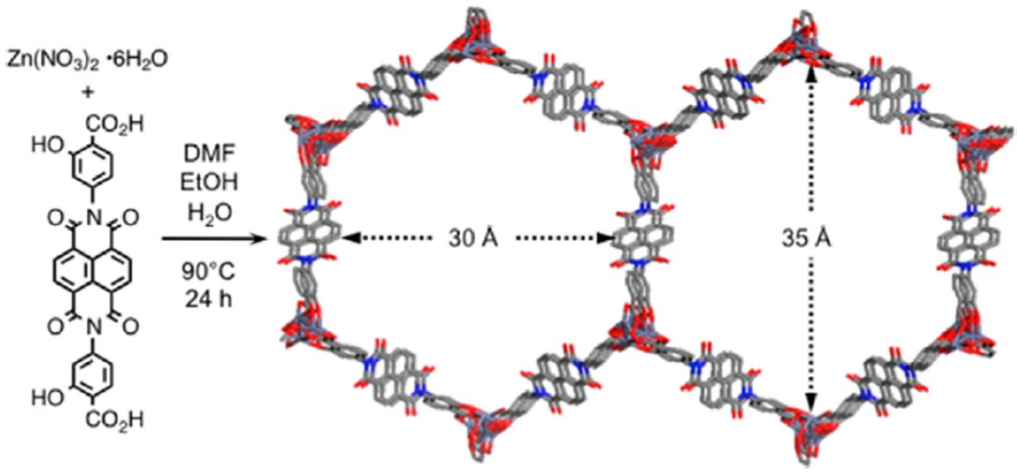


**Figure 3.1**: Synthetic route and structure of MOF-74.

To confirm the structural integrity of the as-synthesized MOF-74, the powder x-ray diffraction (PXRD) pattern was recorded. The PXRD of the as-synthesized MOF-74 matched with the PXRD pattern of traditional MOF-74 topology[19] and calculated[20] pattern for DSNDI-based MOF-74 analog (**Figure 3.2**). Additionally, the TTF-doped MOF-74 showed the same PXRD pattern (**Figure 3.2**) as pristine MOF-74 confirms the structural retention of the MOF-74 upon TTF encapsulation.

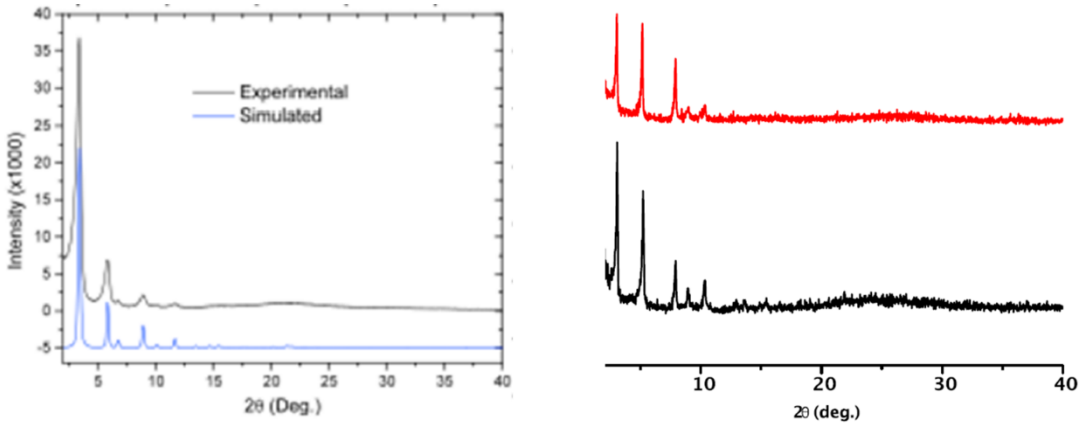


**Figure 3.2:** PXRD of MOF-74-(Left) simulated and experimental. (Right) undoped (black) and TTF-doped (blue).

Furthermore, the thermal stability of the pristine and TTF-doped MOF-74 was determined by thermogravimetric analysis (TGA). The TGA-DSC analysis revealed that the pristine MOF-74 and TTF-doped MOF-74 are stable up to 380 °C and 420 °C, respectively. Phase transition happened in the case of both samples beyond these temperatures (**Figure 3.3**).

The presence of TTF guests in the doped MOF-74 was further confirmed by the energy-dispersive x-ray spectroscopy (EDX) (**Figure 3.4**) and elemental analysis (**Table 3.1**). Both studies revealed the presence of sulfur (characteristics of TTF) in the TTF-doped MOF-74, whereas sulfur is absent in the pristine MOF-74. These results demonstrated the successful incorporation of TTF guests in the MOF-74.

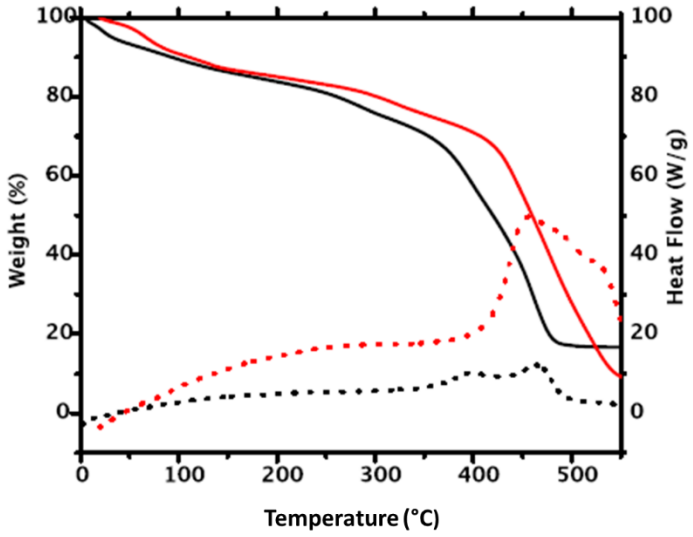


**Figure 3.3:** The TGA (solid lines) and DSC (dotted lines) profiles of DSNDI-based pristine MOF-74 (black) and TTF-doped MOF-74 (red).

**Table 3.1:** Elemental analysis of pristine MOF-74 and TTF-doped MOF-74.

| **Elements** | **Pristine MOF-74** $Zn_2(C_{28}H_{10}N_2O_{10})(H_2O)_5(C_3H_7NO)_{1.5}$ | | **TTF-doped MOF-74** $Zn_2(C_{28}H_{10}N_2O_{10})(H_2O)_5 .(C_6H_4S_4)_{0.2}$ | |
|---|---|---|---|---|
| | Calculated | Found | Calculated | Found |
| C | 45.13 | 44.72 | 44.06 | 43.29 |
| H | 3.55 | 3.40 | 2.63 | 2.82 |
| N | 5.67 | 6.00 | 3.52 | 3.69 |
| S | — | — | 3.22 | 3.40 |

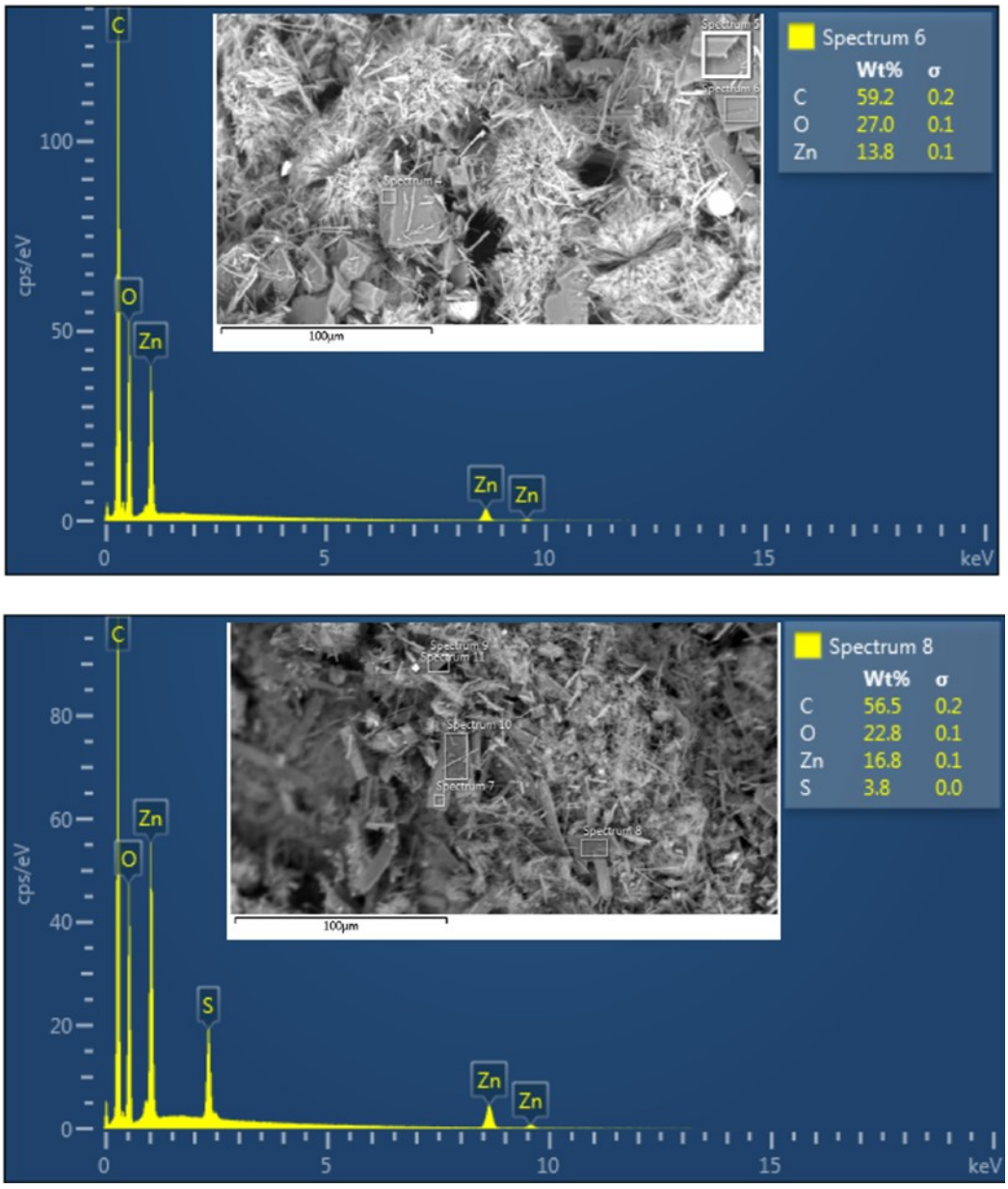


**Figure 3.4:** SEM-EDX data of pristine MOF-74 (top) and TTF-doped MOF-74 (bottom).

Diffused reflectance spectra (DRS) studies were performed to understand the electronic property change upon TTF encapsulation in the MOF-74. For this study, DRS of DSNDI ligand, TTF, MOF-74, and TTF-doped MOF-74 were recorded (**Figure 3.4**). The optical bandgap of the pristine and TTF-doped MOF-74 was calculated from the DRS spectra. The MOF-74 displayed DSNDI ligand-based UV-vis absorption with a $\lambda_{max}$ = 410 nm. The bandgap of pristine MOF-74 (~2.1 eV) was calculated from the onset of this signal at 600 nm. On the other hand, the TTF-doped MOF-74 showed a new CT band centered at 900 nm. The optical bandgap of the TTF-doped MOF was calculated (~1 eV) from the onset point of this new CT band (1250 nm). Such a dramatic drop in optical band gap was attributed to the intercalation of electron-rich TTF guests between electron-deficient DSNDI ligands leading to the formation of π- donor/acceptor stacks. This reduction of the optical band gap is attributed to the π-donor/acceptor interaction between the DSNDI linkers in the MOF-74 and intercalated TTF guests.

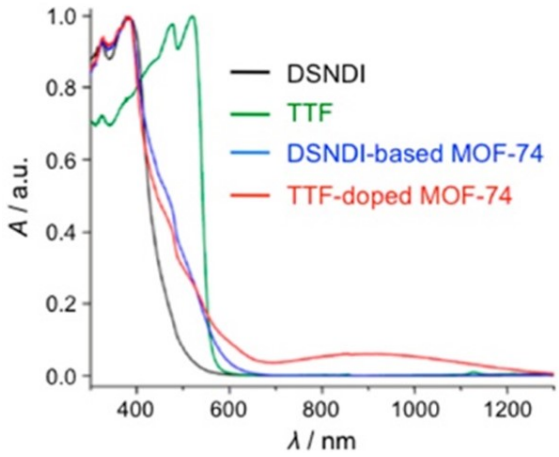


**Figure 3.5:** UV−vis−NIR spectra of DSNDI ligand (black), TTF guest (green), DSNDI-based MOF-74 (blue), and TTF-doped DSNDI-based MOF-74 (red).

## 3.3.Experimental

### 3.3.1. General materials and methods

All chemicals, including $Zn(NO_3)_2.6H_2O$, 1,4,5,8-naphthalenetetracarboxylic dianhydride (NDA), 4-aminosalicylic acid, and solvents (DMF, EtOH, MeOH, DMSO-*d*6), were purchased from Sigma-Aldrich, Acros Organic, TCI America, and Cambridge Isotope Laboratory, and used as obtained.

**$^1$H NMR**

The $^1$H spectrum was recorded on a Bruker 400 MHz NMR spectrometer.

**Powder x-ray diffraction (PXRD)**

PXRD analyses of MOF-74 and TTF-doped MOF-74 were performed in a Rigaku Ultima IV X-ray diffractometer equipped with a Cu Kα radiation source (λ = 1.5406 Å) and a CCD area detector.

**Diffuse reflectance spectroscopy (DRS)**

The UV/Vis/NIR spectra of the ligand, MOF-74, TTF, and TTF-doped MOF-74 were recorded with Shimadzu UV-2600 spectrophotometers equipped with integrated spheres for diffuse reflectance measurements (200–1400 nm range). The optical band gaps of the materials were calculated from the onset of their longest wavelength absorption bands using the following equation: $E_g = 1240 / \lambda$ eV.[21,22]

**TGA-DSC**

Thermogravimetric analysis (TGA) and differential scanning calorimetric (DSC) analysis were conducted under a $N_2$ atmosphere using a TA Instrument SDT Q600 instrument.

**SEM-EDX**

Scanning electron microscopy (SEM) and energy-dispersive X-ray spectroscopy (EDX) of the samples are performed on a Hitachi Variable Pressure SEM S3400 instrument.

**Elemental analysis**

Elemental (CHNS) analyses of pristine MOF-74 and TTF-doped MOF-74 were recorded conducted by Atlantic Microlab Inc.

### 3.3.2. Synthesis

**DSNDI ligand**

DSNDI ligand was synthesized by refluxing NDA (2.68 g, 10 mmol), 4-aminosalicylic acid (4.6 g, 30 mmol), and $Me_3SiCl$ (6.4 mL, 50 mmol) in DMF (12 mL) for 14 h.[23] After allowing the mixture to cool to room temperature, the solid precipitate was filtered and washed first with EtOAc, then with an aqueous NaOH solution (1 M), and finally with $H_2O$ and MeOH to obtain a yellow solid (0.27 g, yield = 5 %). $^1$H NMR (400 MHz, DMSO-*d*6, 25 °C): δ = 8.72 (s, 4H), δ = 7.88–7.86 (d, 2H), δ = 6.94 (s, 2H), δ = 6.85–6.83.06 (m, 2H) ppm. MALDI-TOF-MS: *m*/*z*: $[M]^-_{observed}$ = 537.59, $[M]^-_{calcd}$ = 538.42.

**DSNDI-based MOF-74**

$Zn(NO_3)_2 \cdot 6H_2O$ (21 mg, 0.07 mmol) and DSNDI ligand (17 mg, 0.03 mmol) in a DMF/EtOH/$H_2O$ (3: 0.5: 0.5 mL) solvent mixture was sonicated, and then the reaction mixture was heated at constant 90 °C for 24 h. Within an hour, the reaction mixture became transparent as all the precursors dissolved completely, and after overnight heating, the bright yellow-colored microcrystalline powder was formed. After allowing the reaction mixture to cool down gradually to room temperature, and washed with fresh DMF and MeOH.

**TTF-doped MOF-74**

The activated MOF-74 (15 mg) was immersed in a TTF / MeOH solution (20 mM, 3 mL) and kept in the dark for 2 days. After decanting the solvent, the solid was washed with MeOH to remove excess TTF molecules that were not entrapped inside the MOF and dried under vacuum for 16 h.

**3.4.Conclusions**

In summary, an electroactive MOF-74 was constructed by connecting the electron-deficient ligand (DSNDI) with the $Zn^{2+}$ ion in the extended framework featuring a hexagonal channel. Further, the bandgap of this MOF-74 was suppressed by 1 eV upon encapsulating complementary electron-rich TTF guests in the MOF-74. This study demonstrated the utilization of π-donor/acceptor interactions between the guest and MOF

to tune the electronic property of the latter, which can be advantageous to develop light-harvesting, and semiconducting MOFs.

For the computational study to calculate electronic bandgap, we collaborated with Wei Zhou, and the detail of the computational and electrochemical studies can be found in *ACS Appl. Mater. Interfaces* **2017**, *9*, 32413−32417

### 3.5.References


1. Furukawa, H.; Cordova, K. E.; O'Keeffe, M.; Yaghi, O. M. The Chemistry and Applications of Metal-Organic Frameworks. *Science* **2013**, *341*, 1230444.
2. Xie, L. S.; Skorupskii, G.; Dincă, M. Electrically Conductive Metal−Organic Frameworks. *Chem. Rev*. **2020**, *120*, 8536−8580.
3. Sun, L.; Campbell, M. G.; Dincă, M. Electrically Conductive Porous Metal–Organic Frameworks. *Angew. Chem. Int. Ed*. **2016**, *55*, 3566 – 3579.
4. D'Alessandro, D. M. Exploiting Redox Activity in Metal−Organic Frameworks: Concepts, Trends and Perspectives. *Chem. Commun*. **2016**, *52*, 8957−8971.
5. Stavila, V.; Talin, A. A.; Allendorf, M. D. MOF-Based Electronic and Optoelectronic Devices. *Chem. Soc. Rev*. **2014**, *43*, 5994−6010.
6. Hendon, C. H.; Tiana, A.; Walsh, A. Conductive Metal−Organic Frameworks and Networks: Fact or Fantasy? *Phys. Chem. Chem. Phys*. **2012**, *14*, 13120−13132.
7. Usman, M.; Mendiratta, S.; Lu, K.-L. Semiconductor Metal−Organic Frameworks: Future Low-Bandgap Materials. *Adv. Mater*. **2017**, *29*, 1605071.

*8.* Usman, M.; Mendiratta, S.; Batjargal, S.; Haider, G.; Hayashi, M.; Gade, N. R.; Chen, J.-W.; Chen, Y.-F.; Lu, K.-L. Semiconductor Behavior of a Three-Dimensional Strontium-Based Metal−Organic Frameworks. *ACS Appl. Mater. Interfaces* **2015**, *7*, 22767−22774.

9. Sheberla, D.; Sun, L.; Blood-Forsythe, M. A.; Er, S.; Wade, C. R.; Brozek, C. K.; Aspuru-Guzik, A.; Dincă, M. High Electrical Conductivity in $Ni_3$(2,3,6,7,10,11 hexaiminotriphenylene)$_2$, a Semiconducting Metal−Organic Graphene Analogue. *J. Am. Chem. Soc*. **2014**, *136*, 8859−8862.

10. Kambe, T.; Sakamoto, R.; Kusamoto, T.; Pal, T.; Fukui, N.; Hoshiko, K.; Shimojima, T.; Wang, Z.; Hirahara, T.; Ishizaka, K.; Hasegawa, S.; Liu, F.; Nishihara, H. Redox Control and High Conductivity of Nickel Bis(dithiolene) Complex π-Nanosheet: A Potential Organic Two-Dimensional Topological Insulator. *J. Am. Chem. Soc*. **2014**, *136*, 14357−14360.

11. Park, S. S.; Hontz, E. R.; Sun, L.; Hendon, C. H.; Walsh, A.; Van Voorhis, T.; Dincă, M. Cation-Dependent Intrinsic Electrical Conductivity in Isostructural Tetrathiafulvalene-Based Microporous Metal−Organic Frameworks. *J. Am. Chem. Soc.* **2015**, *137*, 1774−1777.

12. Chen, D.; Xing, H.; Su, Z.; Wang, C. Electrical Conductivity and Electroluminescence of a New Anthracene-Based Metal−Organic Framework with π-Conjugated Zigzag Chains. *Chem. Commun*. **2016**, *52*, 2019−2022.

13. Guo, Z.; Panda, D. K.; Maity, K.; Lindsey, D.; Parker, T. G.; Albrecht-Schmitt, T. E.; Barreda-Esparza, J. L.; Xiong, P.; Zhou, W.; Saha, S. Modulating Electrical

Conductivity of Metal−Organic Framework Films with Intercalated Guest π-Systems. *J. Mater. Chem. C* **2016**, *4*, 894−899.

14. Zych, A. J.; Iverson, B. L. Synthesis and Conformational Characterization of Tethered Self-Complexing 1,5-Dialkoxynaphthalene/1,4,5,8-Napthalenetetracarboxylic Diimide Systems. *J. Am. Chem. Soc*. **2000**, *122*, 8898−8909.
15. Iijima, T.; Vignon, S. A.; Tseng, H.-R.; Jarrosson, T.; Sanders, J. K. M.; Marchioni, F.; Venturi, M.; Apostoli, E.; Balzani, V.; Stoddart, J. F. Controllable Donor-Acceptor Neutral [2]Rotaxanes. *Chem.- Eur. J*. **2004**, *10*, 6375−6392.
16. Ulrich, S.; Lehn, J.-M. Adaptation and Optical Signal Generation in a Constitutional Dynamic Network. *Chem.- Eur. J*. **2009**, *15*, 5640−5645.
17. Fujii, S.; Tada, T.; Komoto, Y.; Osuga, T.; Murase, T.; Fujita, M.; Kiguchi, M. Rectifying Electron-Transport Properties through stacks of Aromatic Molecules Inserted into a Self Assembled Cage. *J. Am. Chem. Soc*. **2015**, *137*, 5939−5947.
18. Guha, S.; Goodson, F. S.; Corson, L. J.; Saha, S. Boundaries of Anion/Naphthalenediimide Interactions: From Anion−π Interactions to Anion-Induced Charge-Transfer and Electron Transfer Phenomena. *J. Am. Chem. Soc.* **2012**, *134*, 13679−13691.
19. Deng, H.; Grunder, S.; Cordova, K. E.; Valente, C.; Furukawa, H.; Hmadeh, M.; Gándara, F.; Whalley, A. C.; Liu, Z.; Asahina, S.; Kazumori, H.; O'Keefe, M.; Terasaki, O.; Stoddart, J. F.; Yaghi, O. M. Large-Pore Apertures in a Series of Metal-Organic Frameworks. *Science* **2012**, *336*, 1018−1023.

20. Guo, Z.; Panda, D. K.; Gordillo, M. A.; Khatun, A.; Wu, H.; Zhou, W.; Saha, S. Lowering Band Gap of an Electroactive Metal−Organic Framework via Complementary Guest Intercalation. *ACS Appl. Mater. Interfaces* **2017**, *9*, 32413−32417.
21. Murphy, A. B. Band-gap Determination from Diffuse Reflectance Measurement of Semiconductor Films, and Application of Photoelectrochemical Water-Splitting. *Solar Energy Mater. Solar Cells* **2007**, *91*, 1326–1337.
22. Musho, T.; Li, J.; Wu, N. Band Gap Modulation of Functionalized Metal–Organic Frameworks. *Phys. Chem. Chem. Phys.* **2014**, *16*, 23646–23653.
23. Sugimori, G.; Ohtsuka, T.; Masui, M. Anti-helicobacterial agents: EP, EP1340755[P]. 2003.

# CHAPTER FOUR

# IMPROVEMENT OF ELECTRICAL CONDUCTIVITY OF A MICROPOROUS MOF BY IN-SITU POLYMERIZATION OF CONDUCTING POLYMERS IN THE MOF PORES

## 4.1.Introduction

To date, many impressive properties of metal–organic frameworks (MOFs), including high surface area[1-3] and porosity,[1,4,5] thermal stability,[6,7] chemical and structural tunability,[1,8,9] have been widely exploited for gas storage and separation,[5,10-14] catalysis,[15,16] and sensing.[17-21] However, electrically conducting MOFs are still relatively less explored[22-25] despite their potential in the field of electrocatalysis,[25-29] energy storage,[30,31,] and chemiresistive sensing.[32-35] Most of the reported MOFs are poor electrical conductors as they were made up of metal-based SBUs and organic linkers that lack the presence of efficient charge carriers (electrons/holes) for conductivity.[22-25] Inspired by their aforementioned potential applications, researchers have invested significant effort to build electrically conducting MOFs in recent years through a number of different strategies. The first and foremost criterion for developing electrically conductive MOFs is to incorporate redox-active ligands and/or mixed-valence metal ions in the MOF frameworks that present accessible charge carriers (electrons/ holes) for efficient charge movement inside the framework that results in conductivity.[22-24,36,37] However, the large separation between the redox-active ligands in the MOF frameworks significantly hinders long-range charge transfer and lower electrical conductivity.[23] To date, the highest reported bulk electrical

conductivity was shown by MOF $Ni_3(HTTP)_2$ (HTTP = 2,3,6,7,10,11-hexaminotriphenylene) (ca. 50 S/cm) is developed by Dinca and co-workers.[38]

Another approach towards conductive MOF is to incorporate electroactive guests inside the porous MOFs that can promote conductivity of the MOFs.[22,23,25] However, in most cases, the guest-promoted conductivity causes a significant loss of the porosity of the frameworks. For instance, Allendorf and co-workers[39] reported a guest-induced improvement of HKUST-1 ($Cu_3(BTC)_2$ MOF with $\sigma \sim 10^{-8}$ S/cm to $10^{-2}$ S/cm at room temperature upon doping of TCNQ (7,7,8,8-tetracyanoquinododimethane) in the pores of MOF with a significant reduction of the porosity.

Several investigations on MOF/polymer composites have been reported in an effort to improve the conductivity of MOFs with encapsulated guests while maintaining significant porosity and surface area of the frameworks.[35,40,41] For instance, Kitagawa and co-workers[35] reported an in-situ polymerization of EDOT (3,4-ethylenedioxythiophene) into conductive PEDOT (poly3,4-ethylenedioxythiophene) inside the MIL-101 (Cr), which led to an enhanced conductivity compared to pristine MOF ($\sigma \sim 10^{-11}$ S/cm vs. $\sim 10^{-3}$ S/cm) while also partially preserving the BET surface area ( ~3100 $m^2/g$ vs. ~803 $m^2/g$). Ballav and co-workers[42] demonstrated a similar study of conductivity enhancement of UiO-66 upon in-situ formation of PEDOT and PPy (polypyrrole) conductive polymers inside its pores that showed significantly higher conductivity ($\sigma \sim 10^{-6}$ S/cm vs. $10^{-4}$ S/cm) and ($\sigma \sim 10^{-6}$ S/cm vs. $\sim 10^{-2}$ S/cm) for UiO-66-PEDOT and UiO-66-PPy MOF/polymer composites, respectively.

In our study, an investigation of enhancement of electrical conductivity of an insulating 3D microporous MOF Zn(NDI-H)[43,44] (**1**) was done by incorporating in-situ polymerized PEDOT and PPy inside the pore of **1**. The pristine **1** exhibited the electrical conductivity σ ~$10^{-14}$ S/cm,[44] whereas the composites **1-PEDOT** and **1-PPy** showed significantly higher electrical conductivity σ = 1.75x$10^{-7}$ S/cm and σ = 2.47x$10^{-5}$ S/cm respectively.

## 4.2.Results and Discussions

The Zn(NDI-H) (**1**) was synthesized by following a protocol reported by Dinca and co-workers.[43] The simulated structure of **1** reported in the literature revealed that the extended three-dimensional framework of **1** consists of tetrahedrally coordinated $Zn^{2+}$ ions bridged by pyrazolate group of the ligand ((**Figure 4.1a**). The framework of **1** possesses an approximately 16 Å wide, one-dimensional pore channel along the c-axis.[43] The Brunauer−Emmett−Teller (BET) surface area of activated **1** was estimated as 1460 $m^2/g$ from $N_2$ sorption analysis.[43] The Powder X-ray Diffraction (PXRD) (**Figure 4.1b**) of as-synthesized **1** matched well with the reported MOF structure, indicating the same structural integrity of **1**.

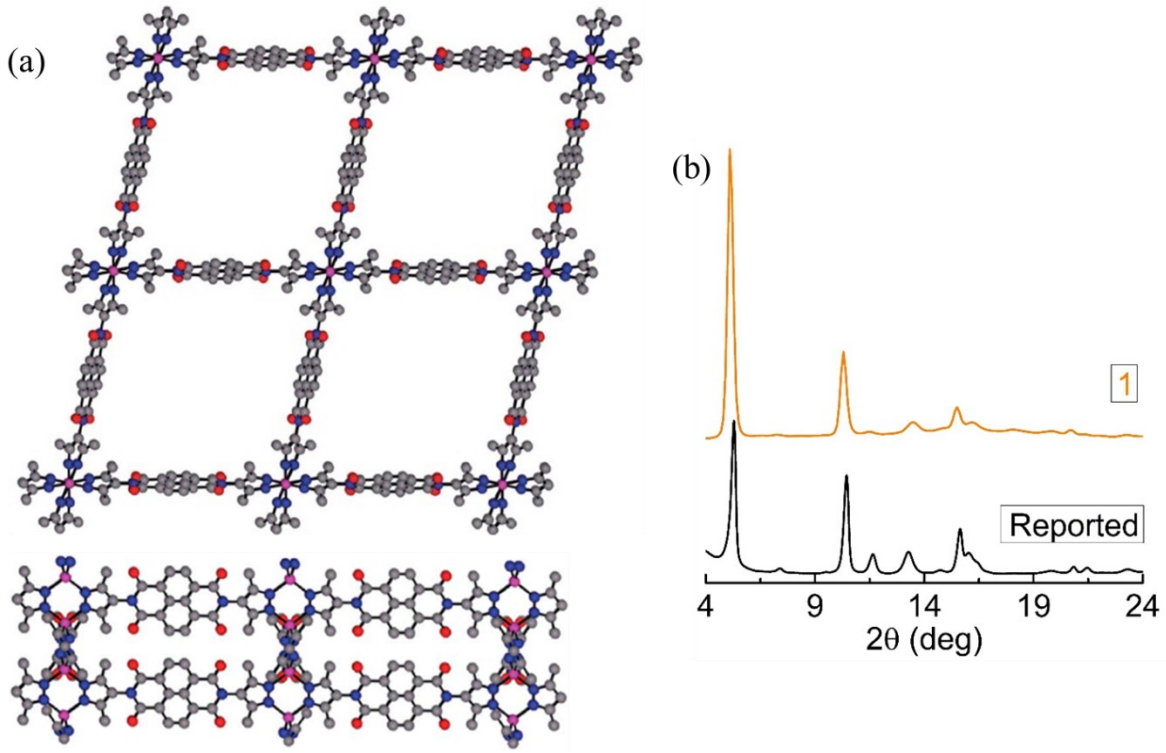


**Figure 4.1:** a) Simulated structure of **1** (adapted with permission from ref. 43. Copyright 2013, Royal Society of Chemistry). Carbon- Grey, Oxygen- Red, Nitrogen- Blue, and Zinc- Pink. b) PXRD of reported (adapted with permission from ref. 43. Copyright 2013, Royal Society of Chemistry) and as-synthesized **1**.

Towards our goal to construct guest-promoted electrically conductive MOF, we have selected conducting poly(3,4-ethylenedioxythiophene) (PEDOT) and polypyrrole (PPy) organic polymers to incorporate as a guest inside the cavity of **1**. The channel size of **1** is sufficiently large to accommodate EDOT or Py monomer inside the pore for the in-situ polymerization of these monomers to PEDOT and PPy, respectively. The PEDOT and PPy incorporation into the MOF cavity was carried out in two steps: a) loading of

respective monomers 3,4-ethylenedioxythiophene (EDOT) and pyrrole (Py) into the cavity of **1**, which are referred to as **1-EDOT** and **1-Py**. b) oxidative polymerization of the monomers inside the MOF cavity. The **1-EDOT** was exposed to $I_2$ vapor at 90°C and **1-Py** to $I_2$ solution (in hexane) at room temperature, respectively, which are referred to as **1-PEDOT** and **1-PPy.**

The monomer EDOT and Py loading in **1** was estimated as approximately 12% (**Figure 4.2a**) and 8% (**Figure 4.2b**) from the thermogravimetric analysis (TGA).[35] In the TGA profile of **1-EDOT** and **1-Py,** the first weight loss (A) in the TGA of **1-EDOT** and **1-PPy** corresponds to the loss of loosely bound solvent and monomer EDOT and Py, respectively. The second weight loss (B) is attributed to the loss of adsorbed EDOT and Py in the pores of **1**. The TGA analysis of pristine **1** showed that it is stable up to 450 °C and the immediate weight loss up to 50 °C, corresponding to the solvent molecules (**Figure 4.2c**). The continuous weight loss **of 1-PEDOT and 1-Py** composite starting at approximately 350 °C and 450 °C can be attributed to a gradual decomposition of the polymer **(Figure 4.2c ).**

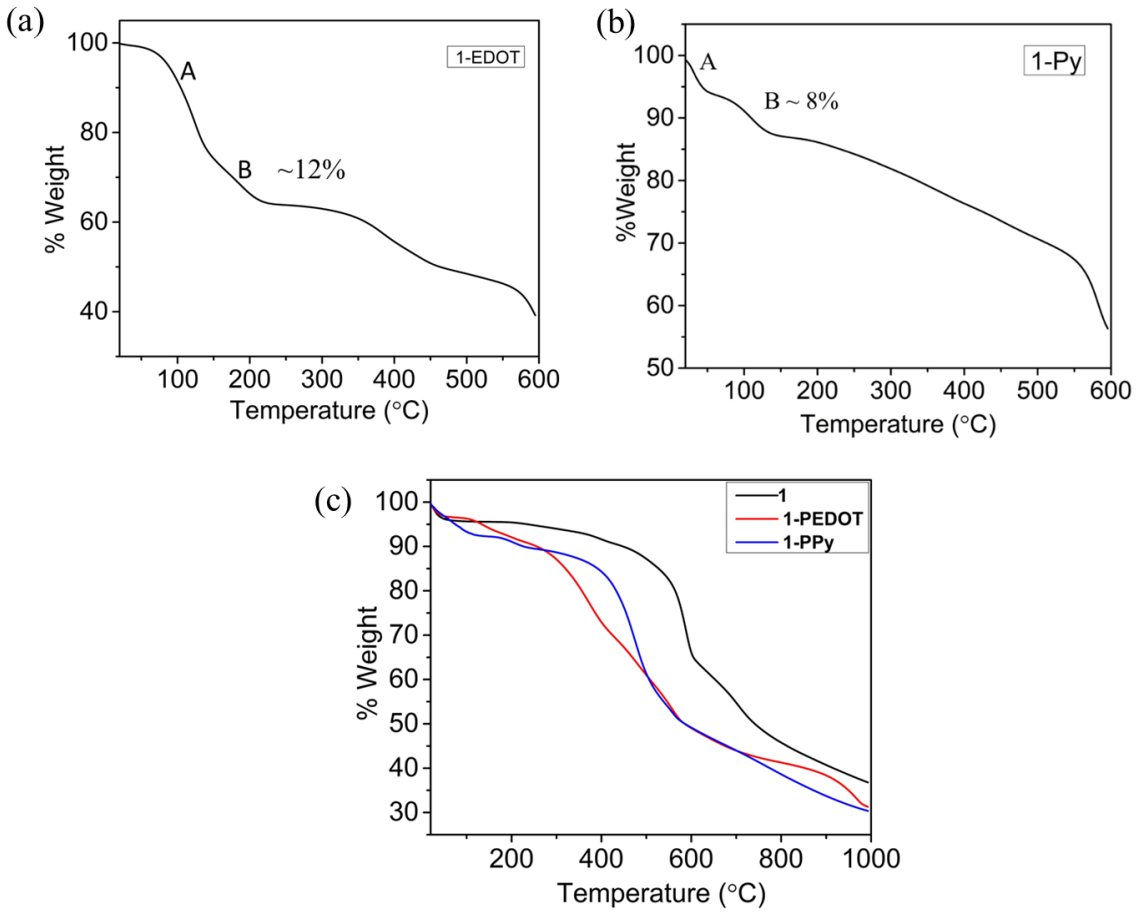


**Figure 4.2:** TGA profile of- a) **1-EDOT**. b) **1-Py**. c) **1, 1-PEDOT, 1-PPy.**

Furthermore, the PXRD data were recorded to confirm the retention of the structure of **1** after monomer loading and in-situ polymerization. The PXRD of both monomer-loaded **1-EDOT**, **1-Py**, and polymerized **1-PEDOT** and **1-PPy** matched well with the PXRD of the pristine **1** (**Figure 4.3**), indicating the retention of the MOF structure after monomer loading and polymerization.

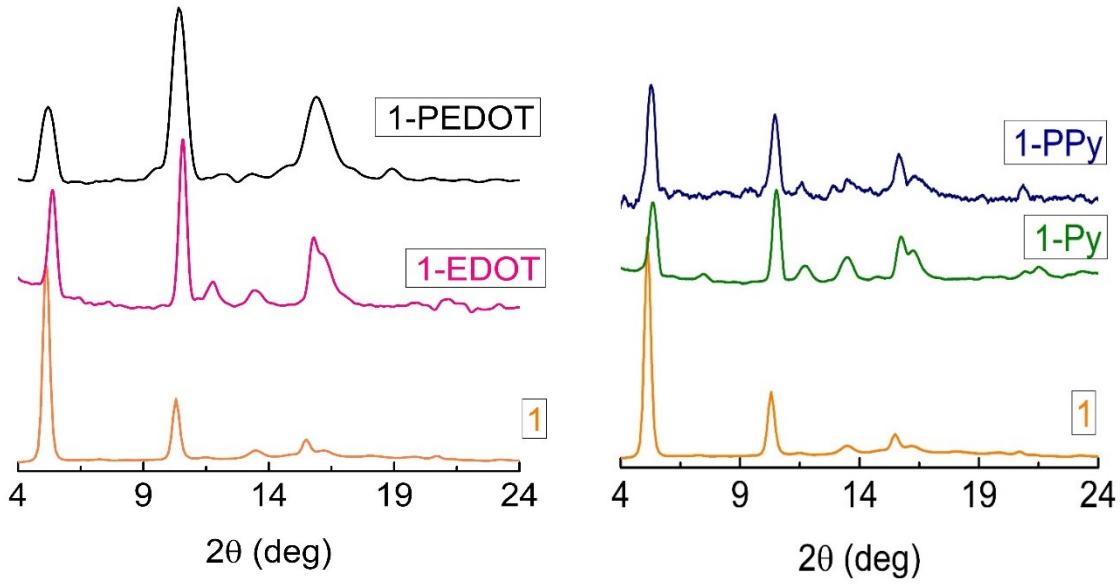


**Figure 4.3**: PXRD pattern of as-synthesized **1**, monomer loaded (**1-EDOT, 1-Py**), and MOF-polymer composites (**1-PEDOT, 1-PPy)**

Moreover, to confirm PEDOT and PPy formation inside the MOF, PEDOT and PPy from the respective MOF-polymer composites were extracted, and FTIR spectrum was recorded for both bulk polymers and the extracted polymers. The IR vibrational bands of the extracted PEDOT and PPy from **1-PEDOT** and **1-PPy** matched with the characteristic IR signals of PEDOT (**Figure 4.4a**) and Py (**Figure 4.4b**), respectively, and confirm the incorporation of polymers inside the MOF pore.[42,45] For the PEDOT, the signals at approximately 1518 $cm^{-1}$ and 1352 $cm^{-1}$ corresponded to the stretching vibration of C=C and C-C bonds, respectively. Other characteristic signals approximately at 1211 $cm^{-1}$, 1068 $cm^{-1,}$ and 984 $cm^{-1}$, 840 $cm^{-1}$ were attributed to the vibrational stretching of C-O-C and C-S bonds, respectively (**Figure 4.4a**).[45]

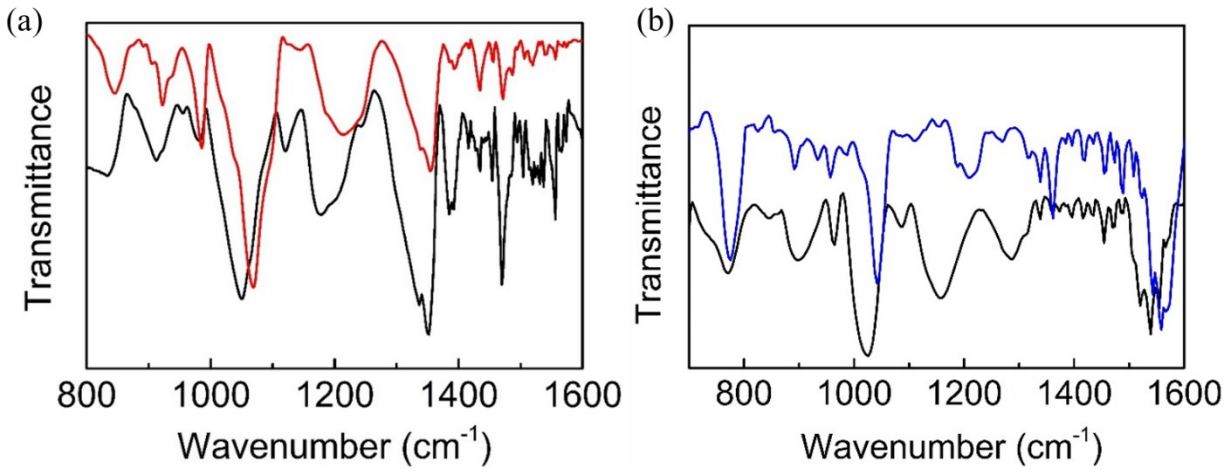


**Figure 4.4**: FTIR spectra of -a) bulk PEDOT (Black) and extracted PEDOT (Red), b) bulk PPy (black), and extracted PPy (blue).

The signals that appeared for PPy (**Figure 4.4b**) at approximately 779 and 891 $cm^{-1}$ are due to C-H out of plane deformation, 1045 $cm^{-1}$ for C-N or N-H in-plane deformation, 1270 $cm^{-1}$ for C-H or C-N in-plane deformation. Other characteristic signals at approximately 1454 $cm^{-1}$ and 1554 $cm^{-1}$ are for C-N stretching C-C stretching vibrations of the pyrrole ring, respectively.[46]

The elemental mapping from energy dispersive X-ray (EDX) coupled with STEM revealed that pristine **1** lacked sulfur (S) (characteristics of PEDOT polymer) and iodine (I) dopant (**Figure 4.5a-b and 4.6a**) whereas, sulfur and iodine are present in the **1-PEDOT** composite (**Figure 4.5c-f and 4.6b**). The STEM-EDX studies also confirm the homogeneous distribution of the PEDOT polymer inside the **1** (**Figure 4.5c-f**), suggesting

the successful incorporation of PEDOT in the pore of **1**. Importantly, EDX elemental mapping of monomer composite **1-EDOT** exhibited the presence of sulfur which confirms the incorporation of EDOT in the pore of **1** (**Appendix C**).

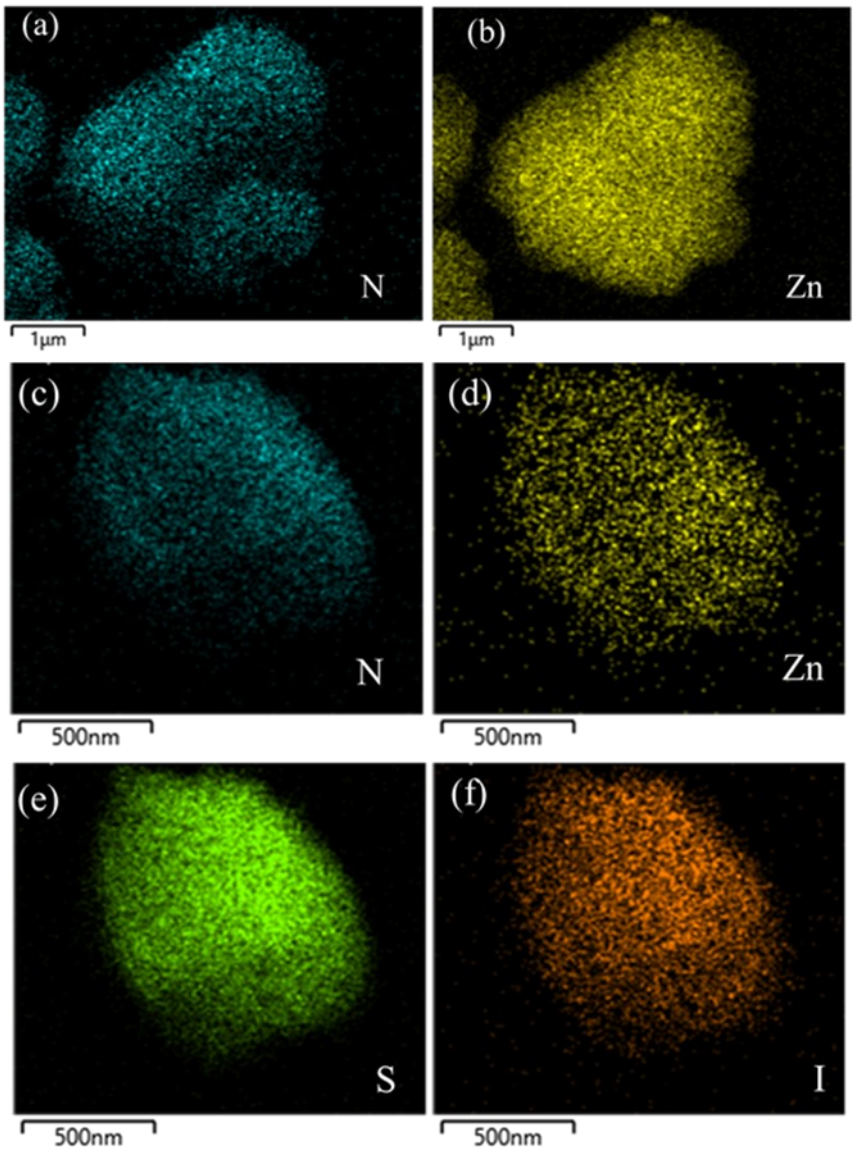


**Figure 4.5:** Elemental mapping of **1** (a-b) and **1-PEDOT** (c-f).

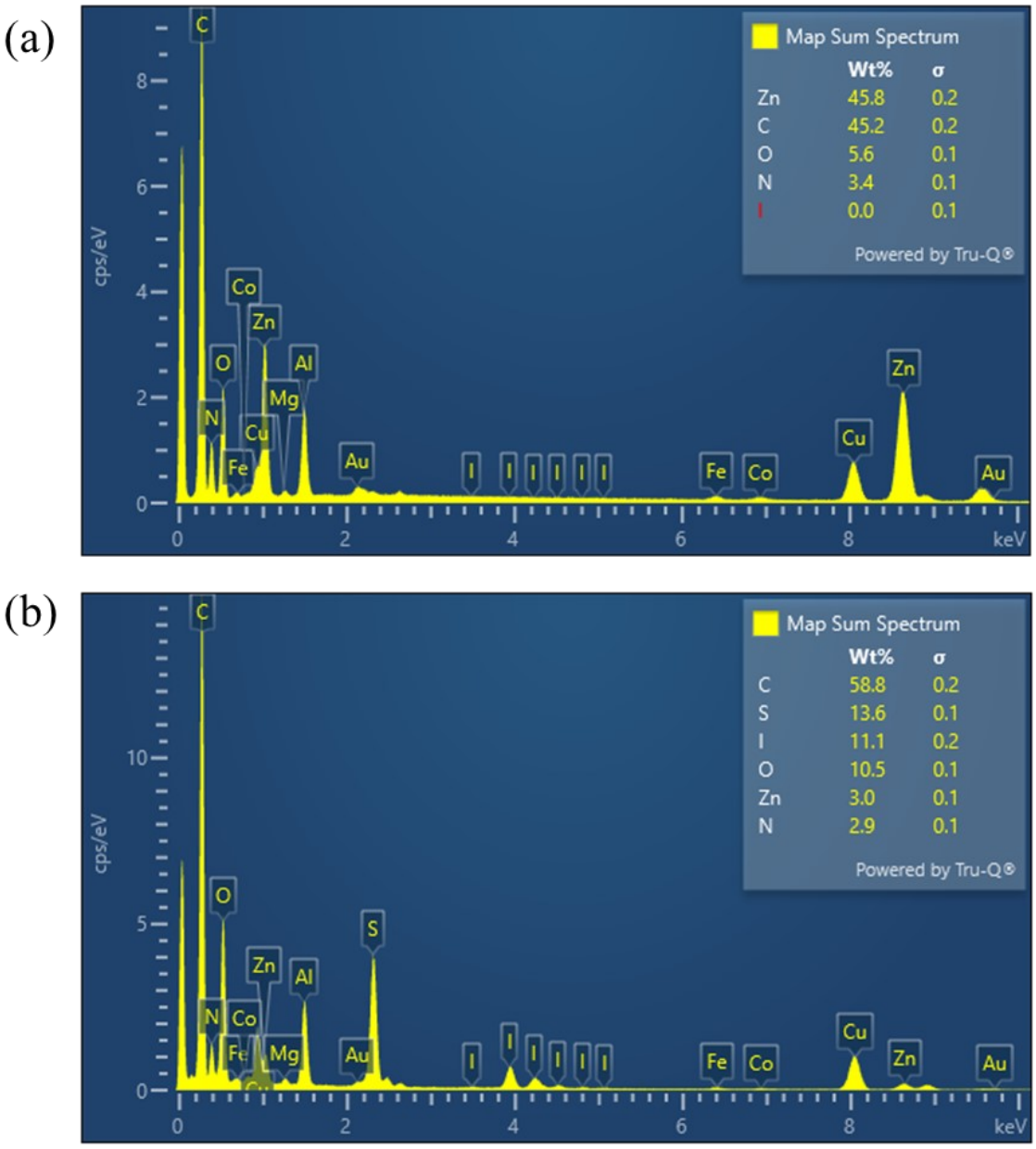


**Figure 4.6:** EDX spectra of (a) **1**. (b) **1-PEDOT**.

Finally, the electrical conductivity (σ) of pristine **1**, **1-PEDOT,** and **1-PPy** was measured by a two-probe direct current-voltage (I-V) technique using a pressed pellet (**Figure 4.7**). The electrical conductivity pristine **1** is reported as approximately $\sigma < 10^{-14}$ S/cm.[44] For the control experiment, pristine 1 was exposed to iodine ($I_2$) at 90 °C for 48h hours and washed with solvents to remove excess iodine that is not trapped in the MOF. The iodine doped 1 (**1**- $I_2$-doped) exhibited similar conductivity as pristine **1** (**Table 4.1**). Gratifyingly, both **1-PEDOT** ($\sigma \sim 1.75 \times 10^{-7}$ S/cm) and **1-PPy** ($\sigma \sim 2.47 \times 10^{-5}$ S/cm) displayed much higher conductivity compared to pristine **1** and **1**- $I_2$-doped ($\sigma < 10^{-14}$). This enhancement of electrical conductivity in the composite **1-PEDOT** and **1-PPy** can be attributed to the better charge transport/conduction through the PEDOT and PPy polymer chains inside the pore of **1**.

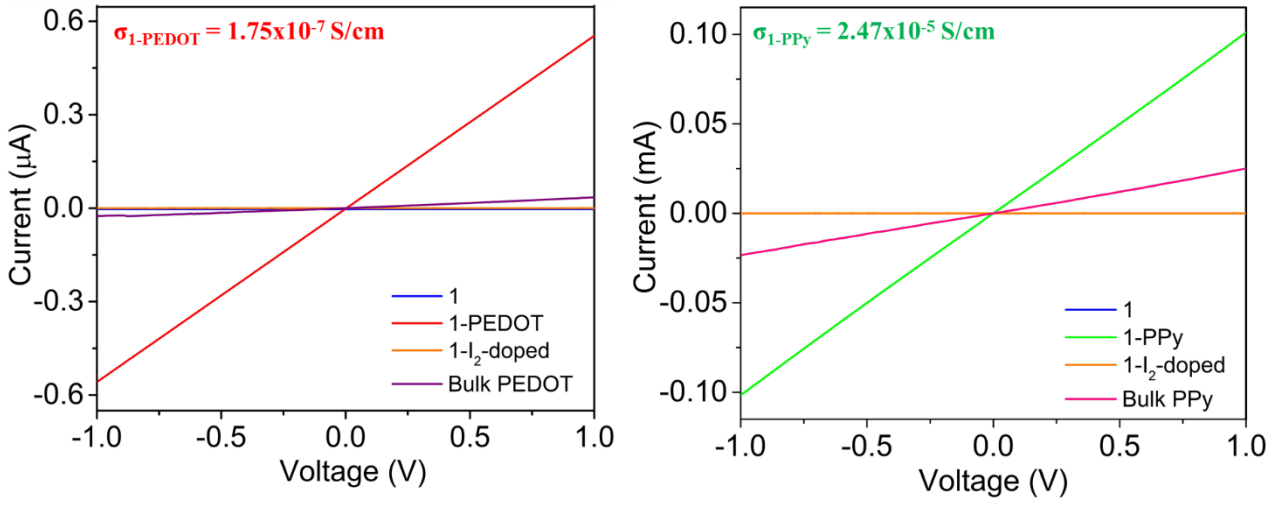


**Figure 4.7:** Current-Voltage (I-V) plots.

**Table 4.1:** Electrical conductivity of pristine **1,** control samples and **1-PEDOT and 1-PPy**.

| Samples | Conductivity σ (S/cm) Pressed pellet | |
|---|---|---|
| **Pristine 1** | $< 10^{-14}$ | |
| **1-$I_2$-doped** | $< 10^{-14}$ | Control experiment |
| **Bulk PEDOT** | $1.95 \times 10^{-8}$ | |
| **Bulk PPy** | $1.214 \times 10^{-5}$ | |
| **1-PEDOT** | $1.75 \times 10^{-7}$ | MOF-polymer composites |
| **1-PPy** | $2.47 \times 10^{-5}$ | |

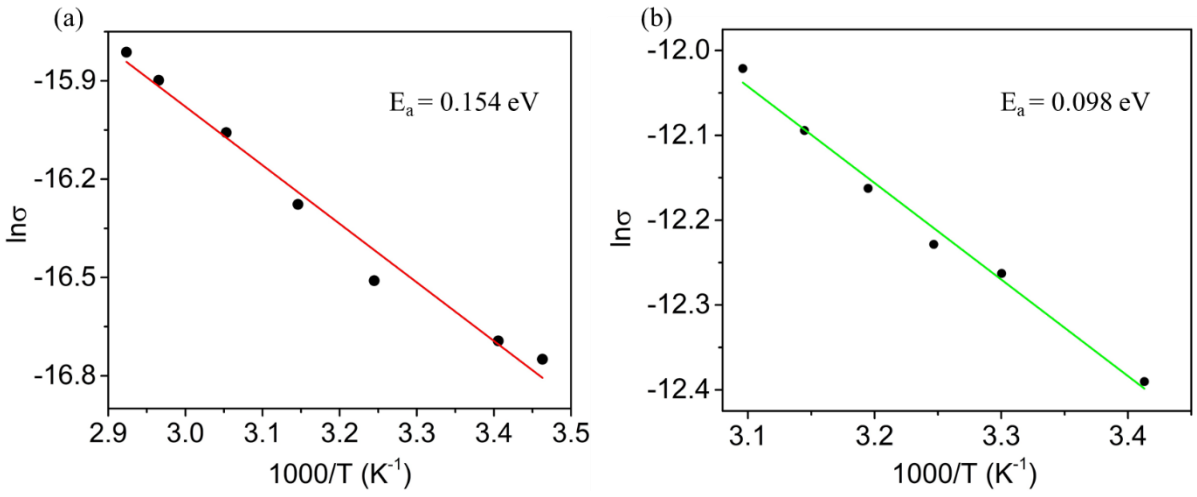


**Figure 4.8:** Arrhenius plot of (a) **1-PEDOT.** (b) **1-PPy**

The temperature-dependent electrical conductivity measurement of **1-PEDOT** and **1-PPy** reflected the semiconducting behavior of these composites. As expected, the electrical conductivity of **1-PEDOT** and **1-PPy** increased with the increase in the temperature and showed a linear fit in the Arrhenius plot (**Figure 4.8**). The thermal activation energy ($E_a$) for **1-PEDOT** and **1-PPy** is calculated as 0.154 eV and 0.098 eV, respectively, from the Arrhenius plot. The higher conductivity of **1-PEDOT** and **1-PPy** than pristine **1** and lower thermal activation energy can be attributed to the formation of PEDOT and PPy in the MOF cavity.

## 4.3.Experimental

### 4.3.1. General materials and methods

1,4,5,8-Naphthalenetetracarboxylic dianhydride (NDA), 3,5-dimethyl-1H-pyrazol-4-amine, EDOT, Py, Iodine crystals, DMF, diethyl ether, and other solvents were purchased from TCI America, ChemBridge, Acros Organic, Alfa Aesar, Fischer chemicals, and VWR chemicals and used as-obtained.

### $^1$H NMR

The proton NMR spectrum was recorded on a Bruker 500 MHz NMR spectrometer.

### Powder X-ray diffraction (PXRD)

PXRD analyses were performed in a Rigaku Ultima IV X-ray diffractometer equipped with a Cu Kα radiation source (λ = 1.5406 Å) and a CCD area detector.

**Thermogravimetric analysis (TGA)**

TGA was performed in a TA Instruments SDT Q600 at a heating rate of 5 °C under $N_2$ were performed to determine the thermal stability of pristine MOF and MOF/polymer composites.

**FTIR**

The FT-IR spectra of the MOF, MOF/polymer composites, and polymers (extracted and bulk) were recorded on a Shimadzu IRAffinity-1S spectrometer.

**I-V measurement**

Using a two-probe technique, the current-voltage (I-V) measurements were performed on pressed pellets of the pristine MOF and MOF/polymer composites at 293K. For constructing the pellets, a two-probe device with two precision-cut stainless-steel rods with flat round tips (radius = 0.135 cm) and a Teflon tube was used. At first, a thin layer of silver was painted on each rod's tip for better electrical contact between the electrodes. Then the materials (approximately 2.5 mg) for this measurement were placed between the two rods in a Teflon tube followed by pressing under approximately 200MPa pressure for about a minute in a digital Parr Pellet Press. The conductivity was calculated using the slope obtained from the I-V curve using the following equation $\sigma = L/RA$.[47]

L = thickness of the pellet = total length of the device with pressed material – length of the device without the material (measured by using a Neiko Electronic Digital Caliper)

R = resistance of the pellet showed in I-V plot, and

A = area of the pellet (=0.057 $cm^2$).

Temperature-dependent I-V measurements were also carried out using this same two-probe technique.

**STEM-EDX**

Scanning Transmission Electron Microscopy (STEM) elemental mapping was recorded in SU9000 coupled with the energy dispersive x-ray (EDX).

### 4.3.2. Synthesis

**Synthesis of NDI-H**

1,4,5,8-Naphthalenetetracarboxylic dianhydride (NDA) (300 g, 1.12 mmol) and 3,5-dimethyl-1H-pyrazol-4-amine (274.29 mg, 2.382 mmol) was refluxed in anhydrous DMF (15 mL) under $N_2$ atmosphere for 8hrs.[43] Diethyl ether was added to the dark brown mixture obtained from the reaction, and the precipitated solid was filtered, followed by recrystallization from DMF/diethyl ether to get NDI-H ligand. The NMR of the obtained product matched well with the reported NMR.

**Synthesis of Zn(NDI-H) (1)**

**1** was synthesized by following a reported protocol.[43] $H_2$NDI-H (40 mg, 0.088 mmol) and $Zn(NO_3)_2$ .$6H_2O$ (28.4 mg, 0.096 mmol) were dissolved in 7 mL DMF, and the vial containing the reaction mixture was kept in an oven at 130 °C for 24h. The resulting MOF was then washed with fresh DMF, MeOH, and diethyl ether at room temperature,

respectively. Then the obtained MOF was activated at 120 °C under vacuum for 24h and used for polymerization.

**Synthesis of 1-PEDOT**

The activated pristine **1** was exposed to monomer EDOT (1µl for 10 mg of **1**) diluted in diethyl ether (1.5 ml) for approximately 48h. The excess monomer was then removed under reduced pressure to obtain **1-EDOT**. Oxidative polymerization of **1-EDOT** was then performed by exposing it to iodine ($I_2$) at 90 °C for 48h.[35,42] The obtained polymerized **1-PEDOT** samples were then washed consecutively with hexane, MeOH, $H_2O$, and acetone to remove excess iodine and dried overnight under vacuum.

**Synthesis of 1-PPy**

The activated pristine **1 (**75 mg) was exposed to pure pyrrole (Py) (1.5 mL) under $N_2$ for 48h.[42] **1-Py** was obtained by removing excess Py under reduced pressure. Oxidant $I_2$ solution (0.05M, in hexane)[48] was added to the **1-Py** and the mixture was kept at room temperature for 24h followed by thorough washing with hexane, methanol, and acetone to obtain **1-PPy** composite.

**Synthesis of Bulk PEDOT**

Bulk PEDOT was synthesized from solution polymerization by following a reported protocol.[42] $I_2$ (1.12g, 4.4 mmol) was dissolved in toluene (15 mL), and then the solution

was added to EDOT (0.25 g, 1.75 mmol) followed by heating at 90 °C for 48h. The obtained black mass was then washed thoroughly with hexane and acetone.

**Synthesis of Bulk PPy**

To synthesize bulk PPy, $FeCl_3$ (0.9 g) was dissolved in water and added slowly to the 166 µl Py (molar ratio of $FeCl_3$: Py = 2.30: 1) at room temperature for 24 hr under constant stirring.[49] The resulting polymer was then washed thoroughly with water and methanol.

**1-$I_2$-doped**

The activated pristine **1** was exposed to iodine ($I_2$) at 90 °C for 48h. The obtained sample was then washed consecutively with hexane, MeOH, $H_2O$, and acetone to remove excess iodine and dried overnight under vacuum and used for I-V measurement as a control.

**Extraction of Polymers**

**1-PEDOT** and **1-PPy** composites were immersed in an aqueous NaOH ($p^H$ ~14) solution for 48h, followed by thorough washing with water and methanol.[42] PEDOT and PPy extracted from the composites were dried under vacuum and used for FTIR analysis.

## 4.4. Conclusions

In summary, we have demonstrated that the conductivity of an insulating MOF increases upon in-situ polymerization of PEDOT and PPy inside the MOF cavity. In comparison to the pristine **1**, the MOF-polymer composites **1-PEDOT** and **1-PPy** exhibited significantly

higher electrical conductivity $\sigma \sim 1.75 \times 10^{-7}$ S/cm and $\sigma \sim 2.47 \times 10^{-5}$ S/cm, respectively. These results demonstrate guest promoted electrical conductivity enhancement in the porous MOF. The BET surface area measurements are needed to be done to investigate further the change of porosity and degree of retention of porosity in the MOF-polymer composites. If the BET analysis shows significant retention of porosity, then the chemiresistive sensing of the MOF-polymer composites would be investigated.

## 4.5. References


1. Furukawa, H.; Cordova, K. E.; O'Keeffe, M.; Yaghi, O. M. The Chemistry and Applications of Metal-Organic Frameworks. *Science* **2013**, *341*, 1230444:1–12.
2. Farha, O. K.; Eryazici, I.; Jeong, N. C.; Hauser, B. G.; Wilmer, C. E.; Sarjeant, A. A.; Snurr, R. Q.; Nguyen, S. T.; Yazaydın, A. Ö.; Hupp, J. T. Metal−Organic Framework Materials with Ultrahigh Surface Areas: Is the Sky the Limit? *J. Am. Chem. Soc*. **2012**, *134*, 15016−15021.
3. Hçnicke, I. M.; Senkovska, I.; Bon, V.; Baburin, I. A.; Bçnisch, N.; Raschke, S.; Evans, J. D.; Kaskel, S. Balancing Mechanical Stability and Ultrahigh Porosity in Crystalline Framework Materials. *Angew. Chem. Int. Ed.* **2018**, *57*, 13780 –13783.
4. Furukawa, H.; Ko, N.; Go, Y. B.; Aratani, N.; Choi, S. B.; Choi, E.; Yazaydin, Ö.; Snurr, R. Q.; O′Keeffe, M.; Kim, J.; Yaghi, O. M. Ultrahigh Porosity in Metal-Organic Frameworks. *Science* **2010**, *329*, 424–428.

5. Eddaoudi, M.; Kim, J.; Rosi, Nathaniel.; Vodak, D.; Wachter, J.; O'Keeffe, M.; Yaghi, O. M. Systematic Design of Pore Size and Functionality in Isoreticular MOFs and Their Application in Methane Storage. *Science* **2002,** *295,* 469–472.
6. Cavka, J. H.; Jakobsen, S.; Olsbye, U.; Guillou, N.; Lamberti, C.; Bordiga, S.; Lillerud, K. P. A New Zirconium Inorganic Building Brick Forming Metal Organic Frameworks with Exceptional Stability. *J. Am. Chem. Soc*. **2008**, *130*, 13850–13851.
7. Schaate, A.; Roy, P.; Godt, A.; Lippke, J.; Waltz, F.; Wiebcke, M.; Behrens, P. Modulated Synthesis of Zr-Based Metal–Organic Frameworks: From Nano to Single Crystals. *Chem. Eur. J*. **2011**, *17*, 6643 – 6651.
8. Islamoglu, T.; Goswami, S.; Li, Z.; Howarth, A. J.; Farha, O. K.; Hupp, J. T. Postsynthetic Tuning of Metal−Organic Frameworks for Targeted Applications. *Acc. Chem. Res*. **2017**, *50*, 805−813.
9. Cohen, S.M. Postsynthetic Methods for the Functionalization of Metal-Organic Frameworks. *Chem. Rev*. **2012**, *112*, 970–1000.
10. Mason, J. A.; Veenstra, M.; Long, J. R. Evaluating Metal−Organic Frameworks for Natural Gas Storage. *Chem. Sci.* **2014**, *5*, 32−51.
11. Sumida, K.; Rogow, D. L.; Mason, J. A.; McDonald, T. M.; Bloch, E. D.; Herm, Z. R.; Bae, T.-H.; Long, J. R. Carbon Dioxide Capture in MetalOrganic Frameworks. *Chem. Rev.* **2012**, *112*, 724–781.
12. Murray, L. J.; Dincă, M.; Long, J. R. Hydrogen Storage in Metal-Organic Frameworks. *Chem. Soc. Rev*. **2009**, *38*, 1294−1314.

13. Suh, M. P.; Park, H. J.; Prasad, T. K.; Lim, D.-W. Hydrogen Storage in Metal-Organic Frameworks. *Chem. Rev.* **2012**, *112*, 782–835.

14. Li, J.-R.; Kuppler, R. J.; Zhou, H.-C. Selective Gas Adsorption and Separation in Metal-Organic Frameworks. *Chem. Soc. Rev*. **2009**, *38*, 1477−1504.

15. Lustig, W. P.; Mukherjee, S.; Rudd, N. D.; Desai, A. V.; Li, J.; Ghosh, S. K. Metal–organic frameworks: functional luminescent and photonic materials for sensing applications. *Chem. Soc. Rev.,* **2017,** *46,* 3242–3285.

16. Fateeva, A.; Chater, P. A.; Ireland, C. P.; Tahir, A. A.; Khimyak, Y. Z.; Wiper, P. V.; Darwent, J. R.; Rosseinsky, M. J. A Water-Stable Porphyrin-Based Metal–Organic Framework Active for Visible-Light Photocatalysis. *Angew. Chem. Int. Ed*. **2012,** *51,* 7440–7444.

17. Yee, K.-K.; Reimer, N.; Liu, J.; Cheng, S.-Y.; Yiu, S.-M.; Weber, J.; Stock, N.; Xu, Z. Effective Mercury Sorption by Thiol-Laced Metal−Organic Frameworks: in Strong Acid and the Vapor Phase. *J. Am. Chem. Soc.* **2013,** *135,* 7795–7798.

18. Zhao, D.; Cui, Yuanjing, Yang, Y.; Qian, G. Sensing-functional luminescent metal–organic Frameworks. *CrystEngComm,* **2016**, *18,* 3746–3759.

19. Xu, H.; Cao, C.-S.; Kanga, X.-M.; Zhao, B. Lanthanide-based metal–organic frameworks as luminescent probes. *Dalton Trans.,* **2016,** *45,* 18003–18017.

20. Cui, Y.; Yue, Y.; Qian, G.; Chen, B. Luminescent Functional Metal-Organic Frameworks. *Chem. Rev*. **2012,** *112,* 1126–1162.

21. Allendorf, M. D.; Bauer, C. A.; Bhakta, R. K.; Houk, R. J. T. Luminescent metal–organic frameworks. *Chem. Soc. Rev.,* **2009**, *38,* 1330–1352.

22. Xie, L. S.; Skorupskii, G.; Dincă, M. Electrically Conductive Metal−Organic Frameworks. *Chem. Rev*. **2020**, *120*, 8536−8580.

23. Nidamanuri, N.; Maity, K.; Saha, S. Electrically Conductive Metal-Organic Frameworks: Elaboration and Applications of Meta-Organic Frameworks; World Scientific, 2018; pp 655-686.

24. D'Alessandro, D. M.; Kanga, J. R. R.; Caddy, J. S. Towards Conducting Metal-Organic Frameworks. *Aust. J. Chem.* **2011**, *64*, 718–722.

25. Sun, L.; Campbell, M. G.; Dincă, M. Electrically Conductive Porous Metal–Organic Frameworks. *Angew. Chem. Int. Ed*. **2016**, *55*, 3566 – 3579.

26. Miner, E. M.; Wanga, L.; Dincă, M. Modular $O_2$ electroreduction activity in triphenylene-based metal–organic frameworks. *Chem. Sci*., **2018**, *9*, 6286–6291.

27. Miner, E. M.; Fukushima, T.; Sheberla, D.; Sun, L.; Surendranath, Y.; Dincă, M. Electrochemical Oxygen Reduction Catalysed by $Ni_3$(Hexaiminotriphenylene)$_2$. *Nat. Commun.* **2016**, *7*, 10942.

28. Kempahanumakkagari, S.; Vellingiri, K.; Deep, A.; Kwon, E. E.; Bolan, N.; Kim, K-H. Metal–organic framework composites as electrocatalysts for electrochemical sensing applications. *Coordination Chemistry Reviews*, **2018**, *357*, 105–129.

29. Clough, A. J.; Yoo, J. W.; Mecklenburg, M. H.; Marinescu, S. C. Two-Dimensional Metal−Organic Surfaces for Efficient Hydrogen Evolution from Water. *J. Am. Chem. Soc*. **2015**, *137*, 118−121.

30. Park, J.; Lee, M.; Feng, D.; Huang, Z.; Hinckley, A. C.; Yakovenko, A.; Zou, X.; Cui, Y.; Bao, Z. Stabilization of Hexaaminobenzene in a 2D Conductive Metal-

Organic Framework for High Power Sodium Storage. *J. Am. Chem. Soc*. **2018**, *140*, 10315−10323.

31. Shinde, S. S.; Lee, C. H.; Jung, J.-Y.; Wagh, N. K.; Kim, S.-H.; Kim, D.-H.; Lin, C.; Lee, S. U.; Lee, J.-H. Unveiling Dual-Linkage 3D Hexaiminobenzene Metal-Organic Frameworks towards Long-Lasting Advanced Reversible Zn-Air Batteries. *Energy Environ. Sci.* **2019**, *12*, 727−738.
32. Rubio-Gimenez, V.; Almora-Barrios, N.; Escorcia-Ariza, G.; Galbiati, M.; Sessolo, M.; Tatay, S.; Marti-Gastaldo, C. Origin of the Chemiresistive Response of Ultrathin Films of Conductive Metal- Organic Frameworks. *Angew. Chem., Int. Ed*. **2018**, *57*, 15086−15090.
33. Campbell, M. G.; Liu, S. F.; Swager, T. M.; Dincă, M. Chemiresistive Sensor Arrays from Conductive 2D Metal-Organic Frameworks. *J. Am. Chem. Soc*. **2015**, *137*, 13780−13783.
34. Aubrey, M. L.; Kapelewski, M. T.; Melville, J. F.; Oktawiec, J.; Presti, D.; Gagliardi, L.; Long, J. R. Chemiresistive Detection of Gaseous Hydrocarbons and Interrogation of Charge Transport in Cu[Ni(2,3-Pyrazinedithiolate)$_2$] by Gas Adsorption. *J. Am. Chem. Soc.* **2019**, *141*, 5005−5013.
35. Ouay, B. L.; Boudot, M.; Kitao, T.; Yanagida, T.; Kitagawa, S.; Uemura, T. Nanostructuration of PEDOT in Porous Coordination Polymers for Tunable Porosity and Conductivity. *J. Am. Chem. Soc.* **2016**, *138*, 10088−10091.
36. Sun, L.; Miyakai, T.; Seki, S.; Dincă, M. $Mn_2$(2,5-Disulfhydrylbenzene-1,4-Dicarboxylate): A Microporous Metal−Organic Framework with Infinite

(−Mn−S−)∞ Chains and High Intrinsic Charge Mobility. *J. Am. Chem. Soc*. **2013**, *135*, 8185−8188.

37. Sun, L.; Hendon, C. H.; Minier, M. A.; Walsh, A.; Dincă, M. Million-Fold Electrical Conductivity Enhancement in $Fe_2$(DEBDC) versus $Mn_2$(DEBDC) (E = S, O). *J. Am. Chem. Soc.* **2015**, *137*, 6164−6167.
38. Sun, L.; Liao, B.; Sheberla, D.; Kraemer, D.; Zhou, J.; Stach, E. A.; Zakharov, D.; Stavila, V.; Talin, A. A.; Ge, Y.; Allendorf, M. D.; Chen, G.; Léonard, F.; Dinca, M. A Microporous and Naturally Nanostructured Thermoelectric Metal-Organic Framework with Ultralow Thermal Conductivity. *Joule* **2017**, *1*, 168–177.
39. Talin, A. A.; Centrone, A.; Ford, A. C.; Foster, M. E.; Stavila, V.; Haney, P.; Kinney, R. A.; Szalai, V.; Gabaly, F. E.; Yoon, H. P.; Léonard, F.; Allendorf, M. D. Tunable Electrical Conductivity in Metal-Organic Framework Thin-Film Devices. *Science* **2014**, *343*, 66–69.
40. Wang, T. C.; Hod, I.; Audu, C. O.; Vermeulen, N. A.; T. Nguyen, S. T.; Farha, O. M.; Hupp, J. T. Rendering High Surface Area, Mesoporous Metal−Organic Frameworks Electronically Conductive. *ACS Appl. Mater. Interfaces* **2017**, *9*, 12584−12591.
41. Salcedo-Abraira, P.; Santiago-Portillo, A.; Atienzar,P.; Bordet, P.; Salles, F.; Guillou, N.; Elkaim, E.; Garcia, H.; Navalon, S.; Horcajada, P. A highly conductive nanostructured PEDOT polymer confined into the mesoporous MIL-100(Fe). *Dalton Trans*., **2019**, *48*, 9807–9817.

42. Jadhav, A.; Gupta, K.; Ninawe, P.; Ballav, N. Imparting Multifunctionality by Utilizing Biporosity in a Zirconium-Based Metal–Organic Framework. *Angew. Chem*. **2020**, *132*, 2235 –2239.

43. Wade, C. R.; Corrales-Sanchez, T.; Narayan, T. C.; Dincă, M. Postsynthetic tuning of hydrophilicity in pyrazolate MOFs to modulate water adsorption properties. *Energy Environ. Sci*., **2013**, *6*, 2172–2177.

44. Wentz, H. C.; Skorupskii, G.; Bonfim, A. B.; Mancuso, J. L.; Hendon, C. H.; Oriel, E. H.; Sazamad, G. T.; Campbell, M. G. Switchable electrical conductivity in a three-dimensional metal–organic framework via reversible ligand n-doping. *Chem. Sci*., **2020**, *11*, 1342–1346.

45. Zhang, J.; Zhao, X. S. Conducting Polymers Directly Coated on Reduced Graphene Oxide Sheets as High-Performance Supercapacitor Electrodes. *J. Phys. Chem. C* **2012**, *116*, 5420−5426.

46. Ćirić-Marjanović, G.; Mentus, S.; Pašti, I.; Gavrilov, N.; Krstić, J.; Travas-Sejdic, J.; Strover, L. T.; Kopecká, J.; Moravková, Z.; Trchová, M.; Stejskal, J. Synthesis, Characterization, and Electrochemistry of Nanotubular Polypyrrole and Polypyrrole-Derived Carbon Nanotubes *J. Phys. Chem. C* **2014**, *118*, 14770–14784.

47. Yadav, A.; Panda, D. K. Zhang, S.; Zhou, W.; Saha, S. Electrically Conductive 3D Metal−Organic Framework Featuring π-Acidic Hexaazatriphenylene Hexacarbonitrile Ligands with Anion−π Interaction and Efficient Charge-Transport Capabilities. *ACS Appl. Mater. Interfaces* **2020**, *12*, 40613−40619.

48. Wang, Q-X.; Zhang, C-Y. Oriented Synthesis of One-Dimensional Polypyrrole Molecule Chains in a Metal-Organic Framework. *Macromol. Rapid Commun*. **2011**, *32,* 1610–1614.

49. Armes, S. P. OPTIMUM REACTION CONDITIONS FOR THE POLYMERIZATION OF PYRROLE BY IRON(III) CHLORIDE IN AQUEOUS SOLUTION. *Synthetic Metals*, **1987**, *20*, 365–371.

## APPENDIX A

## SINGLE CRYSTAL X-RAY DATA FOR $Zn_2(NDC)_2(DPTTZ)\cdot(DMF)_2$

**Table A.1. Sample and crystal data for $Zn_2(NDC)_2(DPTTZ)\cdot(DMF)_2$**

| | | |
|---|---|---|
| **Chemical formula** | $C_{44}H_{34}N_6O_{10}S_2Zn_2$ | |
| **Formula weight** | 1001.63 g/mol | |
| **Temperature** | 140(2) K | |
| **Wavelength** | 0.71073 Å | |
| **Crystal size** | 0.051 x 0.132 x 0.187 mm | |
| **Crystal system** | triclinic | |
| **Space group** | P -1 | |
| **Unit cell dimensions** | a = 8.0961(13) Å | |
| | b = 10.5093(15) Å | α = 75.761(5)° |
| | c = 12.981(2) Å | β = 77.486(6)° |
| **Volume** | 1044.5(3) $Å^3$ | γ = 88.858(5)° |
| **Z** | 1 | |
| **Density (calculated)** | 1.592 $g/cm^3$ | |
| **Absorption coefficient** | 1.317 $mm^{-1}$ | |
| **F(000)** | 512 | |

**Table A.2. Data collection and structure refinement for $Zn_2(NDC)_2(DPTTZ)\cdot(DMF)_2$**

| | | |
|---|---|---|
| **Theta range for data collection** | 2.58 to 26.39° | |
| **Index ranges** | -10<=h<=10, -13<=k<=13, -16<=l<=16 | |
| **Reflections collected** | 49321 | |
| **Independent reflections** | 4257 [R(int) = 0.0587] | |
| **Max. and min. transmission** | 0.9360 and 0.7910 | |
| **Structure solution technique** | direct methods | |
| **Structure solution program** | XT, VERSION 2014/4 | |
| **Refinement method** | Full-matrix least-squares on $F^2$ | |
| **Refinement program** | SHELXL-2014/7 (Sheldrick, 2014) | |
| **Function minimized** | $\Sigma\, w(F_o^2 - F_c^2)^2$ | |
| **Data / restraints / parameters** | 4257 / 34 / 335 | |
| **Goodness-of-fit on $F^2$** | 1.093 | |
| **$\Delta/\sigma_{max}$** | 0.001 | |
| **Final R indices** | 3889 data; I>2σ(I) | R1 = 0.0350, wR2 = 0.0838 |
| | all data | R1 = 0.0406, wR2 = 0.0862 |
| **Weighting scheme** | $w=1/[\sigma^2(F_o^2)+(0.0318P)^2+2.0747P]$ where $P=(F_o^2+2F_c^2)/3$ | |

| | |
|---|---|
| **Largest diff. peak and hole** | 0.671 and -0.913 eÅ$^{-3}$ |
| **R.M.S. deviation from mean** | 0.082 eÅ$^{-3}$ |

**Table A.3. Atomic coordinates and equivalent isotropic atomic displacement parameters (Å$^2$) for $Zn_2(NDC)_2(DPTTZ)\cdot(DMF)_2$**

U(eq) is defined as one third of the trace of the orthogonalized $U_{ij}$ tensor.

| | x/a | y/b | z/c | U(eq) |
|---|---|---|---|---|
| Zn1 | 0.84272(3) | 0.91783(3) | 0.54592(2) | 0.00903(9) |
| S1 | 0.74958(10) | 0.54570(9) | 0.02038(8) | 0.0402(2) |
| O1 | 0.8200(2) | 0.90637(18) | 0.39430(14) | 0.0191(4) |
| O2 | 0.0563(2) | 0.03303(19) | 0.33439(15) | 0.0218(4) |
| O3 | 0.0172(2) | 0.77645(17) | 0.54189(16) | 0.0182(4) |
| O4 | 0.2569(2) | 0.90071(16) | 0.48068(15) | 0.0157(4) |
| N1 | 0.6416(3) | 0.8105(2) | 0.65052(17) | 0.0144(4) |
| N2 | 0.0651(4) | 0.6352(3) | 0.8820(2) | 0.0362(7) |
| C1 | 0.9395(3) | 0.9674(3) | 0.3201(2) | 0.0162(5) |
| C2 | 0.9422(4) | 0.9633(3) | 0.2047(2) | 0.0201(6) |
| C3 | 0.8338(4) | 0.8741(3) | 0.1836(2) | 0.0298(7) |
| C4 | 0.8363(4) | 0.8703(4) | 0.0786(2) | 0.0341(8) |
| C5 | 0.0544(4) | 0.0451(3) | 0.0106(2) | 0.0231(6) |
| C6 | 0.0500(4) | 0.0462(3) | 0.1198(2) | 0.0231(6) |

| | x/a | y/b | z/c | U(eq) |
|---|---|---|---|---|
| C7 | 0.1761(3) | 0.7917(2) | 0.5129(2) | 0.0135(5) |
| C8 | 0.2762(3) | 0.6694(2) | 0.5155(2) | 0.0146(5) |
| C9 | 0.1896(3) | 0.5448(3) | 0.5489(2) | 0.0199(6) |
| C10 | 0.2770(3) | 0.4325(3) | 0.5481(2) | 0.0191(6) |
| C11 | 0.5435(3) | 0.5624(2) | 0.4838(2) | 0.0142(5) |
| C12 | 0.4493(3) | 0.6769(2) | 0.4838(2) | 0.0144(5) |
| C13 | 0.6620(4) | 0.6906(3) | 0.7118(3) | 0.0304(7) |
| C14 | 0.5307(4) | 0.6159(3) | 0.7862(3) | 0.0352(8) |
| C15 | 0.3700(4) | 0.6658(3) | 0.7994(2) | 0.0229(6) |
| C16 | 0.3478(4) | 0.7888(3) | 0.7359(2) | 0.0233(6) |
| C17 | 0.4860(3) | 0.8578(3) | 0.6633(2) | 0.0204(6) |
| C18 | 0.2235(4) | 0.5950(3) | 0.8792(2) | 0.0255(6) |
| C19 | 0.9639(4) | 0.5507(3) | 0.9695(3) | 0.0307(7) |
| N3 | 0.3575(13) | 0.8058(11) | 0.1576(8) | 0.049(2) |
| C20 | 0.4061(15) | 0.9131(14) | 0.2005(11) | 0.060(3) |
| C21 | 0.255(2) | 0.6960(14) | 0.2340(14) | 0.074(4) |
| C22 | 0.4156(19) | 0.8066(16) | 0.0531(11) | 0.073(3) |
| O5 | 0.3912(16) | 0.7109(13) | 0.0223(9) | 0.110(4) |
| N3B | 0.2733(11) | 0.7460(9) | 0.1763(6) | 0.0519(19) |
| C21B | 0.1461(14) | 0.6594(10) | 0.2549(9) | 0.079(3) |
| C20B | 0.3868(13) | 0.8173(15) | 0.2136(10) | 0.082(3) |
| C22B | 0.2861(13) | 0.7624(10) | 0.0703(7) | 0.073(3) |
| O5B | 0.3947(13) | 0.8294(11) | 0.9983(7) | 0.108(3) |

**Table A.4. Bond lengths (Å) for $Zn_2(NDC)_2(DPTTZ)\cdot(DMF)_2$**

| | | | |
|---|---|---|---|
| Zn1-N1 | 2.032(2) | Zn1-O3 | 2.0317(18) |
| Zn1-O4 | 2.0353(17) | Zn1-O1 | 2.0486(18) |
| Zn1-O2 | 2.0764(19) | Zn1-Zn1 | 2.9558(7) |
| S1-C19 | 1.715(3) | S1-C18 | 1.760(3) |
| O1-C1 | 1.262(3) | O2-C1 | 1.253(3) |
| O2-Zn1 | 2.0764(19) | O3-C7 | 1.262(3) |
| O4-C7 | 1.262(3) | O4-Zn1 | 2.0353(17) |
| N1-C17 | 1.337(3) | N1-C13 | 1.343(4) |
| N2-C18 | 1.337(4) | N2-C19 | 1.371(4) |
| C1-C2 | 1.505(3) | C2-C6 | 1.370(4) |
| C2-C3 | 1.410(4) | C3-C4 | 1.369(4) |
| C3-H3 | 0.95 | C4-C5 | 1.413(4) |
| C4-H4 | 0.95 | C5-C4 | 1.413(4) |
| C5-C6 | 1.413(4) | C5-C5 | 1.420(6) |
| C6-H6 | 0.95 | C7-C8 | 1.503(3) |
| C8-C12 | 1.370(4) | C8-C9 | 1.421(4) |
| C9-C10 | 1.366(4) | C9-H9 | 0.95 |
| C10-C11 | 1.420(4) | C10-H10 | 0.95 |
| C11-C12 | 1.412(3) | C11-C10 | 1.420(4) |
| C11-C11 | 1.424(5) | C12-H12 | 0.95 |
| C13-C14 | 1.376(4) | C13-H13 | 0.95 |
| C14-C15 | 1.385(4) | C14-H14 | 0.95 |

| | | | |
|---|---|---|---|
| C15-C16 | 1.383(4) | C15-C18 | 1.469(4) |
| C16-C17 | 1.380(4) | C16-H16 | 0.95 |
| C17-H17 | 0.95 | C18-S1 | 1.760(3) |
| C19-C19 | 1.365(6) | N3-C22 | 1.335(13) |
| N3-C21 | 1.456(18) | N3-C20 | 1.469(15) |
| C20-H20A | 0.98 | C20-H20B | 0.98 |
| C20-H20C | 0.98 | C21-H21A | 0.98 |
| C21-H21B | 0.98 | C21-H21C | 0.98 |
| C22-O5 | 1.205(14) | C22-H22 | 0.95 |
| N3B-C22B | 1.324(10) | N3B-C20B | 1.428(14) |
| N3B-C21B | 1.434(13) | C21B-H21D | 0.98 |
| C21B-H21E | 0.98 | C21B-H21F | 0.98 |
| C20B-H20D | 0.98 | C20B-H20E | 0.98 |
| C20B-H20F | 0.98 | C22B-O5B | 1.220(12) |
| C22B-H22B | 0.95 | | |

**Table A.5. Bond angles (°) for $Zn_2(NDC)_2(DPTTZ)\cdot(DMF)_2$**

| | | | |
|---|---|---|---|
| N1-Zn1-O3 | 100.14(8) | N1-Zn1-O4 | 100.20(8) |
| O3-Zn1-O4 | 159.46(7) | N1-Zn1-O1 | 105.08(8) |
| O3-Zn1-O1 | 88.01(8) | O4-Zn1-O1 | 89.47(7) |
| N1-Zn1-O2 | 95.51(8) | O3-Zn1-O2 | 87.44(8) |
| O4-Zn1-O2 | 87.78(8) | O1-Zn1-O2 | 159.39(8) |
| N1-Zn1-Zn1 | 163.18(6) | O3-Zn1-Zn1 | 79.58(5) |
| O4-Zn1-Zn1 | 80.13(5) | O1-Zn1-Zn1 | 91.73(6) |
| O2-Zn1-Zn1 | 67.68(6) | C19-S1-C18 | 87.99(14) |
| C1-O1-Zn1 | 112.26(16) | C1-O2-Zn1 | 142.98(18) |
| C7-O3-Zn1 | 127.81(16) | C7-O4-Zn1 | 126.81(16) |
| C17-N1-C13 | 117.7(2) | C17-N1-Zn1 | 121.49(18) |
| C13-N1-Zn1 | 120.79(19) | C18-N2-C19 | 106.5(3) |
| O2-C1-O1 | 125.2(2) | O2-C1-C2 | 116.8(2) |
| O1-C1-C2 | 118.0(2) | C6-C2-C3 | 119.8(3) |
| C6-C2-C1 | 120.1(2) | C3-C2-C1 | 120.1(3) |
| C4-C3-C2 | 120.1(3) | C4-C3-H3 | 119.9 |
| C2-C3-H3 | 119.9 | C3-C4-C5 | 121.4(3) |
| C3-C4-H4 | 119.3 | C5-C4-H4 | 119.3 |
| C4-C5-C6 | 122.6(3) | C4-C5-C5 | 118.5(3) |
| C6-C5-C5 | 118.9(3) | C2-C6-C5 | 121.3(3) |
| C2-C6-H6 | 119.3 | C5-C6-H6 | 119.3 |
| O4-C7-O3 | 125.4(2) | O4-C7-C8 | 117.7(2) |

| | | | |
|---|---|---|---|
| O3-C7-C8 | 116.9(2) | C12-C8-C9 | 119.8(2) |
| C12-C8-C7 | 120.8(2) | C9-C8-C7 | 119.4(2) |
| C10-C9-C8 | 120.6(2) | C10-C9-H9 | 119.7 |
| C8-C9-H9 | 119.7 | C9-C10-C11 | 120.6(2) |
| C9-C10-H10 | 119.7 | C11-C10-H10 | 119.7 |
| C12-C11-C10 | 122.0(2) | C12-C11-C11 | 119.2(3) |
| C10-C11-C11 | 118.8(3) | C8-C12-C11 | 121.0(2) |
| C8-C12-H12 | 119.5 | C11-C12-H12 | 119.5 |
| N1-C13-C14 | 123.0(3) | N1-C13-H13 | 118.5 |
| C14-C13-H13 | 118.5 | C13-C14-C15 | 119.0(3) |
| C13-C14-H14 | 120.5 | C15-C14-H14 | 120.5 |
| C16-C15-C14 | 118.3(3) | C16-C15-C18 | 118.8(3) |
| C14-C15-C18 | 122.9(3) | C17-C16-C15 | 119.2(3) |
| C17-C16-H16 | 120.4 | C15-C16-H16 | 120.4 |
| N1-C17-C16 | 122.8(3) | N1-C17-H17 | 118.6 |
| C16-C17-H17 | 118.6 | N2-C18-C15 | 122.6(3) |
| N2-C18-S1 | 116.6(2) | C15-C18-S1 | 120.8(2) |
| C19-C19-N2 | 119.0(4) | C19-C19-S1 | 109.9(3) |
| N2-C19-S1 | 131.1(2) | C22-N3-C21 | 121.8(13) |
| C22-N3-C20 | 120.2(12) | C21-N3-C20 | 117.9(11) |
| N3-C20-H20A | 109.5 | N3-C20-H20B | 109.5 |
| H20A-C20-H20B | 109.5 | N3-C20-H20C | 109.5 |
| H20A-C20-H20C | 109.5 | H20B-C20-H20C | 109.5 |

| | | | |
|---|---|---|---|
| N3-C21-H21A | 109.5 | N3-C21-H21B | 109.5 |
| H21A-C21-H21B | 109.5 | N3-C21-H21C | 109.5 |
| H21A-C21-H21C | 109.5 | H21B-C21-H21C | 109.5 |
| O5-C22-N3 | 119.2(16) | O5-C22-H22 | 120.4 |
| N3-C22-H22 | 120.4 | C22B-N3B-C20B | 119.6(10) |
| C22B-N3B-C21B | 121.5(9) | C20B-N3B-C21B | 118.9(9) |
| N3B-C21B-H21D | 109.5 | N3B-C21B-H21E | 109.5 |
| H21D-C21B-H21E | 109.5 | N3B-C21B-H21F | 109.5 |
| H21D-C21B-H21F | 109.5 | H21E-C21B-H21F | 109.5 |
| N3B-C20B-H20D | 109.5 | N3B-C20B-H20E | 109.5 |
| H20D-C20B-H20E | 109.5 | N3B-C20B-H20F | 109.5 |
| H20D-C20B-H20F | 109.5 | H20E-C20B-H20F | 109.5 |
| O5B-C22B-N3B | 125.7(11) | O5B-C22B-H22B | 117.1 |
| N3B-C22B-H22B | 117.1 | | |

**TableA.6. Anisotropic atomic displacement parameters (Å$^2$) for $Zn_2(NDC)_2(DPTTZ)\cdot(DMF)_2$**

The anisotropic atomic displacement factor exponent takes the form: $-2\pi^2[ h^2 a^{*2} U_{11} + ... + 2 h k a^* b^* U_{12} ]$

| | $U_{11}$ | $U_{22}$ | $U_{33}$ | $U_{23}$ | $U_{13}$ | $U_{12}$ |
|---|---|---|---|---|---|---|
| Zn1 | 0.00820(15) | 0.00842(14) | 0.00926(14) | -0.00165(10) | 0.00004(10) | 0.00054(10) |
| S1 | 0.0199(4) | 0.0370(5) | 0.0450(5) | 0.0147(4) | 0.0044(3) | -0.0002(3) |
| O1 | 0.0248(10) | 0.0210(10) | 0.0116(9) | -0.0057(7) | -0.0024(8) | 0.0002(8) |
| O2 | 0.0247(11) | 0.0286(11) | 0.0146(9) | -0.0072(8) | -0.0073(8) | -0.0006(8) |
| O3 | 0.0113(9) | 0.0131(9) | 0.0284(10) | -0.0040(8) | -0.0020(8) | 0.0038(7) |
| O4 | 0.0141(9) | 0.0101(8) | 0.0227(10) | -0.0041(7) | -0.0037(7) | 0.0030(7) |
| N1 | 0.0133(11) | 0.0143(10) | 0.0136(10) | -0.0019(8) | -0.0001(8) | -0.0022(8) |
| N2 | 0.0302(15) | 0.0264(14) | 0.0336(15) | 0.0084(11) | 0.0149(12) | -0.0061(11) |
| C1 | 0.0201(14) | 0.0179(13) | 0.0132(12) | -0.0069(10) | -0.0064(10) | 0.0077(10) |
| C2 | 0.0205(14) | 0.0282(15) | 0.0139(13) | -0.0091(11) | -0.0045(11) | 0.0016(11) |
| C3 | 0.0305(17) | 0.0415(18) | 0.0159(14) | -0.0069(13) | -0.0004(12) | -0.0148(14) |
| C4 | 0.0353(18) | 0.050(2) | 0.0182(15) | -0.0113(14) | -0.0020(13) | -0.0216(15) |
| C5 | 0.0213(14) | 0.0333(16) | 0.0158(13) | -0.0088(12) | -0.0028(11) | -0.0040(12) |
| C6 | 0.0235(15) | 0.0321(16) | 0.0164(13) | -0.0097(12) | -0.0052(11) | -0.0038(12) |
| C7 | 0.0148(13) | 0.0120(12) | 0.0143(12) | -0.0036(9) | -0.0044(10) | 0.0031(10) |
| C8 | 0.0136(12) | 0.0118(12) | 0.0184(13) | -0.0043(10) | -0.0033(10) | 0.0034(10) |
| C9 | 0.0100(12) | 0.0153(13) | 0.0318(15) | -0.0037(11) | -0.0011(11) | 0.0011(10) |
| C10 | 0.0139(13) | 0.0111(12) | 0.0308(15) | -0.0047(11) | -0.0020(11) | -0.0004(10) |
| C11 | 0.0125(12) | 0.0110(12) | 0.0183(13) | -0.0033(10) | -0.0024(10) | 0.0018(10) |

| | $U_{11}$ | $U_{22}$ | $U_{33}$ | $U_{23}$ | $U_{13}$ | $U_{12}$ |
|---|---|---|---|---|---|---|
| C12 | 0.0144(13) | 0.0094(11) | 0.0198(13) | -0.0041(10) | -0.0043(10) | 0.0020(9) |
| C13 | 0.0177(15) | 0.0235(15) | 0.0375(18) | 0.0070(13) | 0.0038(13) | 0.0040(12) |
| C14 | 0.0218(16) | 0.0237(16) | 0.044(2) | 0.0128(14) | 0.0034(14) | 0.0030(12) |
| C15 | 0.0183(14) | 0.0223(14) | 0.0228(14) | 0.0008(11) | -0.0001(11) | -0.0028(11) |
| C16 | 0.0154(14) | 0.0245(15) | 0.0256(15) | -0.0016(12) | -0.0002(11) | 0.0030(11) |
| C17 | 0.0180(14) | 0.0187(13) | 0.0198(13) | 0.0011(11) | -0.0005(11) | 0.0001(11) |
| C18 | 0.0165(14) | 0.0240(15) | 0.0276(15) | 0.0039(12) | 0.0014(12) | -0.0003(11) |
| C19 | 0.0192(15) | 0.0297(16) | 0.0340(17) | 0.0038(13) | 0.0008(13) | 0.0004(12) |
| N3 | 0.045(5) | 0.072(6) | 0.041(4) | -0.031(5) | -0.014(4) | 0.021(4) |
| C20 | 0.041(5) | 0.092(8) | 0.062(6) | -0.045(7) | -0.012(4) | 0.017(6) |
| C21 | 0.078(8) | 0.064(8) | 0.074(8) | -0.015(6) | -0.010(8) | 0.012(7) |
| C22 | 0.078(6) | 0.094(7) | 0.059(5) | -0.044(5) | -0.017(6) | 0.033(6) |
| O5 | 0.134(7) | 0.140(8) | 0.070(6) | -0.050(6) | -0.029(5) | 0.041(8) |
| N3B | 0.042(4) | 0.071(6) | 0.043(4) | -0.015(4) | -0.010(4) | 0.014(3) |
| C21B | 0.070(6) | 0.066(6) | 0.080(6) | 0.016(5) | -0.009(6) | 0.005(5) |
| C20B | 0.051(5) | 0.133(9) | 0.058(5) | -0.026(8) | -0.001(4) | -0.009(7) |
| C22B | 0.082(6) | 0.094(7) | 0.056(5) | -0.041(5) | -0.020(5) | 0.030(5) |
| O5B | 0.128(6) | 0.141(7) | 0.045(4) | -0.011(5) | -0.010(4) | 0.026(6) |

**Table A.7. Hydrogen atomic coordinates and isotropic atomic displacement parameters (Å$^2$) for $Zn_2(NDC)_2(DPTTZ)\cdot(DMF)_2$**

| | x/a | y/b | z/c | U(eq) |
|---|---|---|---|---|
| H3 | 0.7588 | 0.8165 | 0.2423 | 0.036 |
| H4 | 0.7630 | 0.8095 | 0.0655 | 0.041 |
| H6 | 1.1233 | 1.1056 | 0.1346 | 0.028 |
| H9 | 1.0697 | 0.5397 | 0.5719 | 0.024 |
| H10 | 1.2172 | 0.3500 | 0.5692 | 0.023 |
| H12 | 1.5067 | 0.7604 | 0.4615 | 0.017 |
| H13 | 0.7719 | 0.6559 | 0.7035 | 0.036 |
| H14 | 0.5500 | 0.5312 | 0.8278 | 0.042 |
| H16 | 0.2389 | 0.8253 | 0.7422 | 0.028 |
| H17 | 0.4697 | 0.9426 | 0.6205 | 0.025 |
| H20A | 0.3526 | 0.8972 | 1.2780 | 0.09 |
| H20B | 0.5294 | 0.9173 | 1.1912 | 0.09 |
| H20C | 0.3686 | 0.9965 | 1.1608 | 0.09 |
| H21A | 0.2252 | 0.7139 | 1.3062 | 0.11 |
| H21B | 0.1518 | 0.6844 | 1.2091 | 0.11 |
| H21C | 0.3200 | 0.6158 | 1.2380 | 0.11 |
| H22 | 0.4756 | 0.8817 | 1.0035 | 0.088 |
| H21D | 0.1570 | 0.6604 | 1.3285 | 0.119 |
| H21E | 0.0337 | 0.6886 | 1.2448 | 0.119 |
| H21F | 0.1608 | 0.5700 | 1.2453 | 0.119 |
| H20D | 0.3608 | 0.7942 | 1.2934 | 0.122 |

| | x/a | y/b | z/c | U(eq) |
|---|---|---|---|---|
| H20E | 0.5035 | 0.7948 | 1.1865 | 0.122 |
| H20F | 0.3739 | 0.9117 | 1.1865 | 0.122 |
| H22B | 0.2035 | 0.7182 | 1.0486 | 0.087 |

## APPENDIX B

## SINGLE CRYSTAL X-RAY DATA FOR $Zn_2(1,4\text{-BDC})_2(DPTTZ)_2\cdot(DMF)$

**Table B.1. Sample and crystal data for $Zn_2(1,4\text{-BDC})_2(DPTTZ)_2\cdot(DMF)$**

| | | |
|---|---|---|
| **Chemical formula** | $C_{47}H_{31}N_9O_9S_4Zn_2$ | |
| **Formula weight** | 1124.79 g/mol | |
| **Temperature** | 140(2) K | |
| **Wavelength** | 0.71073 Å | |
| **Crystal size** | 0.028 x 0.031 x 0.299 mm | |
| **Crystal system** | orthorhombic | |
| **Space group** | I b a 2 | |
| **Unit cell dimensions** | a = 34.566(2) Å | |
| | b = 17.1421(8) Å | α = 90° |
| | c = 17.1901(10) Å | β = 90° |
| **Volume** | 10185.7(10) $Å^3$ | γ = 90° |
| **Z** | 8 | |
| **Density (calculated)** | 1.467 $g/cm^3$ | |
| **Absorption coefficient** | 1.168 $mm^{-1}$ | |
| **F(000)** | 4576 | |

**Table B.2. Data collection and structure refinement for $Zn_2(1,4\text{-BDC})_2(DPTTZ)_2\cdot(DMF)$**

| | | |
|---|---|---|
| **Theta range for data collection** | 2.38 to 22.00° | |
| **Index ranges** | -36<=h<=36, -18<=k<=17, -17<=l<=18 | |
| **Reflections collected** | 23443 | |
| **Independent reflections** | 6124 [R(int) = 0.0834] | |
| **Max. and min. transmission** | 1.0000 and 0.8214 | |
| **Structure solution technique** | direct methods | |
| **Structure solution program** | SHELXT-2014 (Sheldrick 2014) | |
| **Refinement method** | Full-matrix least-squares on $F^2$ | |
| **Refinement program** | SHELXL-2014 (Sheldrick 2014) | |
| **Function minimized** | $\Sigma\, w(F_o^2 - F_c^2)^2$ | |
| **Data / restraints / parameters** | 6124 / 1 / 641 | |
| **Goodness-of-fit on $F^2$** | 1.017 | |
| **$\Delta/\sigma_{max}$** | 0.002 | |
| **Final R indices** | 4833 data; $I>2\sigma(I)$ | R1 = 0.0440, wR2 = 0.0816 |
| | all data | R1 = 0.0675, wR2 = 0.0887 |
| **Weighting scheme** | $w=1/[\sigma^2(F_o^2)+(0.0353P)^2+8.3300P]$ where $P=(F_o^2+2F_c^2)/3$ | |

| | |
|---|---|
| **Absolute structure parameter** | 0.4(0) |
| **Largest diff. peak and hole** | 0.921 and -0.357 eÅ$^{-3}$ |
| **R.M.S. deviation from mean** | 0.071 eÅ$^{-3}$ |

**Table B.3. Atomic coordinates and equivalent isotropic atomic displacement parameters (Å$^2$) for $Zn_2$(1,4-BDC)$_2$(DPTTZ)$_2$·(DMF)**

U(eq) is defined as one third of the trace of the orthogonalized $U_{ij}$ tensor.

| | x/a | y/b | z/c | U(eq) |
|---|---|---|---|---|
| Zn1 | 0.59615(3) | 0.61664(6) | 0.58690(7) | 0.0211(3) |
| Zn2 | 0.66280(3) | 0.68371(6) | 0.41134(7) | 0.0221(3) |
| S1 | 0.56215(10) | 0.04308(15) | 0.5236(2) | 0.0464(10) |
| S2 | 0.62673(9) | 0.19315(14) | 0.65611(18) | 0.0375(8) |
| S3 | 0.62509(9) | 0.26103(14) | 0.3589(2) | 0.0400(8) |
| S4 | 0.69265(9) | 0.10919(14) | 0.48317(18) | 0.0375(8) |
| O1 | 0.65270(19) | 0.6211(3) | 0.6176(4) | 0.0268(18) |
| O2 | 0.6817(2) | 0.6862(4) | 0.5211(4) | 0.0322(19) |
| O3 | 0.7814(2) | 0.7969(4) | 0.8705(4) | 0.0342(19) |
| O4 | 0.8245(2) | 0.8085(4) | 0.7769(5) | 0.039(2) |
| O5 | 0.5769(2) | 0.6130(4) | 0.4760(4) | 0.037(2) |
| O6 | 0.6067(2) | 0.6853(4) | 0.3857(4) | 0.032(2) |
| O7 | 0.4184(3) | 0.6111(4) | 0.2215(5) | 0.040(2) |

| | x/a | y/b | z/c | U(eq) |
|---|---|---|---|---|
| O8 | 0.4602(2) | 0.6159(4) | 0.1283(5) | 0.042(2) |
| N1 | 0.5932(2) | 0.7434(4) | 0.5908(7) | 0.026(2) |
| N2 | 0.6133(3) | 0.0325(4) | 0.6340(5) | 0.033(2) |
| N3 | 0.5757(3) | 0.2039(4) | 0.5448(5) | 0.035(3) |
| N4 | 0.5993(2) | 0.4927(4) | 0.5834(6) | 0.026(2) |
| N5 | 0.6646(2) | 0.5590(4) | 0.4092(6) | 0.020(2) |
| N6 | 0.6812(3) | 0.2708(4) | 0.4609(5) | 0.029(2) |
| N7 | 0.6356(3) | 0.1008(4) | 0.3815(5) | 0.035(3) |
| N8 | 0.6591(3) | 0.8109(4) | 0.4175(7) | 0.030(2) |
| C1 | 0.6791(3) | 0.6627(5) | 0.5890(7) | 0.024(2) |
| C2 | 0.7098(3) | 0.6906(5) | 0.6424(6) | 0.022(3) |
| C3 | 0.7412(3) | 0.7286(5) | 0.6146(6) | 0.031(3) |
| C4 | 0.7684(3) | 0.7603(5) | 0.6646(6) | 0.026(3) |
| C5 | 0.7632(3) | 0.7567(5) | 0.7435(6) | 0.023(3) |
| C6 | 0.7317(3) | 0.7174(6) | 0.7726(6) | 0.032(3) |
| C7 | 0.7051(3) | 0.6848(5) | 0.7223(6) | 0.035(3) |
| C8 | 0.7915(4) | 0.7909(6) | 0.8003(7) | 0.033(3) |
| C9 | 0.5787(3) | 0.6463(5) | 0.4109(7) | 0.020(2) |
| C10 | 0.5457(3) | 0.6371(5) | 0.3587(6) | 0.031(3) |
| C11 | 0.5102(3) | 0.6092(6) | 0.3842(7) | 0.036(3) |
| C12 | 0.4793(3) | 0.6028(6) | 0.3319(7) | 0.041(3) |
| C13 | 0.4840(3) | 0.6192(6) | 0.2541(6) | 0.030(3) |
| C14 | 0.5197(4) | 0.6458(7) | 0.2277(7) | 0.055(4) |
| C15 | 0.5506(4) | 0.6549(7) | 0.2803(7) | 0.049(4) |

| | x/a | y/b | z/c | U(eq) |
|---|---|---|---|---|
| C16 | 0.4525(4) | 0.6141(6) | 0.2000(7) | 0.030(3) |
| C17 | 0.6152(3) | 0.7857(5) | 0.6388(7) | 0.033(3) |
| C18 | 0.6149(3) | 0.8665(5) | 0.6395(7) | 0.036(3) |
| C19 | 0.5915(3) | 0.9063(5) | 0.5905(8) | 0.027(3) |
| C20 | 0.5676(3) | 0.8616(5) | 0.5408(6) | 0.038(3) |
| C21 | 0.5695(3) | 0.7820(6) | 0.5445(6) | 0.034(3) |
| C22 | 0.5915(3) | 0.9905(5) | 0.5880(8) | 0.030(3) |
| C23 | 0.6071(3) | 0.1088(5) | 0.6179(6) | 0.027(3) |
| C24 | 0.5818(4) | 0.1264(5) | 0.5607(6) | 0.031(3) |
| C25 | 0.5979(3) | 0.2450(5) | 0.5907(8) | 0.027(3) |
| C26 | 0.5995(3) | 0.3305(5) | 0.5874(7) | 0.024(2) |
| C27 | 0.6238(3) | 0.3727(5) | 0.6362(6) | 0.027(3) |
| C28 | 0.6224(3) | 0.4538(5) | 0.6320(6) | 0.026(3) |
| C29 | 0.5766(4) | 0.4506(6) | 0.5384(7) | 0.037(3) |
| C30 | 0.5759(3) | 0.3698(5) | 0.5391(7) | 0.037(3) |
| C31 | 0.6858(3) | 0.5175(5) | 0.4576(6) | 0.025(3) |
| C32 | 0.6850(3) | 0.4377(5) | 0.4629(6) | 0.026(3) |
| C33 | 0.6604(3) | 0.3977(5) | 0.4134(7) | 0.020(2) |
| C34 | 0.6378(3) | 0.4398(5) | 0.3591(6) | 0.024(3) |
| C35 | 0.6416(3) | 0.5191(5) | 0.3604(6) | 0.028(3) |
| C36 | 0.6582(3) | 0.3117(5) | 0.4156(8) | 0.027(3) |
| C37 | 0.6438(3) | 0.1760(5) | 0.3951(7) | 0.033(3) |
| C38 | 0.6730(4) | 0.1938(5) | 0.4478(7) | 0.034(3) |
| C39 | 0.6598(3) | 0.0587(5) | 0.4249(6) | 0.024(3) |

| | x/a | y/b | z/c | U(eq) |
|---|---|---|---|---|
| C40 | 0.6602(3) | 0.9727(5) | 0.4234(7) | 0.028(3) |
| C41 | 0.6870(3) | 0.9304(6) | 0.4639(6) | 0.037(3) |
| C42 | 0.6854(3) | 0.8499(6) | 0.4596(6) | 0.035(3) |
| C43 | 0.6327(3) | 0.8534(6) | 0.3799(7) | 0.039(3) |
| C44 | 0.6323(3) | 0.9322(5) | 0.3807(6) | 0.037(3) |
| O9 | 0.7522(3) | 0.9864(5) | 0.5890(6) | 0.066(3) |
| C45 | 0.7534(4) | 0.9909(9) | 0.7969(8) | 0.076(5) |
| C46 | 0.7028(5) | 0.021(2) | 0.7119(11) | 0.29(2) |
| C47 | 0.7612(4) | 0.9835(7) | 0.6566(11) | 0.059(4) |
| N9 | 0.7404(3) | 0.9925(6) | 0.7183(6) | 0.051(3) |

**Table B.4. Bond lengths (Å) for $Zn_2(1,4\text{-BDC})_2(DPTTZ)_2\cdot(DMF)$**

| | | | |
|---|---|---|---|
| Zn1-O5 | 2.021(7) | Zn1-O1 | 2.026(7) |
| Zn1-O8 | 2.075(8) | Zn1-N4 | 2.129(7) |
| Zn1-N1 | 2.177(7) | Zn1-O7 | 2.370(8) |
| Zn1-C16 | 2.571(11) | Zn2-O6 | 1.988(7) |
| Zn2-O2 | 1.997(7) | Zn2-O3 | 2.078(7) |
| Zn2-N5 | 2.140(7) | Zn2-N8 | 2.187(7) |
| Zn2-O4 | 2.355(8) | Zn2-C8 | 2.515(12) |
| S1-C24 | 1.705(10) | S1-C22 | 1.753(12) |
| S2-C23 | 1.728(10) | S2-C25 | 1.747(11) |
| S3-C37 | 1.712(9) | S3-C36 | 1.736(11) |
| S4-C38 | 1.714(10) | S4-C39 | 1.745(11) |

| | | | |
|---|---|---|---|
| O1-C1 | 1.259(11) | O2-C1 | 1.238(12) |
| O3-C8 | 1.262(13) | O3-Zn2 | 2.078(7) |
| O4-C8 | 1.247(13) | O4-Zn2 | 2.355(8) |
| O5-C9 | 1.257(12) | O6-C9 | 1.254(11) |
| O7-C16 | 1.237(13) | O7-Zn1 | 2.370(8) |
| O8-C16 | 1.261(12) | O8-Zn1 | 2.075(8) |
| N1-C21 | 1.318(13) | N1-C17 | 1.336(13) |
| N2-C22 | 1.308(13) | N2-C23 | 1.354(12) |
| N3-C25 | 1.306(13) | N3-C24 | 1.373(11) |
| N4-C29 | 1.317(13) | N4-C28 | 1.334(12) |
| N4-Zn1 | 2.129(7) | N5-C31 | 1.317(12) |
| N5-C35 | 1.342(12) | N6-C36 | 1.316(13) |
| N6-C38 | 1.368(12) | N7-C39 | 1.333(12) |
| N7-C37 | 1.339(12) | N8-C43 | 1.334(13) |
| N8-C42 | 1.340(13) | N8-Zn2 | 2.187(7) |
| C1-C2 | 1.480(14) | C2-C3 | 1.355(13) |
| C2-C7 | 1.386(13) | C3-C4 | 1.386(13) |
| C3-H3 | 0.95 | C4-C5 | 1.369(14) |
| C4-H4 | 0.95 | C5-C6 | 1.374(13) |
| C5-C8 | 1.503(15) | C6-C7 | 1.380(13) |
| C6-H6 | 0.95 | C7-H7 | 0.95 |
| C8-Zn2 | 2.515(12) | C9-C10 | 1.462(14) |
| C10-C11 | 1.388(14) | C10-C15 | 1.391(14) |
| C11-C12 | 1.399(14) | C11-H11 | 0.95 |
| C12-C13 | 1.377(15) | C12-H12 | 0.95 |

| | | | |
|---|---|---|---|
| C13-C14 | 1.390(15) | C13-C16 | 1.435(14) |
| C14-C15 | 1.407(15) | C14-H14 | 0.95 |
| C15-H15 | 0.95 | C16-Zn1 | 2.571(11) |
| C17-C18 | 1.385(13) | C17-H17 | 0.95 |
| C18-C19 | 1.353(15) | C18-H18 | 0.95 |
| C19-C20 | 1.412(16) | C19-C22 | 1.443(12) |
| C20-C21 | 1.368(13) | C20-H20 | 0.95 |
| C21-H21 | 0.95 | C23-C24 | 1.350(13) |
| C25-C26 | 1.468(12) | C26-C30 | 1.344(14) |
| C26-C27 | 1.390(14) | C27-C28 | 1.392(12) |
| C27-H27 | 0.95 | C28-H28 | 0.95 |
| C29-C30 | 1.384(13) | C29-H29 | 0.95 |
| C30-H30 | 0.95 | C31-C32 | 1.372(13) |
| C31-H31 | 0.95 | C32-C33 | 1.383(14) |
| C32-H32 | 0.95 | C33-C34 | 1.416(14) |
| C33-C36 | 1.476(12) | C34-C35 | 1.366(12) |
| C34-H34 | 0.95 | C35-H35 | 0.95 |
| C37-C38 | 1.389(14) | C39-C40 | 1.474(13) |
| C40-C41 | 1.368(14) | C40-C44 | 1.397(13) |
| C41-C42 | 1.384(13) | C41-H41 | 0.95 |
| C42-H42 | 0.95 | C43-C44 | 1.352(13) |
| C43-H43 | 0.95 | C44-H44 | 0.95 |
| O9-C47 | 1.205(16) | C45-N9 | 1.425(14) |
| C45-H45A | 0.98 | C45-H45B | 0.98 |
| C45-H45C | 0.98 | C46-N9 | 1.393(19) |

| | | | |
|---|---|---|---|
| C46-H46A | 0.98 | C46-H46B | 0.98 |
| C46-H46C | 0.98 | C47-N9 | 1.292(16) |
| C47-H47 | 0.95 | | |

**Table B.5. Bond angles (°) for $Zn_2(1,4\text{-}BDC)_2(DPTTZ)_2\cdot(DMF)$**

| | | | |
|---|---|---|---|
| O5-Zn1-O1 | 124.4(3) | O5-Zn1-O8 | 90.9(3) |
| O1-Zn1-O8 | 144.8(3) | O5-Zn1-N4 | 87.7(3) |
| O1-Zn1-N4 | 89.7(3) | O8-Zn1-N4 | 93.0(3) |
| O5-Zn1-N1 | 92.5(3) | O1-Zn1-N1 | 90.0(3) |
| O8-Zn1-N1 | 87.2(3) | N4-Zn1-N1 | 179.7(4) |
| O5-Zn1-O7 | 148.3(3) | O1-Zn1-O7 | 87.2(3) |
| O8-Zn1-O7 | 57.7(3) | N4-Zn1-O7 | 89.9(3) |
| N1-Zn1-O7 | 90.0(3) | O5-Zn1-C16 | 119.9(4) |
| O1-Zn1-C16 | 115.7(4) | O8-Zn1-C16 | 29.1(3) |
| N4-Zn1-C16 | 92.2(3) | N1-Zn1-C16 | 87.9(3) |
| O7-Zn1-C16 | 28.6(3) | O6-Zn2-O2 | 121.8(3) |
| O6-Zn2-O3 | 145.8(3) | O2-Zn2-O3 | 90.7(3) |
| O6-Zn2-N5 | 92.2(3) | O2-Zn2-N5 | 91.6(3) |
| O3-Zn2-N5 | 97.2(3) | O6-Zn2-N8 | 86.5(3) |
| O2-Zn2-N8 | 87.2(3) | O3-Zn2-N8 | 84.9(3) |
| N5-Zn2-N8 | 177.6(4) | O6-Zn2-O4 | 87.9(3) |
| O2-Zn2-O4 | 149.9(3) | O3-Zn2-O4 | 59.2(3) |
| N5-Zn2-O4 | 91.9(3) | N8-Zn2-O4 | 90.1(4) |
| O6-Zn2-C8 | 116.2(4) | O2-Zn2-C8 | 120.6(4) |

| | | | |
|---|---|---|---|
| O3-Zn2-C8 | 30.0(3) | N5-Zn2-C8 | 98.1(3) |
| N8-Zn2-C8 | 84.3(3) | O4-Zn2-C8 | 29.4(3) |
| C24-S1-C22 | 87.9(5) | C23-S2-C25 | 87.5(5) |
| C37-S3-C36 | 88.4(5) | C38-S4-C39 | 87.6(5) |
| C1-O1-Zn1 | 128.3(7) | C1-O2-Zn2 | 149.5(7) |
| C8-O3-Zn2 | 94.5(7) | C8-O4-Zn2 | 82.4(7) |
| C9-O5-Zn1 | 144.0(7) | C9-O6-Zn2 | 131.9(6) |
| C16-O7-Zn1 | 84.7(7) | C16-O8-Zn1 | 97.9(7) |
| C21-N1-C17 | 117.0(8) | C21-N1-Zn1 | 120.8(8) |
| C17-N1-Zn1 | 122.2(7) | C22-N2-C23 | 108.4(9) |
| C25-N3-C24 | 108.2(9) | C29-N4-C28 | 116.8(8) |
| C29-N4-Zn1 | 122.2(7) | C28-N4-Zn1 | 120.7(7) |
| C31-N5-C35 | 116.7(8) | C31-N5-Zn2 | 123.0(7) |
| C35-N5-Zn2 | 120.1(7) | C36-N6-C38 | 107.0(9) |
| C39-N7-C37 | 106.9(9) | C43-N8-C42 | 117.0(8) |
| C43-N8-Zn2 | 124.1(7) | C42-N8-Zn2 | 118.9(7) |
| O2-C1-O1 | 127.1(10) | O2-C1-C2 | 115.4(9) |
| O1-C1-C2 | 117.4(10) | C3-C2-C7 | 118.5(10) |
| C3-C2-C1 | 120.6(10) | C7-C2-C1 | 120.5(10) |
| C2-C3-C4 | 120.9(10) | C2-C3-H3 | 119.6 |
| C4-C3-H3 | 119.6 | C5-C4-C3 | 120.5(10) |
| C5-C4-H4 | 119.8 | C3-C4-H4 | 119.8 |
| C4-C5-C6 | 119.2(10) | C4-C5-C8 | 122.6(11) |
| C6-C5-C8 | 118.1(10) | C5-C6-C7 | 119.8(10) |
| C5-C6-H6 | 120.1 | C7-C6-H6 | 120.1 |

| | | | |
|---|---|---|---|
| C6-C7-C2 | 121.0(10) | C6-C7-H7 | 119.5 |
| C2-C7-H7 | 119.5 | O4-C8-O3 | 122.8(11) |
| O4-C8-C5 | 118.8(11) | O3-C8-C5 | 118.2(11) |
| O4-C8-Zn2 | 68.2(6) | O3-C8-Zn2 | 55.5(6) |
| C5-C8-Zn2 | 165.9(8) | O6-C9-O5 | 126.0(10) |
| O6-C9-C10 | 116.6(10) | O5-C9-C10 | 117.3(10) |
| C11-C10-C15 | 119.3(11) | C11-C10-C9 | 122.2(11) |
| C15-C10-C9 | 118.4(11) | C10-C11-C12 | 119.9(11) |
| C10-C11-H11 | 120.1 | C12-C11-H11 | 120.1 |
| C13-C12-C11 | 121.2(11) | C13-C12-H12 | 119.4 |
| C11-C12-H12 | 119.4 | C12-C13-C14 | 119.2(11) |
| C12-C13-C16 | 121.8(12) | C14-C13-C16 | 118.8(10) |
| C13-C14-C15 | 120.0(11) | C13-C14-H14 | 120.0 |
| C15-C14-H14 | 120.0 | C10-C15-C14 | 120.3(11) |
| C10-C15-H15 | 119.8 | C14-C15-H15 | 119.8 |
| O7-C16-O8 | 119.7(11) | O7-C16-C13 | 122.2(11) |
| O8-C16-C13 | 118.1(11) | O7-C16-Zn1 | 66.6(6) |
| O8-C16-Zn1 | 53.1(6) | C13-C16-Zn1 | 170.2(9) |
| N1-C17-C18 | 122.9(11) | N1-C17-H17 | 118.6 |
| C18-C17-H17 | 118.6 | C19-C18-C17 | 120.3(11) |
| C19-C18-H18 | 119.8 | C17-C18-H18 | 119.8 |
| C18-C19-C20 | 116.8(8) | C18-C19-C22 | 121.4(11) |
| C20-C19-C22 | 121.8(11) | C21-C20-C19 | 119.1(10) |
| C21-C20-H20 | 120.5 | C19-C20-H20 | 120.5 |
| N1-C21-C20 | 123.9(10) | N1-C21-H21 | 118.1 |

| | | | |
|---|---|---|---|
| C20-C21-H21 | 118.1 | N2-C22-C19 | 122.3(11) |
| N2-C22-S1 | 115.6(7) | C19-C22-S1 | 122.1(10) |
| C24-C23-N2 | 118.0(9) | C24-C23-S2 | 110.1(7) |
| N2-C23-S2 | 131.9(9) | C23-C24-N3 | 117.5(9) |
| C23-C24-S1 | 110.0(7) | N3-C24-S1 | 132.5(9) |
| N3-C25-C26 | 122.5(10) | N3-C25-S2 | 116.7(6) |
| C26-C25-S2 | 120.8(9) | C30-C26-C27 | 118.5(8) |
| C30-C26-C25 | 120.1(10) | C27-C26-C25 | 121.3(10) |
| C26-C27-C28 | 117.9(10) | C26-C27-H27 | 121.0 |
| C28-C27-H27 | 121.0 | N4-C28-C27 | 123.4(10) |
| N4-C28-H28 | 118.3 | C27-C28-H28 | 118.3 |
| N4-C29-C30 | 123.6(10) | N4-C29-H29 | 118.2 |
| C30-C29-H29 | 118.2 | C26-C30-C29 | 119.7(10) |
| C26-C30-H30 | 120.1 | C29-C30-H30 | 120.1 |
| N5-C31-C32 | 124.7(10) | N5-C31-H31 | 117.7 |
| C32-C31-H31 | 117.7 | C31-C32-C33 | 117.8(10) |
| C31-C32-H32 | 121.1 | C33-C32-H32 | 121.1 |
| C32-C33-C34 | 119.5(8) | C32-C33-C36 | 120.7(10) |
| C34-C33-C36 | 119.8(10) | C35-C34-C33 | 116.3(9) |
| C35-C34-H34 | 121.8 | C33-C34-H34 | 121.8 |
| N5-C35-C34 | 125.0(10) | N5-C35-H35 | 117.5 |
| C34-C35-H35 | 117.5 | N6-C36-C33 | 121.1(10) |
| N6-C36-S3 | 117.6(7) | C33-C36-S3 | 121.3(9) |
| N7-C37-C38 | 118.7(9) | N7-C37-S3 | 132.5(10) |
| C38-C37-S3 | 108.9(7) | N6-C38-C37 | 118.1(9) |

| | | | |
|---|---|---|---|
| N6-C38-S4 | 132.5(10) | C37-C38-S4 | 109.4(7) |
| N7-C39-C40 | 122.6(9) | N7-C39-S4 | 117.4(6) |
| C40-C39-S4 | 120.0(9) | C41-C40-C44 | 118.2(9) |
| C41-C40-C39 | 121.8(10) | C44-C40-C39 | 120.0(10) |
| C40-C41-C42 | 118.3(10) | C40-C41-H41 | 120.9 |
| C42-C41-H41 | 120.9 | N8-C42-C41 | 123.6(11) |
| N8-C42-H42 | 118.2 | C41-C42-H42 | 118.2 |
| N8-C43-C44 | 123.3(11) | N8-C43-H43 | 118.4 |
| C44-C43-H43 | 118.4 | C43-C44-C40 | 119.6(10) |
| C43-C44-H44 | 120.2 | C40-C44-H44 | 120.2 |
| N9-C45-H45A | 109.5 | N9-C45-H45B | 109.5 |
| H45A-C45-H45B | 109.5 | N9-C45-H45C | 109.5 |
| H45A-C45-H45C | 109.5 | H45B-C45-H45C | 109.5 |
| N9-C46-H46A | 109.5 | N9-C46-H46B | 109.5 |
| H46A-C46-H46B | 109.5 | N9-C46-H46C | 109.5 |
| H46A-C46-H46C | 109.5 | H46B-C46-H46C | 109.5 |
| O9-C47-N9 | 130.0(14) | O9-C47-H47 | 115.0 |
| N9-C47-H47 | 115.0 | C47-N9-C46 | 119.9(13) |
| C47-N9-C45 | 126.9(12) | C46-N9-C45 | 112.0(12) |

**Table B.6. Anisotropic atomic displacement parameters (Å$^2$) for $Zn_2$(1,4-BDC)$_2$(DPTTZ)$_2$·(DMF)**

The anisotropic atomic displacement factor exponent takes the form: $-2\pi^2[ h^2 a^{*2} U_{11} + ... + 2 h k a^* b^* U_{12} ]$

| | $U_{11}$ | $U_{22}$ | $U_{33}$ | $U_{23}$ | $U_{13}$ | $U_{12}$ |
|---|---|---|---|---|---|---|
| Zn1 | 0.0268(8) | 0.0112(5) | 0.0253(7) | 0.0011(6) | -0.0023(7) | -0.0013(5) |
| Zn2 | 0.0278(8) | 0.0109(5) | 0.0276(7) | -0.0001(6) | 0.0010(7) | -0.0032(5) |
| S1 | 0.071(3) | 0.0125(14) | 0.056(2) | -0.0010(14) | -0.023(2) | -0.0013(15) |
| S2 | 0.048(2) | 0.0142(14) | 0.050(2) | 0.0009(15) | -0.0106(16) | -0.0010(13) |
| S3 | 0.052(2) | 0.0136(14) | 0.054(2) | 0.0018(14) | -0.0125(18) | -0.0026(14) |
| S4 | 0.056(2) | 0.0117(14) | 0.0453(19) | -0.0006(14) | -0.0087(17) | 0.0008(13) |
| O1 | 0.019(4) | 0.021(4) | 0.040(5) | 0.002(3) | -0.004(4) | -0.008(3) |
| O2 | 0.055(6) | 0.022(4) | 0.019(5) | -0.003(4) | -0.001(4) | -0.006(4) |
| O3 | 0.040(5) | 0.033(4) | 0.030(5) | -0.006(4) | -0.006(4) | -0.002(3) |
| O4 | 0.031(6) | 0.034(4) | 0.051(6) | -0.007(4) | -0.003(5) | -0.003(4) |
| O5 | 0.057(6) | 0.022(4) | 0.032(5) | 0.004(4) | -0.006(4) | 0.001(4) |
| O6 | 0.031(5) | 0.020(4) | 0.046(5) | 0.008(3) | 0.001(4) | -0.002(3) |
| O7 | 0.031(6) | 0.044(5) | 0.045(5) | 0.003(4) | -0.009(5) | -0.007(4) |
| O8 | 0.053(6) | 0.033(4) | 0.041(6) | -0.003(4) | -0.007(5) | -0.006(4) |
| N1 | 0.028(6) | 0.020(4) | 0.030(6) | 0.000(6) | 0.003(5) | -0.001(4) |
| N2 | 0.043(7) | 0.009(5) | 0.047(7) | 0.003(4) | 0.001(5) | -0.001(4) |
| N3 | 0.062(8) | 0.009(5) | 0.033(6) | 0.010(4) | -0.015(5) | 0.007(4) |
| N4 | 0.028(6) | 0.015(4) | 0.035(5) | -0.003(6) | -0.012(5) | 0.002(4) |

| | $U_{11}$ | $U_{22}$ | $U_{33}$ | $U_{23}$ | $U_{13}$ | $U_{12}$ |
|---|---|---|---|---|---|---|
| N5 | 0.024(6) | 0.022(4) | 0.014(5) | -0.006(5) | 0.003(5) | 0.000(4) |
| N6 | 0.042(7) | 0.013(5) | 0.032(6) | 0.000(4) | 0.004(5) | -0.002(4) |
| N7 | 0.044(7) | 0.009(5) | 0.052(7) | -0.004(4) | -0.009(5) | -0.001(4) |
| N8 | 0.039(6) | 0.013(4) | 0.038(6) | -0.008(5) | -0.008(5) | -0.003(4) |
| C1 | 0.020(7) | 0.010(5) | 0.042(8) | -0.001(6) | 0.006(6) | -0.003(5) |
| C2 | 0.022(7) | 0.016(5) | 0.029(7) | 0.003(5) | -0.003(6) | -0.007(5) |
| C3 | 0.051(9) | 0.030(6) | 0.013(6) | -0.003(5) | -0.005(6) | 0.000(6) |
| C4 | 0.024(7) | 0.026(6) | 0.029(7) | 0.005(5) | 0.001(6) | -0.008(5) |
| C5 | 0.022(7) | 0.032(6) | 0.016(6) | -0.004(5) | -0.005(5) | -0.005(5) |
| C6 | 0.031(8) | 0.045(7) | 0.020(7) | 0.000(6) | -0.003(6) | -0.010(6) |
| C7 | 0.043(8) | 0.026(6) | 0.034(8) | -0.001(5) | 0.006(6) | -0.009(5) |
| C8 | 0.042(9) | 0.020(6) | 0.039(9) | -0.003(6) | -0.003(7) | 0.006(6) |
| C9 | 0.022(7) | 0.013(5) | 0.024(6) | -0.009(6) | -0.006(6) | 0.014(5) |
| C10 | 0.029(8) | 0.028(6) | 0.036(8) | -0.003(5) | 0.000(6) | 0.006(5) |
| C11 | 0.025(8) | 0.048(7) | 0.035(8) | 0.011(6) | -0.005(6) | -0.003(6) |
| C12 | 0.023(8) | 0.042(7) | 0.056(9) | 0.001(6) | 0.004(7) | -0.005(6) |
| C13 | 0.030(8) | 0.037(6) | 0.024(7) | 0.003(5) | -0.010(6) | 0.006(6) |
| C14 | 0.040(10) | 0.097(11) | 0.030(8) | 0.006(7) | -0.001(7) | -0.006(8) |
| C15 | 0.035(9) | 0.076(9) | 0.035(9) | 0.010(7) | -0.005(7) | -0.016(7) |
| C16 | 0.033(9) | 0.028(6) | 0.030(8) | 0.003(6) | -0.005(7) | -0.005(6) |
| C17 | 0.052(9) | 0.009(6) | 0.039(8) | -0.005(5) | -0.007(7) | 0.004(5) |
| C18 | 0.036(8) | 0.020(6) | 0.053(9) | -0.012(6) | -0.007(7) | -0.003(5) |
| C19 | 0.039(7) | 0.011(5) | 0.030(6) | 0.011(6) | -0.002(6) | 0.004(5) |
| C20 | 0.073(11) | 0.010(6) | 0.031(7) | -0.002(5) | -0.016(7) | 0.014(6) |

| | $U_{11}$ | $U_{22}$ | $U_{33}$ | $U_{23}$ | $U_{13}$ | $U_{12}$ |
|---|---|---|---|---|---|---|
| C21 | 0.042(9) | 0.025(6) | 0.035(8) | 0.004(5) | -0.017(6) | -0.004(6) |
| C22 | 0.041(8) | 0.012(5) | 0.038(7) | -0.003(6) | 0.010(7) | 0.000(5) |
| C23 | 0.034(8) | 0.017(6) | 0.030(7) | -0.004(5) | 0.002(6) | -0.001(5) |
| C24 | 0.047(9) | 0.006(6) | 0.040(9) | 0.002(5) | -0.002(7) | -0.007(5) |
| C25 | 0.037(7) | 0.013(5) | 0.030(7) | 0.003(6) | -0.005(6) | 0.002(5) |
| C26 | 0.032(7) | 0.016(5) | 0.024(6) | 0.002(7) | 0.005(6) | -0.002(5) |
| C27 | 0.024(8) | 0.019(6) | 0.039(7) | 0.001(5) | -0.005(6) | 0.007(5) |
| C28 | 0.024(8) | 0.022(6) | 0.031(7) | -0.005(5) | -0.002(6) | -0.011(5) |
| C29 | 0.058(10) | 0.020(6) | 0.033(7) | 0.008(6) | -0.015(7) | 0.008(6) |
| C30 | 0.047(9) | 0.017(6) | 0.046(8) | -0.006(6) | -0.020(7) | -0.011(6) |
| C31 | 0.032(8) | 0.020(6) | 0.022(7) | -0.011(5) | 0.000(6) | -0.003(5) |
| C32 | 0.037(8) | 0.014(6) | 0.026(7) | 0.000(5) | 0.005(6) | -0.005(5) |
| C33 | 0.026(7) | 0.006(5) | 0.028(6) | 0.003(6) | 0.010(6) | 0.003(5) |
| C34 | 0.030(7) | 0.006(5) | 0.036(7) | -0.009(5) | 0.004(6) | -0.006(5) |
| C35 | 0.024(7) | 0.030(7) | 0.031(7) | -0.004(6) | -0.011(6) | 0.007(5) |
| C36 | 0.036(7) | 0.018(5) | 0.028(6) | -0.004(6) | 0.005(6) | 0.000(5) |
| C37 | 0.045(8) | 0.009(5) | 0.045(9) | 0.010(5) | -0.002(7) | 0.006(5) |
| C38 | 0.051(9) | 0.009(6) | 0.042(8) | 0.005(5) | 0.001(7) | 0.005(5) |
| C39 | 0.040(8) | 0.010(5) | 0.023(7) | -0.004(5) | 0.009(6) | -0.009(5) |
| C40 | 0.041(8) | 0.021(6) | 0.022(7) | -0.001(6) | -0.003(6) | -0.002(5) |
| C41 | 0.060(10) | 0.024(7) | 0.027(7) | 0.007(6) | -0.013(7) | -0.002(6) |
| C42 | 0.045(9) | 0.013(6) | 0.046(8) | 0.003(5) | -0.016(7) | -0.009(5) |
| C43 | 0.034(8) | 0.019(6) | 0.063(9) | 0.011(6) | -0.004(7) | -0.002(5) |
| C44 | 0.046(9) | 0.022(6) | 0.042(8) | 0.006(5) | -0.016(6) | -0.004(5) |

| | $U_{11}$ | $U_{22}$ | $U_{33}$ | $U_{23}$ | $U_{13}$ | $U_{12}$ |
|---|---|---|---|---|---|---|
| O9 | 0.072(7) | 0.091(7) | 0.034(6) | -0.009(6) | 0.002(6) | -0.006(5) |
| C45 | 0.064(12) | 0.101(11) | 0.064(11) | 0.010(9) | -0.018(9) | 0.008(9) |
| C46 | 0.042(14) | 0.73(7) | 0.102(18) | 0.06(3) | 0.006(13) | 0.10(3) |
| C47 | 0.041(9) | 0.056(9) | 0.080(12) | 0.006(9) | 0.016(10) | 0.004(7) |
| N9 | 0.027(7) | 0.093(8) | 0.033(7) | 0.003(6) | -0.004(6) | -0.007(6) |

**Table B.7. Hydrogen atomic coordinates and isotropic atomic displacement parameters ($Å^2$) for $Zn_2$(1,4 -BDC)$_2$(DPTTZ)$_2$·(DMF)**

| | x/a | y/b | z/c | U(eq) |
|---|---|---|---|---|
| H3 | 0.7447 | 0.7336 | 0.5599 | 0.038 |
| H4 | 0.7909 | 0.7848 | 0.6441 | 0.032 |
| H6 | 0.7282 | 0.7128 | 0.8272 | 0.038 |
| H7 | 0.6834 | 0.6579 | 0.7427 | 0.041 |
| H11 | 0.5069 | 0.5945 | 0.4370 | 0.043 |
| H12 | 0.4547 | 0.5868 | 0.3505 | 0.049 |
| H14 | 0.5232 | 0.6579 | 0.1743 | 0.066 |
| H15 | 0.5749 | 0.6733 | 0.2622 | 0.059 |
| H17 | 0.6318 | 0.7591 | 0.6740 | 0.04 |
| H18 | 0.6311 | 0.8940 | 0.6745 | 0.044 |
| H20 | 0.5505 | 0.8865 | 0.5054 | 0.045 |
| H21 | 0.5528 | 0.7527 | 0.5117 | 0.041 |
| H27 | 0.6407 | 1.3471 | 0.6713 | 0.033 |

| | x/a | y/b | z/c | U(eq) |
|---|---|---|---|---|
| H28 | 0.6388 | 1.4830 | 0.6655 | 0.031 |
| H29 | 0.5598 | 1.4771 | 0.5036 | 0.044 |
| H30 | 0.5588 | 1.3423 | 0.5057 | 0.044 |
| H31 | 0.7029 | 0.5448 | 0.4913 | 0.03 |
| H32 | 0.7007 | 0.4108 | 0.4993 | 0.031 |
| H34 | 0.6209 | 0.4143 | 0.3237 | 0.029 |
| H35 | 0.6268 | 0.5483 | 0.3240 | 0.034 |
| H41 | 0.7063 | -0.0443 | 0.4943 | 0.045 |
| H42 | 0.7039 | -0.1794 | 0.4880 | 0.041 |
| H43 | 0.6133 | -0.1731 | 0.3511 | 0.046 |
| H44 | 0.6131 | -0.0401 | 0.3524 | 0.044 |
| H45A | 0.7313 | -0.0007 | 0.8318 | 0.114 |
| H45B | 0.7651 | -0.0599 | 0.8081 | 0.114 |
| H45C | 0.7726 | 0.0322 | 0.8050 | 0.114 |
| H46A | 0.6911 | 0.0246 | 0.7637 | 0.438 |
| H46B | 0.7035 | 0.0735 | 0.6885 | 0.438 |
| H46C | 0.6874 | -0.0135 | 0.6791 | 0.438 |
| H47 | 0.7878 | -0.0269 | 0.6661 | 0.071 |

## APPENDIX C

## EDX SPECTRUM AND ELEMENTAL MAPPING OF 1-EDOT

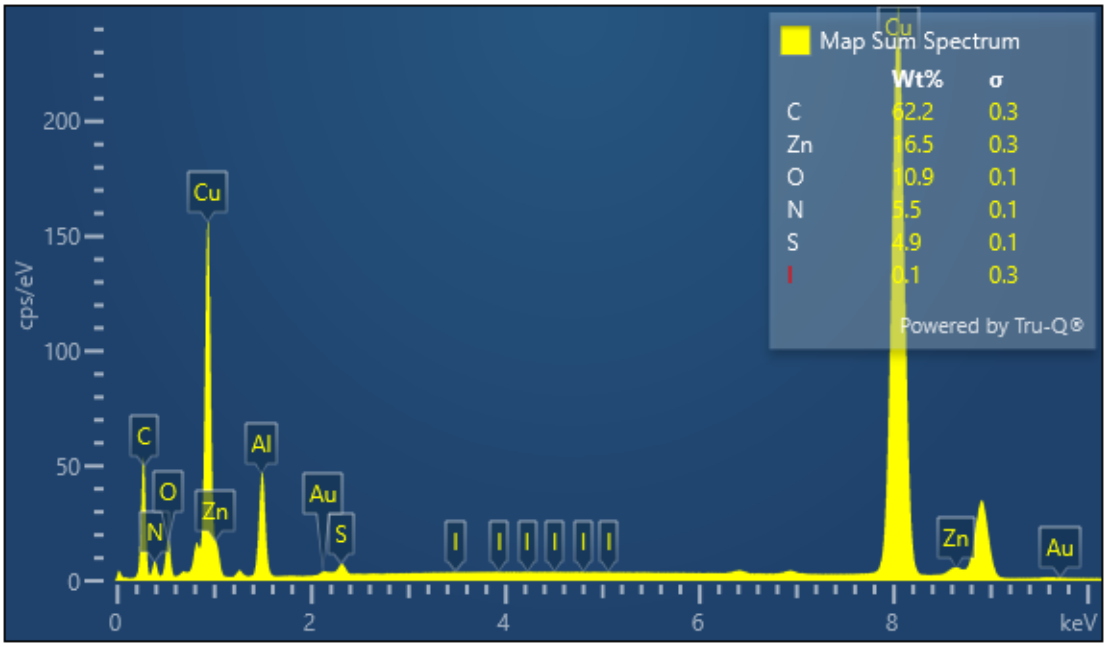


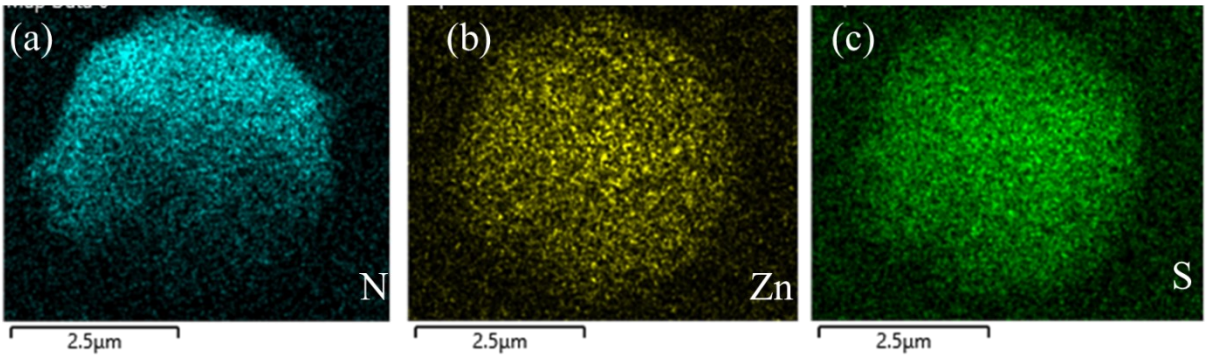

# APPENDIX D

# COPYRIGHT PERMISSION FOR CHAPTER TWO

# APPENDIX E

# COPYRIGHT PERMISSION FOR CHAPTER THREE

**Lowering Band Gap of an Electroactive Metal–Organic Framework via Complementary Guest Intercalation**

**Author:** Zhiyong Guo, Dillip K. Panda, Monica A. Gordillo, et al
**Publication:** Applied Materials
**Publisher:** American Chemical Society
**Date:** Sep 1, 2017

## APPENDIX F

## COPYRIGHT PERMISSION FOR FIGURE 4.1a AND REPORTED PXRD OF Zn(NDI-H) 4.1b

10/22/21, 4:42 AM https://marketplace.copyright.com/rs-ui-web/mp/license/7eae8baf-b658-4551-afba-9c3bca370124/22695ec7-80fd-4829-8b71-1fb...

CCC Marketplace™

This is a License Agreement between Amina Khatun ("User") and Copyright Clearance Center, Inc. ("CCC") on behalf of the Rightsholder identified in the order details below. The license consists of the order details, the CCC Terms and Conditions below, and any Rightsholder Terms and Conditions which are included below.

All payments must be made in full to CCC in accordance with the CCC Terms and Conditions below.

| | | | |
|---|---|---|---|
| Order Date | 20-Oct-2021 | Type of Use | Republish in a thesis/dissertation |
| Order License ID | 1155781-1 | | |
| ISSN | 1754-5706 | Publisher | RSC Publishing |
| | | Portion | Chart/graph/table/figure |

LICENSED CONTENT

| | | | |
|---|---|---|---|
| Publication Title | Energy & environmental science | Rightsholder | Royal Society of Chemistry |
| | | Publication Type | e-Journal |
| Article Title | Postsynthetic tuning of hydrophilicity in pyrazolate MOFs to modulate water adsorption properties | Start Page | 2172 |
| | | Issue | 7 |
| | | Volume | 6 |
| Author/Editor | Royal Society of Chemistry (Great Britain) | URL | http://www.rsc.org/Publishing/Journals/EE/Index.asp |
| Date | 01/01/2008 | | |
| Language | English | | |
| Country | United Kingdom of Great Britain and Northern | | |

REQUEST DETAILS

| | | | |
|---|---|---|---|
| Portion Type | Chart/graph/table/figure | Distribution | Worldwide |
| Number of charts / graphs / tables / figures requested | 4 | Translation | Original language of publication |
| | | Copies for the disabled? | No |
| Format (select all that apply) | Electronic | Minor editing privileges? | No |
| Who will republish the content? | Academic institution | Incidental promotional use? | No |
| Duration of Use | Life of current edition | Currency | USD |
| Lifetime Unit Quantity | Up to 499 | | |
| Rights Requested | Main product | | |

NEW WORK DETAILS

| | | | |
|---|---|---|---|
| Title | NA | Institution name | Clemson University |
| Instructor name | Sourav Saha | Expected presentation date | 2021-11-09 |

on the license

REUSE CONTENT DETAILS

| | | | |
|---|---|---|---|
| Title, description or numeric reference of the portion(s) | NA | Title of the article/chapter the portion is from | Postsynthetic tuning of hydrophilicity in pyrazolate MOFs to modulate water adsorption properties |
| Editor of portion(s) | Wade, Casey R.; Corrales-Sanchez, Tachmajal; Narayan, Tarun C.; Dincă, Mircea | Author of portion(s) | Wade, Casey R.; Corrales-Sanchez, Tachmajal; Narayan, Tarun C.; Dincă, Mircea |
| Volume of serial or monograph | 6 | | |
| Page or page range of portion | 2172 | Issue, if republishing an article from a serial | 7 |
| | | Publication date of portion | 2013-06-19 |